UNIVERSITY OF CAPE TOWN

MASTERS THESIS

MAX Phases as an Electrocatalyst Support Material: A DFT Study

Author:
Jonathan GERTZEN

Supervisors:
Ms. Tokoloho RAMPAI
Ms. Tracey VAN HEERDEN
A/Prof. Pieter LEVECQUE

A thesis submitted in partial fulfilment of the requirements for the degree of MSc Chemical Engineering

in the

HySA/Catalysis Centre of Competence
Department of Chemical Engineering

28 June 2019

Plagiarism Declaration

I know the meaning of plagiarism and declare that all the work in the document, save for that which is properly acknowledged, is my own. This thesis/dissertation has been submitted to the Turnitin module (or equivalent similarity and originality checking software) and I confirm that my supervisor has seen my report and any concerns revealed by such have been resolved with my supervisor.

Signed: Signed by candidate

Date: 18/10/2019

"The fear of the LORD *is the beginning of knowledge "*

Proverbs 1:7a (ESV)

"For the LORD *gives wisdom;*
from his mouth come knowledge and understanding; "

Proverbs 2:6 (ESV)

Abstract

The insatiable global demand for energy cannot be sustained by fossil fuels without irreparable damage to the environment. Various alternative energy sources are being investigated to provide renewable clean energy. One promising technology is the hydrogen fuel cell, which uses hydrogen and oxygen to produce electricity. However, the currently used catalyst support material, carbon black, corrodes in the low pH and oxidative environment. Therefore, new catalyst support materials are being sought. A new class of material, called MAX phases, shows potential because some possess a combination of properties of metals and ceramics. Three of them, Ti_2AlC, Ti_3AlC_2, and Ti_3SiC_2, show good electrical conductivity and oxidation resistance. These MAX phases have been investigated using density functional theory (DFT) in this thesis to determine their properties.

The density of states show that they are electrically conductive, with a continuous band over the Fermi level primarily from the Ti d orbital. Calculating the Boltzmann transport properties, yielded electrical resistivity values of 0.460 $\mu\Omega$ m for Ti_2AlC, 0.370 $\mu\Omega$ m for Ti_3AlC_2, and 0.268 $\mu\Omega$ m for Ti_3SiC_2 at 300 K. Therefore, Ti_3SiC_2 should be the most electrically conductive of the three.

The vacancy formation energy of an A group atom was investigated using a 2 x 2 x 2 supercell. The vacancy formation energies were calculated to be 2.882 eV for Ti_2AlC, 2.812 eV for Ti_3AlC_2, and 2.167 eV for Ti_3SiC_2. The formation of a vacancy increases the electrical resistivity of the bulk MAX phases.

As a catalyst support material, a MAX phase particle will have surfaces present. Due to the layered structure of the MAX phases, multiple terminations of (0 0 0 1) surfaces could be possible, which were investigated. It was shown that terminations where the Ti-C cage structure remained intact produced the lowest cleavage energies. For Ti_2AlC, the two low cleavage energy surfaces are Al(Ti) and Ti(C), for Ti_3AlC_2, Al(Ti2) and Ti2(C), and for Ti_3SiC_2, Si(Ti2) and Ti2(C). The surfaces with the lowest cleavage energy should be more stable than other surfaces and would therefore be expected to be present on a MAX phase particle.

Vacancies were also formed in the surface systems. The surfaces with the vacancy in the surface layer had the lowest vacancy formation energy, with that of Si(Ti2) being positive. The surface slabs generally showed a higher electrical resistivity than the bulk systems, while the formation of a vacancy generally increased the resistivity, in agreement with the bulk vacancy trend.

These MAX phases are electrically conductive, however a quantifiable oxidation resistance was not able to be calculated. They do however show signs of being good electrocatalyst support materials.

Acknowledgements

I would like to acknowledge the following individuals and institutions, without whom this thesis would not have been possible.

Firstly, my supervisors: Ms. Tokoloho Rampai, Ms. Tracey van Heerden, and A/Prof. Pieter Levecque. It has been a pleasure working under your guidance. I have never known that research could be as entertaining as it was. Thank you for making this project enjoyable. Your knowledge and insight was incredibly valued, and I can truly say that I have learnt lots from you, not just about this project but about life. Thank you for providing me with this opportunity; I am very grateful.

I wish to acknowledge Mr. Graham Inggs, Mr. Andrew Lewis, and Dr. Anton Lopis for providing access to the high performance computing servers and answering questions about using them. This project would not have been possible without the computational resources provided by the Chemical Engineering Department, the University of Cape Town's ICTS High Performance Computing team (HPC), and the Council for Scientific and Industrial Research's Centre for High Performance Computing (CHPC).

I would like to thank Thobani Gambu for his insight and help with scripts. Thank you for inspiring me with your work, for answering questions, and helping me navigate my first proper conference. I would also like to thank Pierre Cilliers for the modelling manual that he wrote, which was very helpful.

Then, I would like to thank my classmates for the thoroughly enjoyable years: Hassan Moydien, I am so thankful for working together on many projects; Naomi Harrisankar, thank you for the friendship, conversations, food, and all-round fun; Bongani Mtetwa, maybe one day I'll be up to your level of argument, nevertheless I have learnt so much through them; Mark Hambrock, for the laughs while tutoring and advice on computers; Tita Labi, for the friendship and the golf; Ziba Rajan, for the great discussions and inspirational pursuit of excellence; as well as many others.

To my family, friends, and girlfriend, thank you for putting up with me, for supporting me, and for being there for me every step of the way.

This research would not have been possible without funding from HySA/Catalysis and the Department of Chemical Engineering, for which I am very grateful.

Finally, and most importantly, I would like to thank the Father Almighty for giving me this opportunity, for strengthening me, encouraging me, refining me, and giving me life. I would be a very different person, and my soul impoverished, but for You.

Contents

List of Figures

List of Tables

List of Abbreviations

PEMFC	**P**roton **E**xchange **M**embrane **F**uel **C**ell
HOR	**H**ydrogen **O**xidation **R**eaction
ORR	**O**xygen **R**eduction **R**eaction
DFT	**D**ensity **F**unctional **T**heory
HF	**H**artree-**F**ock Theory
SCF	**S**elf-**c**onsistent **f**ield procedure
LDA	**L**ocal **D**ensity **A**pproximation
GGA	**G**eneralised **G**radient **A**pproximation
PW91	**P**erdew-**W**ang 19**91** functional
PBE	**P**erdew-**B**urke-**E**rnzerhof functional
RPBE	**R**evised **P**erdew-**B**urke-**E**rnzerhof functional
VASP	**V**ienna *Ab-initio* **S**imulation **P**ackage
CASTEP	**Ca**mbridge **S**equential **T**otal **E**nergy **P**ackage
DOS	**D**ensity **o**f **S**tates
BTE	**B**oltzmann **T**ransport **E**quation
RMSE	**R**oot-**m**ean-**s**quare **e**rror
EOS	**E**quation **o**f **s**tate
B-M	**B**irch-**M**urnaghan EOS

List of Symbols

S	Seebeck coefficient	$\mu V\,K^{-1}$
E_f	Fermi level energy	eV
T	Temperature	K or °C
zT	Thermoelectric figure of merit	dimensionless
E_t	Total energy	eV
A	Surface area	m^2
V	Unit cell volume	$Å^3$
B	Bulk modulus	GPa
E_C	Cleavage energy	eV or $J\,m^{-2}$
d	d-band centre	eV
E_V	Vacancy formation energy	eV
σ	Electrical conductivity	$S\,cm^{-1}$ ($\Omega^{-1}\,cm^{-1}$)
ρ	Resistivity	$\mu\Omega\,m^{-1}$
κ	Thermal conductivity	$W/(mK)$
τ	Relaxation time	s
γ	Surface energy	$J\,m^{-2}$
μ	Chemical potential	eV

1. Introduction

1.1. Background

In the 21st century, mankind has become increasingly reliant on electricity for nearly everything. This energy sustains life by enabling the cooking of food, providing warmth and being integral to most jobs and healthcare systems. However, the world has come to realise that its dependence on fossil fuels is negatively impacting the environment through the emission of greenhouse gases, potentially causing catastrophic damage to the ability of the planet to support life in the future.

Therefore, extensive research has been undertaken to investigate other means of energy creation. Consequently, various possibilities are being touted as the future of energy creation such as solar power, wind power, and batteries. One of the most promising sources of energy is hydrogen. Hydrogen is the most abundant element in the solar system and is one of the primary sources of fuel of the sun. One of the ways that hydrogen is envisaged for future use is through hydrogen fuel cells. These fuel cells are promising because they use hydrogen from a tank and oxygen from the air to produce electricity. The added bonus of fuel cells is that they do not produce any greenhouse gases, since only water is produced in the chemical reaction.

The compatriote to hydrogen fuel cells is electrolysers. These take water and split it into its constituent elements, hydrogen and oxygen. One of the primary problems with these technologies at present is that they are not commercially cost effective. Thus, much research and development of new materials is being conducted to help commercialise these technologies. However, competitive costing alone will not achieve a green hydrogen economy without a unified vision of government allowing renewable energy to hold more of the energy generation market share.

One of the components holding back hydrogen fuel cells from commercialisation is the catalyst support material. Currently, carbon black is used as the support material and platinum is used as the catalyst (Sharma & Pollet, 2012). Carbon black has good electrical conductivity and a high surface area, however, the durability of carbon black is poor as it oxidises under the low pH conditions found in a hydrogen fuel cell. Although ample research has already been conducted to try and replace carbon black, nothing has yet succeeded it.

A new class of material was discovered in 1996 called MAX phases. These exhibit remarkable properties, showing both metallic and ceramic characteristics (Barsoum & El-Raghy, 1996). Some of the MAX phases show good electrical conductivity and good oxidation resistance (Barsoum & Radovic, 2011). However, there are more than 70 different types of MAX phase, depending on which elements are used. To try to synthesis each combination

in the laboratory and test them as a catalyst support material in a fuel cell would be highly time-consuming and cost inefficient. Therefore, some sort of screening method would be beneficial. This would be able to predict the properties of the materials and determine the best candidates for laboratory testing.

Such a screening tool exists, which is able to predict the properties of materials. It is called density functional theory (DFT). It conducts an atomic level simulation of a crystalline material to calculate the energy of that material, which can then be used to determine other properties of that material. This is further explained in Section 2.4.

This project aims to use DFT to investigate the properties of some of these MAX phases, Ti_2AlC, Ti_3AlC_2, and Ti_3SiC_2, in the hope of providing some insight into their structure and properties, and paving a way forward to investigate other MAX phases.

1.2. Scope

This project looks at three different MAX phases: Ti_2AlC, Ti_3AlC_2, and Ti_3SiC_2. It aims to determine some of the mechanical properties of these materials, such as the bulk modulus, but not all the mechanical properties that would be of interest to a materials scientist. The effect of changing the stoichiometric ratio using the same elements of a MAX phase will be investigated by looking at Ti_2AlC and Ti_3AlC_2. Furthermore, the effect of changing the A group atom will be determined through Ti_3AlC_2 and Ti_3SiC_2. The electrical conductivity of the materials is able to be determined using results obtained from DFT, and thus will be calculated. The oxidation resistance of a material is more difficult to determine using computational methods. To gain an insight into the oxidation resistance, the vacancy formation energy of an A group atom will be investigated.

2. Literature Review

2.1. Hydrogen Fuel Cells

Hydrogen fuel cells utilise hydrogen, fed to the anode, and oxygen, fed to the cathode, to produce electricity, with water as the only reaction product. Hydrogen is oxidised at the anode in the hydrogen oxidation reaction (HOR), shown in Equation 2.2. The hydrogen proton then travels through the proton exchange membrane (PEM) to the cathode, where oxygen is reduced in the oxygen reduction reaction (ORR), indicated by Equation 2.1 (Sui et al., 2017). The overall reaction, depicted by Equation 2.3, shows that water is the only chemical reaction product that is generated within a hydrogen fuel cell. Thus, hydrogen fuel cells do not generate greenhouse gases, which makes them a promising method for producing electricity.

$$\frac{1}{2}\,O_2 + 2\,H^+ + 2\,e^- \rightleftharpoons H_2O \tag{2.1}$$

$$H_2 \rightleftharpoons 2\,H^+ + 2\,e^- \tag{2.2}$$

$$H_2 + \frac{1}{2}\,O_2 \rightleftharpoons H_2O + \text{electricity} + \text{heat} \tag{2.3}$$

The full fuel cell is called a proton exchange membrane fuel cell (PEMFC), as the hydrogen protons are able to migrate through the PEM while the electrons travel through an external circuit, enabling the flow of current. To facilitate current flow, the catalyst support material needs to be electrically conductive. An ionomer is mixed with the catalyst layer to connect the catalyst layer to the PEM to facilitate movement of the protons.

The PEMFC is not the only fuel cell being researched. Other fuel cells include the direct methanol fuel cell (DMFC), however this produces CO_2 as a reaction product, and therefore is not as green as the PEMFC (Sharma & Pollet, 2012: 97).

One of the requirements for a PEMFC catalyst is that it needs to facilitate the so-called "three-phase boundary," where the active catalyst material needs to be in contact with an electrically conductive material, a proton transfer material, and be available for gases to reach it (Liu et al., 2011). This is illustrated in Figure 2.1.

It has been shown that platinum (Pt) is the most active catalyst of the different metals investigated based on the binding energy for the ORR (Figure 2.2), since Pt binds oxygen neither too strongly nor too weakly (Nørskov et al., 2004). Most catalysts for PEMFCs consist of Pt

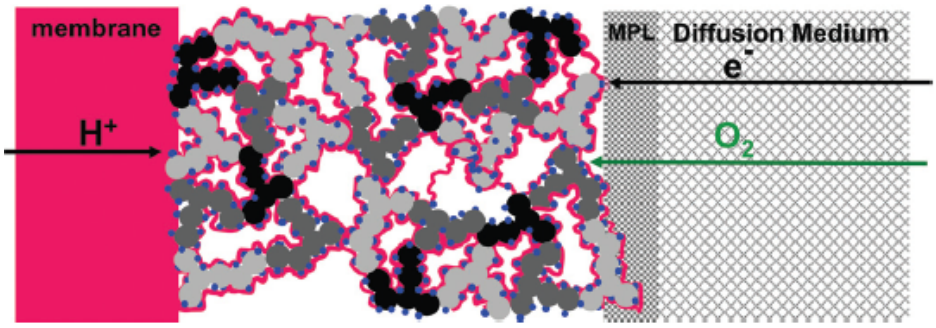

FIGURE 2.1: Theoretical sketch of the three-phase boundary showing the catalyst support, platinum particles and membrane with ionomers (Liu et al., 2011)

supported on carbon black, as carbon black has a high surface area and has a good electrical conductivity. To allow proton transfer, an ionomer is mixed into the catalyst, which is connected to the PEM.

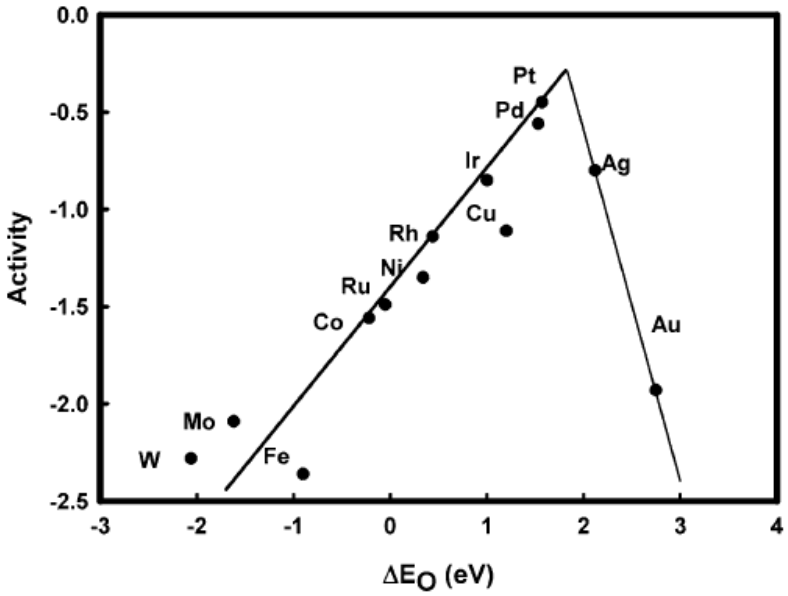

FIGURE 2.2: Oxygen reduction activity plotted as a function of oxygen binding energy (Nørskov et al., 2004)

A single cell consists of a catalyst layer and a gas diffusion layer either side of a proton exchange membrane, together termed the membrane electrode assembly. To either side of this, a bipolar plate is attached, which has gas channels and is electrically conductive. Typically, a single cell in a low temperature PEMFC operates at voltages between 0.6 and 0.9 V. Multiple cells are then stacked together to form a fuel cell stack, which then provides a higher voltage. A normal operating temperature for a fuel cell stack is around 80 °C, with gas pressures that are slightly above atmospheric pressure (Borup et al., 2007).

2.1.1. Fuel Cell and Support Requirements

The electrocatalyst support material has a large influence over the performance, efficiency and durability of a PEMFC (Sharma & Pollet, 2012). The majority of electrocatalyst support materials used are porous and conductive. The porosity allows for large numbers of catalyst nanoparticles to be deposited on the surface of the support material, which creates a large surface area of the catalyst particles. The small nanoparticle size coupled with the large number of nanoparticles creates a large overall catalyst surface area. A large surface area also increases the probability of the catalyst being in contact with the support material and the ionomer proton membrane at the same time. However, the predominantly used catalyst support material – carbon – undergoes corrosion under high operating electrical potentials (Shao et al., 2007; Sharma & Pollet, 2012). It is therefore vital for the commercialisation of hydrogen fuel cells that a support material which is both corrosion resistant and electrically conductive, with a high surface area, be developed.

Some other factors that have been investigated relating to the improvement of hydrogen fuel cells are: reducing catalyst loading, decreasing catalyst particle size, investigating new methods to aid in mass transfer to electrode surfaces, improving the durability of carbon-based support materials, increasing the performance of carbon-based support materials, and substitution of Pt catalyst for other elements (Shao et al., 2007; Sharma & Pollet, 2012; Zhang et al., 2009).

The following factors are the predominant characteristics affecting the choice of electrocatalyst support materials: electrical conductivity, interactions between support and catalyst, surface area, porosity of support structure, and resistance to oxidation (Sharma & Pollet, 2012: 97). These factors, in turn, determine the cost of the fuel cell catalyst and the durability of the catalyst.

2.1.2. Alternative Electrocatalyst Support Materials

Currently, the most commonly used electrocatalyst support material is carbon black, since it displays a high electrical conductivity ($4.0\,\mathrm{S\,cm^{-1}}$, Pantea et al. (2001)) and a high surface area (Vulcan XC-72R has a surface area of $250\,\mathrm{m^2/g}$ (Sharma & Pollet, 2012: 97)). Other carbon support materials have been investigated, including carbon nanotubes, carbon nanofibers, nanodiamonds, and graphenes. These all display combinations of high electrical conductivity, high surface areas, and stability in acidic environments, but often perform poorly in another area. Additionally, not all materials have yet been tested under actual fuel cell conditions.

Various non-carbon support materials have also been investigated, including titania, indium oxide, silica, silicon carbide (Lv et al., 2010), alumina, tungsten oxide nanostructures, and polymers. The primary focus for using non-carbon-based support materials is to circumvent the carbon corrosion problem (Sharma & Pollet, 2012: 97). However, none of these materials has succeeded in replacing carbon black, each for its own reason. Although much

research has been conducted into this field, the problem of carbon corrosion remains unresolved, since each alternative support material fails to fulfil at least one of the requirements for PEMFC electrocatalyst support materials.

Some of the requirements needed by electrocatalyst support materials include the following: electrical conductivity, thermal stability, and chemical stability (especially under highly acidic conditions of pH 0 – 1). A new class of material has recently been developed that fulfils all these criteria (Magnuson & Mattesini, 2017). These new materials are called MAX phases. Since they satisfy all these conditions, they could be a promising alternative to be used in PEMFCs as an electrocatalyst support material.

2.2. MAX Phases

The $M_{n+1}AX_n$ phases, where n = 1, 2, or 3, shortened to MAX phases, are a new class of materials that combine some of the properties of ceramics and metals (Barsoum, 2000). The acronym MAX consists of a group of elements represented by each letter, where M is an early transition metal, A is a group A (usually IIIA or IVA) element, and X is either C or N (see Figure 2.3).

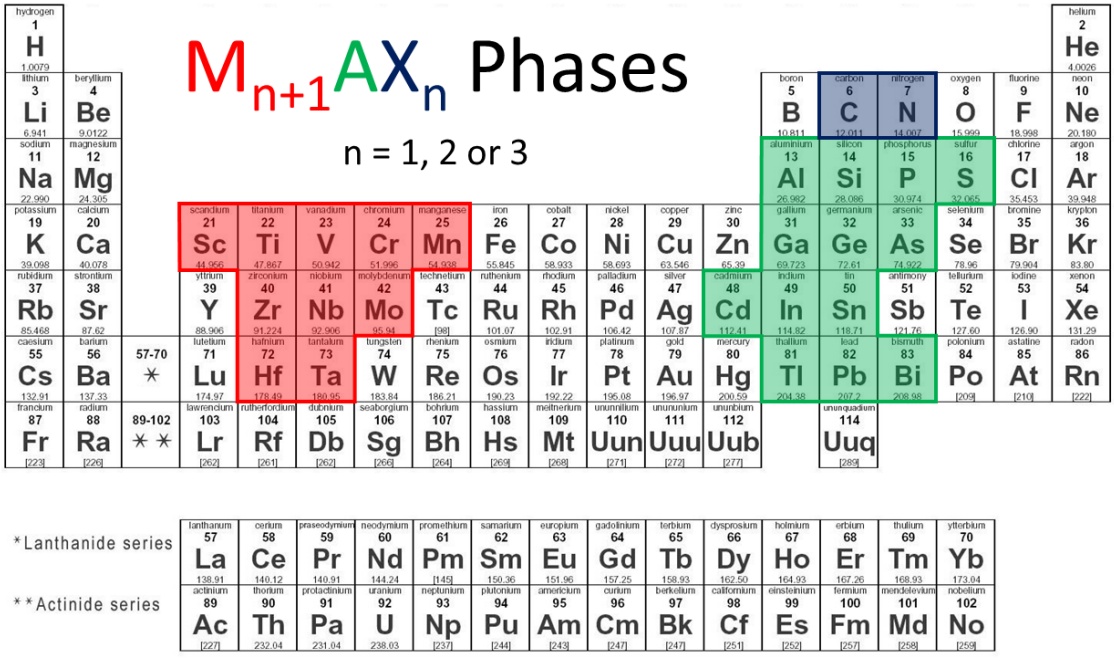

FIGURE 2.3: Periodic table showing elements within the MAX phase class (adapted from Sun (2011))

The MAX phases were discovered in the 1960s by Nowotny and his colleagues and were initially termed the H phases (Jeitschko & Nowotny, 1967; Nowotny, 1971). Most of these compounds were of the form M_2AX, otherwise called the 211 phases. However, these were only 90-92% dense (Barsoum, 2013: 4). Later, Ti_3SiC_2 (Jeitschko & Nowotny, 1967), Ti_3GeC_2 (Wolfsgruber et al., 1967), and Ti_3AlC_2 (Pietzka & Schuster, 1994, 1996) were discovered, but they were not able to be produced as single-phase, bulk, dense samples (Barsoum, 2013: 4).

Research into the MAX phases was reawakened in 1996 when Barsoum successfully synthesised predominantly single-phase titanium silicon carbide, Ti_3SiC_2, with high purity and reported on the notable physical and mechanical properties (Barsoum & El-Raghy, 1996). Since then research into the field has dramatically increased, with over 1500 articles published by 2016 on Ti_3SiC_2 alone, according to the Institute of Scientific Information (Bai et al., 2017: 2).

The reason these new materials have garnered so much interest in under two decades is because of their unique combination of properties. Some MAX phases combine certain properties of metals and ceramics, creating materials that are elastically stiff but relatively soft and machinable, are damage tolerant and fracture tough, as well as being oxidation, thermal shock, creep, and fatigue resistant, while still being electrically and thermally conductive (Barsoum, 2006; Barsoum & Radovic, 2011). They display these characteristics partially due to the unique layered structure that they possess. Figure 2.4 shows the unit cells of the M_2AX (211), M_3AX_2 (312) and M_4AX_3 (413) phases, which shows how MAX phases consist of $M_{n+1}X_n$ layers interleaved by sheets of A atoms.

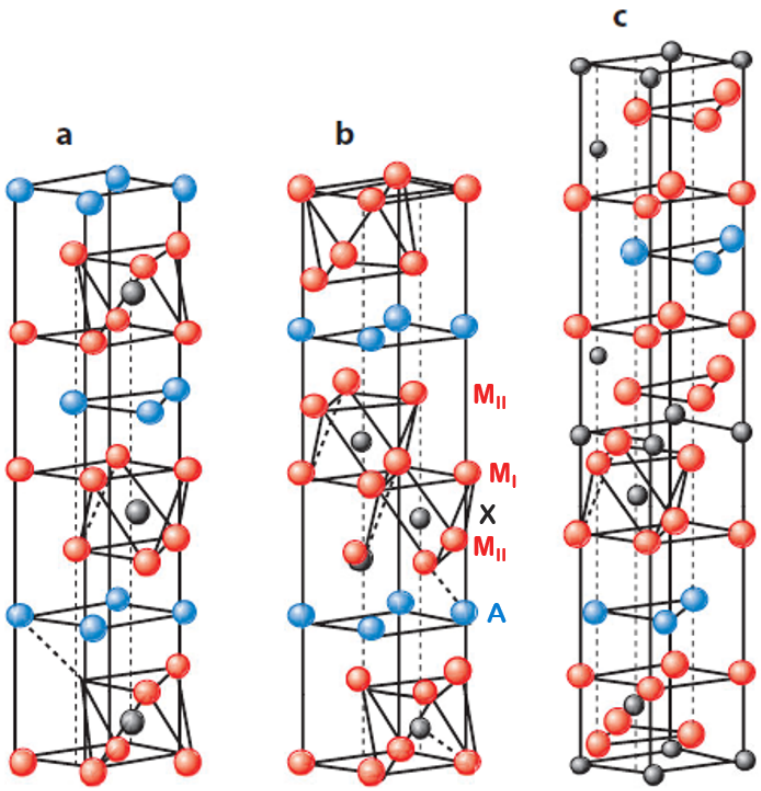

FIGURE 2.4: Unit cell structure of a) 211, b) 312 and c) 413 MAX phases (adapted from Barsoum & Radovic (2011: 196)).

Review papers have been published by Barsoum (2000, 2006), Barsoum & Radovic (2011), Eklund et al. (2010), Hu et al. (2013), Magnuson & Mattesini (2017), and Wang & Zhou (2010) detailing the progress of MAX phase synthesis. To date, there are 70 known MAX phases that have been synthesised (see Table 2.1). Additionally, there are over 30 solid solutions of MAX phases that have also been synthesised, where predominantly a mixture of M or X

elements is seen (Magnuson & Mattesini, 2017). There are, however, 5 MAX phases where the A atom contains a mixture of two elements (Cabioch et al., 2013; Etzkorn et al., 2009; Horlait et al., 2016; Yu et al., 2010). MAX phases with an n of 4, 5, or 6 have been seen in experiments, although there have been no samples without other compounds present reported to date (Bai et al., 2017: 3). Another interesting MAX phase-type structure that has been synthesised is $Ti_5Al_2C_3$, which consists of a usual MAX phase structure layering with alternating M_2X and M_3X_2 layers in between the A layers, i.e. A — M_2X — A — M_3X_2 — A (Lane et al., 2012).

TABLE 2.1: Known ternary MAX phases grouped according to electronic configuration (modified from Hug (2006))

M atoms		**A group**				
		s^2	**s^2p^1**	**s^2p^2**	**s^2p^3**	**s^2p^4**
3d	Sc		Sc_2InC			
	Ti	Ti_2CdC	Ti_2AlC, Ti_2GaC, Ti_2InC, Ti_2TlC, Ti_2AlN, Ti_2GaN, Ti_2InN, Ti_3AlC_2, Ti_3GaC_2, Ti_3InC_2, Ti_4GaC_3, Ti_4AlN_3	Ti_2GeC, Ti_2SnC, Ti_2PbC, Ti_3SiC_2, Ti_3GeC_2, Ti_3SnC_2, Ti_4SiC_3, Ti_4GeC_3		Ti_2SC
	V		V_2AlC, V_2GaC, V_2GaN, V_3AlC_2, V_4AlC_3	V_2GeC	V_2PC, V_2AsC	
	Cr		Cr_2AlC, Cr_2GaC, Cr_2GaN	Cr_2GeC		
	Mn		Mn_2GaC			
4d	Zr		Zr_2AlC, Zr_2InC, Zr_2TlC, Zr_2InN, Zr_2TlN, Zr_3AlC_2	Zr_2SnC, Zr_2PbC		Zr_2SC
	Nb		Nb_2AlC, Nb_2GaC, Nb_2InC, Nb_4AlC_3	Nb_2GeC, Nb_2SnC	Nb_2PC, Nb_2AsC	Nb_2SC
	Mo		Mo_2GaC			
5d	Hf		Hf_2InC, Hf_2TlC	Hf_2SnC, Hf_2PbC, Hf_2SnN		Hf_2SC
	Ta		Ta_2AlC, Ta_2GaC, Ta_3AlC_2, α-Ta_4AlC_3, β-Ta_4AlC_3			

One of the potential applications that has been proposed is the use of MAX phases as nuclear fuel cladding (Horlait et al., 2016; Lapauw et al., 2016a,b). In particular, zirconium (Zr) MAX phases have been proposed as potential substitutes for the zirconium alloy currently used. Investigations into these MAX phases have led to the successful synthesis of Zr_2AlC and Zr_3AlC_2, which were previously thought to not be stable. At the same time, extensive research has been carried out on some of the earliest MAX phases that were discovered, especially in characterising those MAX phases. However, although other applications have been proposed for different MAX phases such as engine parts, heating elements, and electrical contacts (Magnuson & Mattesini, 2017: 127), actual implementation of MAX phases is yet to be widely employed.

Investigations have been conducted into the corrosion resistance of different MAX phases in acids, with HCl and H_2SO_4 being used to determine corrosion behaviour. Jovic & Barsoum (2004) noted that Ti_3SiC_2 is more corrosion resistant than pure Ti in HCl due to the formation

of SiO_2 on the surface of Ti_3SiC_2. The SiO_2 passivates the corrosion behaviour. Jovic et al. (2006) agreed with this result and investigated a variety of MAX phases including Ti_2AlC and Ti_3SiC_2 in HCl and H_2SO_4. They concluded that Ti_3SiC_2 is stable in both solutions, but Ti_2AlC dissolves in HCl. Li et al. (2010) studied Ti_3AlC_2 electrochemically over 24 hours in H_2SO_4 and concluded that it was not long-term corrosion resistant. Xie et al. (2012) used hot concentrated HCl solution to investigate Ti_3SiC_2, Ti_3AlC_2, and Ti_2AlC, amongst other MAX phases. They concluded that Ti_3SiC_2 displayed excellent corrosion resistance, while Ti_3AlC_2 experienced severe corrosion. Furthermore, Ti_2AlC displayed a poorer corrosion resistance than Ti_3AlC_2 (see Table 2.2).

TABLE 2.2: Experimental corrosion extent of MAX phases after 24 h in 200 °C HCl, where the corrosion extent is the amount of MAX phase corroded away according to Rietveld quantitative phase analysis (Xie et al., 2012)

MAX phase	**Corrosion extent**
Ti_3SiC_2	6.8 %
Ti_3AlC_2	72.7 %
Ti_2AlC	100 %

Xie et al. (2012) found that during corrosion, the Al atoms are the first to be corroded away, leaving the TiC layers exposed. This then allows the corrosion of Ti atoms and the formation of rutile TiO_2. It was proposed that the reason Ti_3AlC_2 did not corrode as extensively as Ti_2AlC is due to the thickness of the TiC layer. In Ti_2AlC, once the Al is corroded away, all the Ti atoms are exposed; however, in Ti_3AlC_2, not all the Ti atoms are exposed after Al corrosion. This causes Ti_3AlC_2 to corrode slower. Xie et al. (2012) show that after corrosion in HCl the sample contains predominantly rutile, not the MXene form of Ti_2AlC or Ti_3AlC_2. A MXene is formed when the A group element is removed from the MAX phase structure, yet the layered structure of the MAX phase is maintained, leaving 2D sheets of M_2X, M_3X_2, or M_4C_3, corresponding to the 211, 312, or 413 MAX phase (Naguib et al., 2011). If the Al MAX phases corroded to form the MXene, the material would maintain its electrical conductivity (Naguib et al., 2014) and the removal of the Al atoms would slow the rate of corrosion; however, this does not occur. Corrosion from HCl is therefore detrimental to the electrical conductivity of the Al MAX phases, since TiO_2 is not conductive.

The corrosion of these MAX phases has not been compared with the corrosion of carbon, nor has perchloric acid been used as a corrosive agent, therefore there is still room for investigation into the comparative rate of MAX phase corrosion against carbon, and MAX phase corrosion in perchloric acid. Additionally, corrosion at 80 °C has not been studied, which is the operating temperature of a PEMFC.

Other corrosion tests that have been conducted investigate the corrosion resistance of MAX phases including Ti_2AlC and Ti_3AlC_2 in air. These have shown that the MAX phases need to be heated up to a temperature of around 800 °C before corrosion takes place (Barsoum et al., 2001). When Ti_3SiC_2 is heated to 900 °C and above in air, layers of silica and titania form underneath an outer layer of rutile (Barsoum et al., 1997).

The experimental resistivity of different MAX phases, the inverse of electrical conductivity, is reported in the literature. These are shown in Table 2.3. They are compared against other materials.

TABLE 2.3: Electrical resistivity at 300 K of MAX phases and other compounds from literature

Material	Resistivity ($\mu\Omega$ m)	Source
Ti_2AlC	0.44	Magnuson & Mattesini (2017)
	0.36	Scabarozi et al. (2008)
Ti_3AlC_2	0.5	Magnuson & Mattesini (2017)
	0.353	Scabarozi et al. (2008)
	0.287	Wang & Zhou (2002a)
Ti_3SiC_2	0.25	Magnuson & Mattesini (2017)
	0.23	Barsoum (2000)
Carbon black	2.5×10^3	Pantea et al. (2001)
SiC	5×10^6	Kim et al. (2015a)
TiC	2	Hollander (1961)
Aluminium	0.0265	Serway (1998: 602)
Titanium	1.59	Ito et al. (2006)

The three most studied MAX phases are Ti_3SiC_2, Ti_3AlC_2 and Ti_2AlC. These show good resistance to oxidation and good electrical conductivity (Barsoum & Radovic, 2011; Wang & Zhou, 2010). These will therefore be the best to investigate since there is plenty of experimental data to validate the model against. Once this is completed, it will then be possible to investigate MAX phases that have not been studied as well, without needing to synthesise them to test them as electrocatalyst support materials.

2.3. Quantum Mechanical Modelling Methods

Molecular modelling methods provide means with which to understand the underlying reasons for experimental phenomenon. Different tools allow insight into electronic properties, mechanical properties, bond breaking and formation processes, thermodynamic stability, transport properties, and reaction processes, to name but a few. Along with the many calculation outcomes obtainable come many calculation routes. While each method aims to model atoms, each does it with a different modus operandi. For example, density functional theory (DFT) aims to model the electrons of a small system of atoms, usually in the tens of atoms. Molecular dynamics (MD) applies a classical physics approach using hard spheres and springs to represent atoms and bonds, allowing for a much larger ensemble of atoms, often in the order of hundreds of atoms.

In molecular systems where the bond characteristics are of interest it is necessary to use *ab-initio*, or first-principle, methods, which ultimately aim to solve the Schrödinger Equation (Schrödinger, 1926). The time-independent Schrödinger equation is given by:

$$\hat{H}\Psi = E\Psi \tag{2.4}$$

with

$$\hat{H} = \hat{T} + \hat{V}_{ne} + \hat{V}_{ee} \tag{2.5}$$

where $\hat{H}$ is the Hamiltonian operator, E is the energy of the system, Ψ is the wavefunction of the system, $\hat{T}$ represents the kinetic energy operator, and $\hat{V}$ is the operator that describes the potential of the electron-nucleus attraction $\hat{V}_{ne}$ and the electron-electron repulsion $\hat{V}_{ee}$ (Parr & Yang, 1989). For the one electron atom, the Schrödinger equation can be rewritten as:

$$\left[\frac{-h^2}{8\pi^2 m}\nabla^2 + v_{eff}\right]\Psi(r) = E\Psi(r) \tag{2.6}$$

where h is Planck's constant, m is the mass of the electron, ∇^2 is the second derivative operator, and v_{eff} is the effective potential of the electron (Lewars, 2011: 118).

For the one electron system, the Schrödinger equation can be solved exactly; however there is no exact solution for systems with more than one electron, therefore approximations need to be made. A fundamental approximation for multi electron systems is the Born-Oppenheimer approximation (Born & Oppenheimer, 1927). This assumes that electrons move much faster than nuclei because of the difference in mass. This decouples Equation 2.4 into nuclear and electronic components. As the nuclei can be considered as point charges, only the solution to the wavefunction of the electrons needs to be solved (Greeley et al., 2002).

To approximate the potential that a single electron feels, Hartree-Fock (HF) Theory assumes that electrons are independent particles and will experience an effective potential (v_{eff}) from the nuclei and other electrons. The HF method approximates the wavefunction of the system using an anti-symmetric product of each one-electron wavefunction using the Slater determinant. The anti-symmetric nature ensures that electrons in the same orbital obey the Pauli Exclusion Principle, which states that two electrons cannot be in the same quantum state and must possess different spins. This enables systems to be reduced to the one electron electronic Schrödinger equation (Equation 2.6), which can then be solved. This requires an iterative procedure, since v_{eff} depends on the wavefunction, which is initially approximated and v_{eff} calculated, before a new wavefunction is generated. This iterative process is repeated until convergence of the wavefunction is achieved. This process is termed the self-consistent field (SCF) procedure.

HF theory fails to take into account electron correlation effects, resulting in inaccurate molecular energies (Greeley et al., 2002). Another drawback with using HF theory is the large computational cost associated with it. The HF method has a large number of degrees

of freedom and requires numerous calculations before self-consistency is achieved (N^4 calculations, where N is the number of basis set functions). Hence, for modelling of realistic systems with many electrons other methods are preferred. Density functional theory is one such procedure that has yielded a better computational cost while maintaining sufficient accuracy. DFT employs a different approach to determining the wavefunction by using an effective electron correlation based on the number of basis sets, which scales much more favourably for larger systems, scaling with N^3 calculations (Greeley et al., 2002). Additionally, for a wave function calculation, there are $4n$ variables $(x, y, z, spin)$ that need to be solved, with n being the number of electrons; however, for DFT calculations, only three variables (x, y, z) are required (Lewars, 2011: 446).

2.4. Density Functional Theory

Density functional theory (DFT) was developed by Hohenberg and Kohn when they showed that the ground state energy of a system could be uniquely determined using the electron density of the system (Hohenberg & Kohn, 1964). The electron density, $\rho_0(\mathbf{r})$, can therefore replace the costly determination of the many-body wavefunction[1]. This is shown in Equation 2.7.

$$E_0 = F\left[\rho_0(\mathbf{r})\right] = E\left[\rho_0(\mathbf{r})\right] \tag{2.7}$$

Solving for E_0 involves using a trial density ρ_t, which must satisfy the condition:

$$\int \rho_t(\mathbf{r}) d\mathbf{r} = N \tag{2.8}$$

where N is the total number of electrons of the system. Additionally, the trial density cannot be negative (Lewars, 2011: 450).

Solving for the energy was further developed using Kohn-Sham theory (Kohn & Sham, 1965), which suggested that the $F\left[\rho_0(\mathbf{r})\right]$ term could be found using the kinetic and potential energy contributions. Thus, the energy is expanded to be represented using three terms, the kinetic energy T, nucleus-electron potential energy V_{ne}, and electron-electron potential energy V_{ee} (Lewars, 2011: 451).

$$E_0 = \langle T[\rho_0] \rangle + \langle V_{ne}[\rho_0] \rangle + \langle V_{ee}[\rho_0] \rangle \tag{2.9}$$

Each energy term of this equation denoted by $\langle \quad \rangle$ are called quantum-mechanical average values, otherwise termed "expectation values". The nucleus-electron potential energy $\langle V_{ne} \rangle$ can be expanded simply as:

[1]Most of the derivation of the various DFT equations is from Lewars (2011), with additional input from Parr & Yang (1989) and Springborg (1997).

$$\langle V_{ne} \rangle = \int \rho_0(\mathbf{r}) v(\mathbf{r}) d\mathbf{r} \tag{2.10}$$

This can be expanded in terms of the attraction potential of the nuclei A and the electron i over a distance **r**.

$$\int \rho_0(\mathbf{r}) v(\mathbf{r}) d\mathbf{r} = \int \left[\rho_0(\mathbf{r}_1) \sum_{nuclei\ A} -\frac{Z_A}{\mathbf{r}_{1A}} \right] d\mathbf{r}_1 = - \sum_{nuclei\ A} Z_A \int \frac{\rho_0(\mathbf{r}_1)}{\mathbf{r}_{1A}} d\mathbf{r}_1 \tag{2.11}$$

Unfortunately, the expansion of kinetic energy $\langle T[\rho_0] \rangle$ and electron-electron potential energy $\langle V_{ee}[\rho_0] \rangle$ terms is not as straightforward. Therefore, the idea of a fictitious reference system was employed. This reference system would yield the same electron density as the real system while using non-interacting electrons (Kohn & Sham, 1965). The deviation of the kinetic energy operator was represented by:

$$\Delta \langle T[\rho_0] \rangle \equiv \langle T[\rho_0] \rangle - \langle T[\rho_0] \rangle_{ref} \tag{2.12}$$

The same can be done for $\langle V_{ee}[\rho_0] \rangle$, however, here the reference state can be know exactly from the classical charge-cloud coulomb repulsion energy (Lewars, 2011: 453). This can be expressed as:

$$\Delta \langle V_{ee}[\rho_0] \rangle = \langle V_{ee}[\rho_0] \rangle - \frac{1}{2} \iint \frac{\rho_0(\mathbf{r}_1) \rho_0(\mathbf{r}_2)}{\mathbf{r}_{12}} d\mathbf{r}_1 d\mathbf{r}_2 \tag{2.13}$$

The last term includes the summation over pairs of infinitesimal volume elements $\rho_0(\mathbf{r}_1)$ and $\rho_0(\mathbf{r}_2)$, separated by the distance $\mathbf{r}_{12}$. The energy equation can now be written as:

$$E_0 = \int \rho_0(\mathbf{r}) v(\mathbf{r}) d\mathbf{r} + \langle T[\rho_0] \rangle_{ref} + \frac{1}{2} \iint \frac{\rho_0(\mathbf{r}_1) \rho_0(\mathbf{r}_2)}{\mathbf{r}_{12}} d\mathbf{r}_1 d\mathbf{r}_2 + \Delta \langle T[\rho_0] \rangle + \Delta \langle V_{ee}[\rho_0] \rangle \tag{2.14}$$

Here, everything is known except the last two Δ terms. The sum of these two terms are called the exchange-correlation energy, simplified as:

$$E_{XC}[\rho_0] \equiv \Delta \langle T[\rho_0] \rangle + \Delta \langle V_{ee}[\rho_0] \rangle \tag{2.15}$$

In Equation 2.14, the first and third terms can be determined exactly if the ground state electron density is known. The second term, $\Delta \langle T[\rho_0] \rangle$, for the ground state wave function of the reference system, is the expectation value of the sum of the one-electron kinetic operators (Lewars, 2011; Parr & Yang, 1989). This can be represented as:

$$\langle T[\rho_0]\rangle_{ref} = \left\langle \psi_r \middle| \sum_{i=1}^{2n} -\frac{1}{2}\nabla_i^2 \middle| \psi_r \right\rangle \tag{2.16}$$

Due to the hypothetical electrons being non-interacting, the wave function ψ_r can be written using a Slater determinant of occupied spin molecular orbitals (Lewars, 2011: 454). Each element of the Slater determinant can be written as the product of a Kohn-Sham orbital ψ_i^{KS} and a spin function α or β. Applying Slater-Condon rules for simplifying integrals yields the following equation:

$$\langle T[\rho_0]\rangle_{ref} = -\frac{1}{2}\sum_{i=1}^{2n} \left\langle \psi_i^{KS} \middle| \nabla_i^2 \middle| \psi_i^{KS} \right\rangle \tag{2.17}$$

One therefore only has to solve the Kohn-Sham spatial orbitals to calculate the electronic kinetic energy of the non-interacting electrons reference system. The only term left to determine is the elusive exchange-correlation term, $E_{XC}[\rho_0(\mathbf{r})]$. This has been one of the major problems with DFT, in that such a functional exists but is unknown. Calculating the exchange-correlation potential involves the derivation of E_{XC} by $\rho(\mathbf{r})$, since E_{XC} depends on $\rho(\mathbf{r})$. The exchange-correlation potential is defined as:

$$v_{XC}(\mathbf{r}) = \frac{\delta E_{XC}[\rho(\mathbf{r})]}{\delta\rho(\mathbf{r})} \tag{2.18}$$

This leads to the Kohn-Sham equations (Lewars, 2011: 455; Parr & Yang, 1989: 154):

$$\left[-\frac{1}{2}\nabla_i^2 - \sum_{nuclei\ A}\frac{Z_A}{\mathbf{r}_{1A}} + \int\frac{\rho(\mathbf{r}_2)}{\mathbf{r}_{12}}d\mathbf{r}_2 + v_{XC}(1)\right]\psi_i^{KS}(1) = \varepsilon_i^{KS}\psi_i^{KS}(1) \tag{2.19}$$

There are various approximations for the exchange-correlation functional that have been proposed, each with their own accuracy and computational cost. Local-density approximation (LDA) looks at the density at a specific co-ordinate and has the lowest computational cost. This can be represented as (Perdew et al., 2005):

$$E_{XC}^{LDA}[\rho(\mathbf{r})] = \int d\mathbf{r}\,\rho(\mathbf{r})\,\varepsilon_{XC}^{LDA}(\rho(\mathbf{r})) \tag{2.20}$$

LDA has a variation termed local spin density approximation (LSD), which separates the electrons with opposite spins into different Kohn-Sham orbitals. This is able to handle unpaired electrons easier than LDA, but for systems with paired electrons, LSD and LDA are equivalent (Lewars, 2011: 462).

Generalised gradient approximation (GGA) accounts for the gradient of electron density by building on the LDA model, which is more accurate for systems with electron density gradients. GGA takes into account the electron gradient in addition to the local electron density, which can be represented as (Perdew et al., 2005):

$$E_{XC}^{GGA}[\rho(\mathbf{r})] = \int d\mathbf{r}\, \rho(\mathbf{r})\, \varepsilon_{XC}^{GGA}(\rho(\mathbf{r}), \nabla\rho(\mathbf{r})) \tag{2.21}$$

More accurate models, such as the meta-GGA and the hybrid functional models, build on the GGA model but require a much higher computational cost without yielding significantly different results in most studies (Bai et al., 2017: 6). These seek to "climb" up what has been called the Jacob's ladder of functionals (Figure 2.5) to higher and more accurate functionals. The top of this ladder would be an exact exchange-correlation functional.

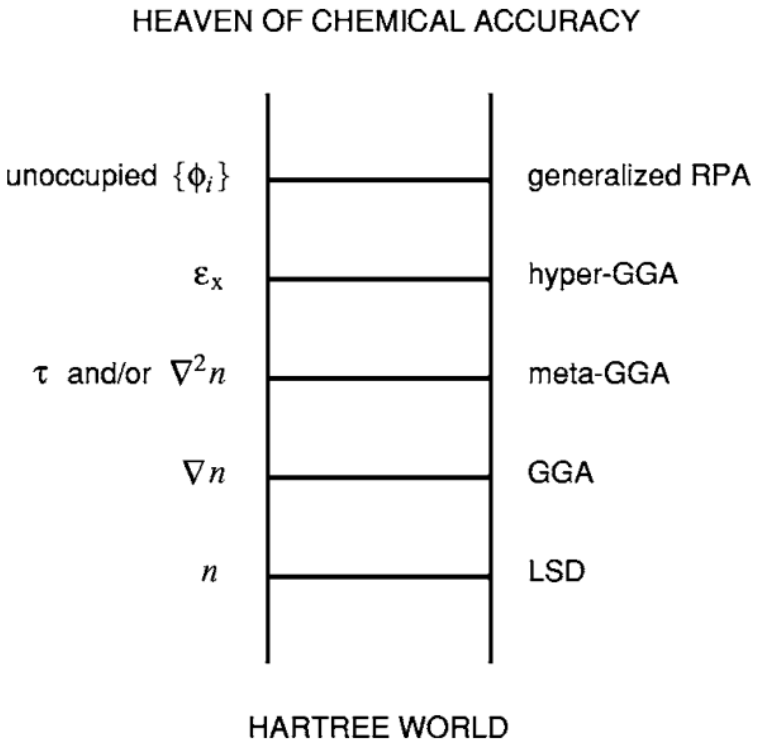

FIGURE 2.5: Jacob's ladder of exchange-correlation functionals (Perdew et al., 2005). Here, n has been used for density.

In the field of catalysis, there are two programs that are predominantly used to conduct DFT calculations: Vienna *Ab-initio* Simulation Package (VASP) and Cambridge Sequential Total Energy Package (CASTEP). These are based on the plane-wave pseudopotential method (Bai et al., 2017: 7). These two packages are popular in the field of MAX phase DFT calculations; however, there are other packages that are used in other fields. A fairly comprehensive list can be found at https://dft.sandia.gov/codes_list.html.

2.5. Boltzmann Transport Coefficients

It is possible to determine electrical conductivity from the band structure of a material, especially the band structure calculated from DFT. According to Boltzmann theory, when interpolating and integrating over the band structure, different Boltzmann transport coefficients

can be calculated over a range of temperatures and chemical potentials (Madsen & Singh, 2006; Madsen et al., 2018). One of the determined coefficients is the relationship between electrical conductivity, thermal conductivity and the Seebeck coefficient. The relationship is defined by a figure of merit (zT). The relationship is given by:

$$zT = \frac{S^2\sigma}{\kappa}T \tag{2.22}$$

where S is the Seebeck coefficient in $\mathrm{V\,K^{-1}}$, otherwise known as the thermopower, σ is the electrical conductivity in $\Omega^{-1}\,\mathrm{m}^{-1}$, κ is the thermal conductivity in $\mathrm{W\,m^{-1}\,K^{-1}}$, and T is the temperature in K. The term $S^2\sigma$ is often termed the power factor, since this parameter is important for thermoelectric materials. The thermal conductivity is usually made up of electronic and lattice contributions, κ_e and κ_l. It is complex trying to solve the Boltzmann transport equation for the electrical conductivity instead of the conductivity divided by the relaxation time of the system, σ/τ. The relaxation time depends on the energy and the temperature of the system and theoretically cannot be assumed to be a constant. The predominant approach taken in the literature when dealing with the electronic structure is to assume that the scattering rate is weak when compared to the energy dependency (Ong et al., 2011). This approach is valid for some semi-conductors and metals (Zhang & Singh, 2009).

A program developed to utilise Boltzmann theory from the band structure of a system was written to determine these properties. The programme, called `BoltzTraP`, short for Boltzmann Transport Properties, allows the calculation of the Seebeck coefficient and electronic thermal conductivity (Madsen & Singh, 2006). The Boltzmann Transport Equation (Boltzmann, 1964) is given by:

$$\frac{\delta f\left(\mathbf{r},\mathbf{p},t\right)}{\delta t} + \frac{\mathbf{P}}{m}\cdot\bigtriangledown_{\mathbf{r}} f\left(\mathbf{r},\mathbf{p},t\right) - \bigtriangledown_{\mathbf{r}} V_{ext}\left(\mathbf{r},t\right)\cdot\bigtriangledown_{\mathbf{p}} f\left(\mathbf{r},\mathbf{p},t\right) = \mathbf{I}\left[f\right] \tag{2.23}$$

where $\mathbf{I}\left[f\right]$ is the collision integral (Gressman & Strain, 2010; Krems, 2007).

`BoltzTraP` program was written in the Fortran programming language. The authors decided to rewrite the program using Python to make it more accessible, as well as providing additional capabilities to the program, calling it `BoltzTraP2` (Madsen et al., 2018). `BoltzTraP2` utilises the constant relaxation time approximation for calculations, therefore it is straightforward to convert σ/τ back into σ.

2.6. Density Functional Theory of MAX Phase Properties

DFT has been used to model various properties of MAX phases. Bai et al. (2017) presented a review of DFT on MAX phases. The main categories of properties that have been modelled by DFT are: the electronic structure and chemical bonding, point defects within the

MAX phase structure, lattice dynamics and related thermodynamic properties, phase stability and the prediction of potential new MAX phases, the compressibility of MAX phases, and the elastic properties of MAX phases (Bai et al., 2017). They conclude that the results are accurate, particularly for the lattice parameters, the compressibility and the elastic properties of the MAX phases. There is also good agreement between different authors around the electronic bonding structure, with a general trend showing a strong M-X bond and a weaker M-A bond (Magnuson & Mattesini, 2017).

2.6.1. MAX Phase Bonding

The first DFT paper that was published on MAX phases after the synthesis of Ti_3SiC_2 by Barsoum & El-Raghy (1996) investigated the electronic band structure, band width, total and local densities of state, and charge distributions of Ti_3SiC_2 using the full-potential linear-muffin-tin-orbital (FLMTO) method (Medvedeva et al., 1998). They compared the bonding characteristics of Ti_3SiC_2 to that of TiC, and investigated the effect of C lattice vacancies, and theoretical C substitutions with N and O. They determined that the Ti atoms in different layers have different bonding characteristics, which was determined from the partial densities of state. The Ti atoms adjacent to the Si layer (M_{II} on Figure 2.4b), termed Ti2, were calculated to have a higher density of state (DOS) at the Fermi level than the Ti atoms in the centre of the Ti_2C layer, termed Ti1 (M_I on Figure 2.4b). The authors cite the contribution of the Ti2 DOS at the Fermi level to the overall DOS at the Fermi level as the reason for the metallic properties that are present in Ti_3SiC_2.

On the difference between M_I and M_{II}, there is no consistency in the literature when it comes to the labelling of M atoms. Barsoum & El-Raghy (1996) used M1 for the atoms adjacent to the A group, while others like Wang & Zhou (2010) term this layer as M2. In this study, Ti1 atoms are in the centre of the Ti-C slab, and Ti2 atoms are in the layer next to the A group atoms. The terms from the references have been adjusted to match this definition.

Sun & Zhou (1999) also studied Ti_3SiC_2; however they utilised the linear combination of atomic orbitals (LCAO) approach. They also determined that Ti_3SiC_2 would have a metallic electronic conductivity; however, they do not attribute this to the M, A, or X element. Their densities of state calculations showed that the Ti2 atoms bond more strongly to the Si atoms and the Ti1 atoms bond more strongly to the C atoms when compared to the $Ti-Ti$ bonding or the $Si-C$ bonding. They postulate that the strength of the M-X bond is what gives this MAX phase its high melting point temperature (3200 °C).

Wang & Zhou (2003a) studied Ti_3SiC_2 under different pressures and showed that the bond length changes under pressure. They showed that the Ti2-Si bond length changes more than the other bond lengths, therefore showing that the Ti_3C_2 lattice moves closer to the Si layer instead of compressing the Ti-C bonds.

Further authors have investigated the bonding characteristics of MAX phases in general. It is reported that there is strong covalent bonding between the M and X components which

is analogous to the ceramic MX compounds, e.g. TiC (Barsoum & Radovic, 2011: 199; Bai et al., 2010: 8). This is attributed as the reason for the high mechanical strength observed in MAX phases. These results confirm what was observed by both Medvedeva et al. (1998) and Sun & Zhou (1999).

2.6.2. Calculation Methods

Ti_3AlC_2 shares the same structure as Ti_3SiC_2, although Ti_3AlC_2 has fewer electrons in the valence shell than Ti_3SiC_2. Nevertheless, the results of DFT calculations on Ti_3AlC_2 indicate that it is electrically conductive (Zhou et al., 2001). Despite different program packages used and different plane wave cut-off energies used, the lattice parameters calculated by Zhou et al. (2001) and Lane et al. (2012) are in good agreement with each other, as shown in Table 2.4. Their lattice parameters are in good agreement with experimental values as well. While there has not been a consensus on which program or plane wave cut-off energy yields the most accurate result, each paper seems to be in good agreement with the experimental values.

TABLE 2.4: Comparison of lattice parameters and calculation methods for select studies that used the GGA functional

MAX Phase	*a* (Å)	*c* (Å)	Method	Functional	Cut-off energy (eV)	Source
Ti_3SiC_2	3.068	17.67	Experimental	-	-	Jeitschko et al. (1964)
	3.0592	17.636	CASTEP	PW91	450	Bai et al. (2010)
	3.078	17.701	VASP	Not given	500	Sun et al. (2006)
Ti_3AlC_2	3.075	18.58	Experimental	-	-	Pietzka & Schuster (1994)
	3.0720	18.732	CASTEP	PW91	670	Zhou et al. (2001)
	3.083	18.66	VASP	PBE	400	Lane et al. (2012)
Ti_2AlC	3.052	13.64	Experimental	-	-	Schuster et al. (1980)
	3.053	13.64	CASTEP	PW91	450	Wang & Zhou (2004)
	3.067	13.75	VASP	PBE	400	Lane et al. (2012)

2.6.3. Density of States

Hug (2006) investigated the Ti 211 MAX phases and reported on the trends in their electronic structure. The author was able to report on the stability of some MAX phases that have not been produced experimentally. The DOS for each compound was reported and related to the valence shell of the A element (Figure 2.6). As the number of electrons in the valence shell increases, Hug (2006) states that the metallicity of the MAX phase increases, probably indicating that the electrical conductivity should increase with the filling of the valence shell. Although three of the compounds are not experimentally stable (Ti_2SiC, Ti_2PC, and Ti_2AsC), they show higher DOS at the Fermi level than Ti_2AlC. Hug (2006) postulate that the sharp drop to the DOS of Ti_2SC from Ti_2PC is because the S 3p states are at lower energy than the C 2p states, causing a stronger bond to form between Ti 3d and S 2p orbitals. Magnuson & Mattesini (2017) report that Ti_3SiC_2 should have a lower electrically resistivity

than Ti_3AlC_2, which shows that the trend in the DOS at the Fermi level from the 211 MAX phases could also relevant to the 312 MAX phases.

Wang & Zhou (2004) also investigated different 211 MAX phases of M_2AlC, where M = Ti, V, Cr, and Nb. For Ti_2AlC, they observe that the Ti 3d orbital is also responsible for the DOS at the Fermi level. Looking at the change in M atom, they observe that the increase in valence electrons across a period increases the DOS at the Fermi level. However, Nb_2AlC has roughly the same DOS at the Fermi level as Ti_2AlC, showing a lower DOS than V_2AlC, which is in the same group.

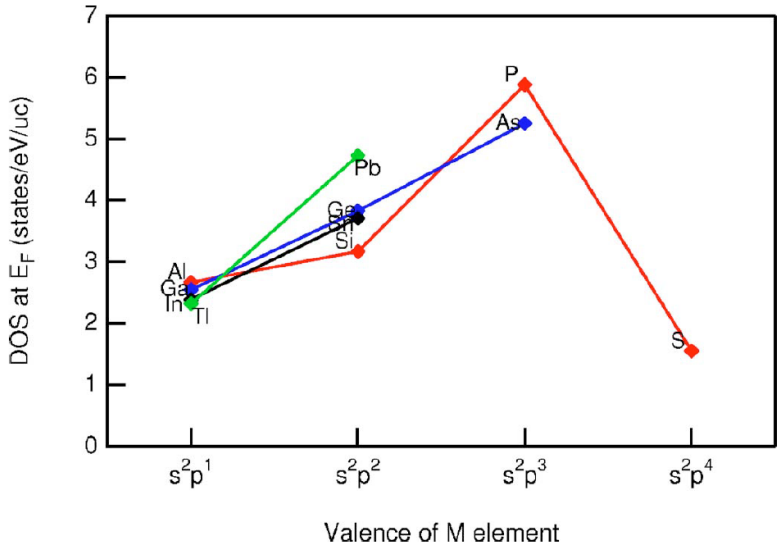

FIGURE 2.6: Values of the total DOS at the Fermi level as a function of the p-shell filling. Colours correspond to different shells: red, 3p; blue, 4p; black, 5p; and green, 6p. From Hug (2006)

Ivanovsky et al. (1995) in their paper on Ti_3SiC_2 report on the bonding characteristics as obtained from the local DOS. They remark that the primary contributor to the DOS at the Fermi level is the 3d states of the Ti2 atoms. They observe that the different environments of the Ti1 and Ti2 atoms gives rise to a difference in electronic structure, where the contribution to the DOS at the Fermi level by the Ti2 atoms is 3.76 times that of the Ti1 atoms. In contrast to TiC, which is not electrically conductive, the inclusion of the Si atoms changes the bonding characteristics of the Ti2 atoms, enabling the metallic behaviour of Ti_3SiC_2. This was also described by Medvedeva et al. (1998), who compared Ti_3SiC_2 against TiC, as well as investigating Ti_3SiC_2 with a C vacancy - Ti_3SiC. Sun & Zhou (1999) add to this interpretation, noting that strong bonds exist between Ti2 3d and Si 3p as well as between Ti1 3d and C 2p. They note that the bonding of Ti1 with C is stronger than that of Ti2 with C. The authors suggest that these strong bonds are the reason that Ti_3SiC_2 has a high melting temperature of 3200 °C.

Similar bonding characteristics to Ti_3SiC_2 were observed by Zhou et al. (2001) for Ti_3AlC_2. They note the hybridisation of the Ti2 3d and Al 3p orbitals along with that of Ti1 3d and

Ti2 3d with C 2p. The authors also observe that the primary contributor to the DOS at the Fermi level is the 3d orbital of Ti, both Ti1 and Ti2.

2.6.4. Oxidation Resistance

It appears as if the oxidation of MAX phases has not been modelled using DFT before, although the oxidation of MAX phases in air (Tallman et al., 2013) and in acids (Jovic et al., 2006) have been done experimentally. The oxidation tests in air have been conducted at temperatures above 800 °C, therefore would not strictly be relevant for comparison with oxidation in a fuel cell. However, the conclusions of Tallman et al. (2013) do provide interesting postulations that can be compared to a DFT study, such as the fact that Ti_2AlC has a higher oxidation resistance than Ti_3AlC_2 in air because it has a higher Al ratio. The higher Al ratio allows a protective Al_2O_3 layer to form more easily over the surface of the Al MAX phases, passivating the effect of the corrosion by slowing down the kinetics of the Al migration. This Al_2O_3 layer has been seen experimentally but has not been modelled using DFT due to its complexity. Since, the electron flow goes from the Pt catalyst particle to the support material, it may be possible for electrical conductivity to be maintained despite an Al_2O_3 layer, provided the Al_2O_3 layer does not interfere with the Pt nanoparticle surface.

There are no known DFT papers on MAX phases that investigate the MAX phases in the presence of a highly corrosive environment with a pH of between 0 and 1, which are the conditions found in a PEMFC. DFT as a tool is not able to include pH as a factor in calculations designed to determine kinetic oxidation resistance, but it can be used to study the thermodynamics of oxidation. The results obtained from DFT could be used in other calculations, for example in determining a Pourbaix diagram.

2.6.5. Vacancy Formation

The vacancy formation energy has often been studied with the aim of determining a material's suitability for use in high irradiation environments. The consensus in the literature is that the formation energy of an A group element is lower than that of an M or X element (Bai et al., 2017: 18). While point defects have been studied predominantly, the migration energy of elements has also been studied. Experimentally, the formation of Al_2O_3 on the surface of Ti_3AlC_2 when heated in air was observed Wang & Zhou (2002b, 2003b). The Al_2O_3 forms before TiO_2, indicating that Al more readily diffuses out of the Ti_3AlC_2 lattice to oxidise in air. Barsoum et al. (1997) and Sun et al. (2001) investigated Ti_3SiC_2 at high temperatures in air and found that both SiO_2 and TiO_2 form. Both found that the oxide layer that formed consisted of an outer layer of TiO_2 and an inner layer of SiO_2.

It is known that MAX phases form with vacancies present in their structure, and vacancies of Ti, Al, and C have been investigated in Ti_2AlC using DFT (Liao et al., 2008a). It was determined that structures with Al or C vacancies can exist within the Ti_2AlC structure while only altering the formation energy slightly, and without causing the formation of

other secondary phases like TiC, TiAl, or Al_4O_3 to become more favourable. However, the formation energy of Ti_2AlC with Ti vacancies is much larger, therefore Ti vacancies are unlikely to form in Ti_2AlC.

To understand this formation, DFT studies looked at vacancy formation energies and the migration energy of vacancies. Medvedeva et al. (1998) was one of the first DFT papers to be published about Ti_3SiC_2, in which they looked at C vacancies. Different papers have been published investigating vacancies in Ti_2AlC showing that the vacancy formation energy of Al is lower than for Ti or C (Liao et al., 2008a,b; Tan et al., 2014; Wang et al., 2008a). Similarly, Ti_3AlC_2 and Ti_3SiC_2 have been studied, again showing that the A group element would preferentially form a vacancy before the M or X group atoms (Middleburgh et al., 2013; Wang et al., 2017; Wang et al., 2015; Zhang et al., 2013; Zhao et al., 2014).

While there does not seem to be a consensus on any values for vacancy formation energy in the literature, the trend of the A group element having the smallest vacancy formation energy is consistent.

2.6.6. MAX Phase Surfaces

Whenever bulk DFT calculations are possible for a material, surfaces can be cut and their properties investigated. This is usually to report the surface energy of the different surfaces of a material. This is widely used to study catalytic reactions, since reactions occur on the surface of a catalyst. Gas phase molecules can be adsorbed to a surface which provides insight into adsorption mechanisms, surface coverages, and potential reaction paths, to name but a few (Greeley et al., 2002).

The earliest surface paper for MAX phases that was published was by Sun & Ahuja (2006) on Cr_2AlC (0 0 0 1) surfaces and found that the Al termination was the most stable. Music et al. (2006, 2007) then investigated other 211 MAX phases, including Ti_2AlC, and confirmed that the A group remains the most stable surface termination. However, Music et al. (2006, 2007) failed to distinguish between surfaces for which it is possible to have different elements in the subsurface layer. For Ti_2AlC they only report the surface energy with Ti on the surface, but do not mention whether Al or C is in the subsurface layer.

To calculate the surface energy of a system, one requires the chemical potential of the constituent elements or the energy of the bulk system. The surface energy can then be calculated using Equation 2.24.

$$\gamma = \frac{E_t - \sum n_i \mu_i}{2A} \tag{2.24}$$

Here, γ is the surface energy, E_t is the total energy, A is the slab surface area, n_i is the number of atoms, and μ_i is the chemical potential of the atomic species. Often $\sum n_i \mu_i$ is simply the bulk energy of the system multiplied by a stoichiometric factor. The factor 2 is required because a surface system has two surfaces in a periodic unit cell, one at the top

and the other at the bottom of the slab. This approach works well when the system consists of a single element, or when the chemical potentials are readily available. One condition of using this equation is that the surface on the top and bottom of the slab needs to be the same, since both surfaces have an effect on the energy of the system.

Music et al. (2006, 2007) do not report what they used for their reference energies, therefore there is no way to prove that their results are accurate.

Zhang & Wang (2007) studied the (0 0 0 1) surfaces of Ti_3AlC_2 and Ti_3SiC_2 using 1 x 1 unit cells. They correctly differentiate between the six different surfaces possible and calculated the surface energies of each surface. The surface energy calculation requires a symmetrical slab, with the top and bottom surface being identical. Because of the layered structure of the MAX phases, creating a symmetrical slab requires the system to be non-stoichiometric. Therefore, the bulk energy cannot be used in the calculation of the surface energy, and the chemical potential of the pure element is used instead. To assume that the chemical potential of the elemental system will be the same as in the surface system is a big assumption, especially in the case of MAX phases where the layered structure changes the surrounding environment of each element completely.

Kim et al. (2015b) investigated $LiMn_2O_4$ spinels, which have a similar problem when it comes to calculating the surface energy as MAX phases, creating either symmetrical non-stoichiometric surface slabs or asymmetrical stoichiometric slabs. Their approach to solve the problem involves calculating the system energies of stoichiometrically different systems and solving for the chemical potentials of each element. This has the benefit of calculating the chemical potential of each element for the spinel in an environment that is similar to where the chemical potential is going to be used. Zhang & Wang (2007) identify this problem, but just substitute the chemical potential of the element with the difference between the chemical potential of the pure element and the chemical potential in the surface environment, then using $\Delta\mu_i$ in their equations. They then plot the surface energy as a function of $\Delta\mu_i$, where i is one of the elements, with the chemical potential of the other elements kept constant at the value of their pure elemental chemical potential. The resulting figures for $\Delta\mu_{Ti}$ and $\Delta\mu_{Si}$ are shown in Figure 2.7. The same approach is used for Ti_3AlC_2.

Zhang & Wang (2007) also calculate the cleavage energy of each surface using an approach that maintains the stoichiometry of the systems. This calculates the energy required to cleave the bonds between two layers of atoms, which can then tell one which bonds are easiest to break. Keeping the stoichiometry of the systems the same as the bulk system allows the energy of the bulk unit cell to be used as the reference energy, which should provide a more accurate description of the system. From the results of the cleavage energy, Zhang & Wang (2007) conclude that the Ti2-Al/Si bond is the weakest and the Ti2-C bond is the strongest. They also conclude that the Ti2-Si bond of Ti_3SiC_2 is stronger than the Ti2-Al bond of Ti_3AlC_2, which explains why Ti_3SiC_2 has a higher bulk modulus than Ti_3AlC_2.

Wang et al. (2008a) also recognise the pitfalls in using symmetric slabs in their study of Ti_2AlC (0 0 0 1) surfaces. They correctly identify the four different surface terminations

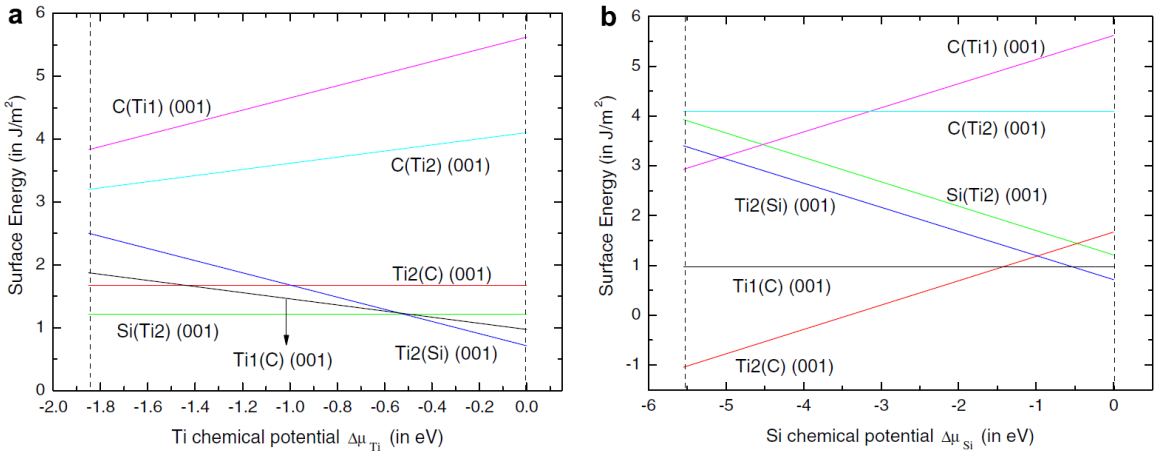

FIGURE 2.7: Surface energy (J m^{-2}) of Ti_3SiC_2 as a function of chemical potential of (a) $\Delta\mu_{Ti}$ with $\Delta\mu_{Si} = 0$, and (b) $\Delta\mu_{Si}$ with $\Delta\mu_{Ti} = 0$ (Zhang & Wang, 2007).

possible. Their approach to calculate the surface energy differs from that used by Kim et al. (2015b). They calculate the unrelaxed cleavage energy for the complementary pair of surfaces using stoichiometric slabs. Then they allow surface reconstruction to occur and calculate the relaxation energy – the difference between the relaxed and unrelaxed systems. The cleavage energy is then corrected with this relaxation energy to yield the surface energy of the system. They conclude that the Al(Ti) and Ti(C) surfaces are more stable than the C(Ti) and Ti(Al) surfaces, with the Al(Ti) and Ti(C) surfaces being more stable under different chemical conditions using the difference in chemical potentials to the elemental system.

Orellana & Gutiérrez (2011) investigated the (0 0 0 1) surfaces of Ti_3SiC_2 using DFT and molecular dynamics. They concluded that the most stable surfaces were Si(Ti2) and Ti2(Si) at low temperatures because of their low surface energy. However at high temperatures, using molecular dynamics simulations, these surfaces were not stable. Instead, the most stable surfaces at high temperatures were Ti1(C) and Ti2(C). They remark that the surfaces with C on top, i.e. C(Ti1) and C(Ti2), had the highest surface energy and were the least stable compared to M or X atoms.

2.7. Project Objectives, Hypotheses and Key Questions

2.7.1. Project Objectives

Based on the above literature, the objectives of the project are:

1. To successfully use DFT to characterise Ti_3SiC_2, Ti_3AlC_2, and Ti_2AlC MAX phase properties — electrical conductivity and oxidation resistance;
2. To determine which MAX phase would give the best combination of properties for use as an electrocatalyst support material; and

3. To develop methodology to characterise and investigate other MAX phases, including salt solutions, in the context of PEMFC electrocatalyst support materials.

2.7.2. Hypotheses

Based on the above objectives, it is hypothesised that:

1. It is possible to model MAX phases using DFT, since it has been done before in literature. Furthermore, it will be possible to gain insight into the electrical conductivity and oxidation resistance of the different MAX phases;
2. Ti_3SiC_2 is more electrically conductive than Ti_3AlC_2 and Ti_2AlC, therefore Ti_3SiC_2 will be the most suitable electrocatalyst support material for PEMFCs; and
3. The 312s are more stable than the Ti_2AlC MAX phase, therefore a salt solution that increases the electrical conductivity of a 312 MAX phase would be more suitable as an electrocatalyst support material.

2.7.3. Key Questions

To aid in testing the hypotheses, the following key questions will guide the research:

1. Will validation on known literature examples show that it is possible to get electrical conductivity and oxidation resistance from the DFT models?
2. Which MAX phase would give the best combination of properties for use as an electrocatalyst support material?

3. Methodology and Model Validation

The initial structures of the MAX phase unit cells were built in Materials Studio using the internal coordinates and lattice parameters from Wang & Zhou (2010) for Ti_2AlC and Ti_3AlC_2. For Ti_3SiC_2 the same internal coordinates as Ti_3AlC_2 were used with the lattice parameters from Barsoum (2000). The lattice parameters from Barsoum (2000) for Ti_2AlC and Ti_3AlC_2 are the same as in Wang & Zhou (2010). The unit cells generated by Materials Studio are shown in Figure 3.1 and the lattice parameters and internal coordinates used are shown in Table 3.1.

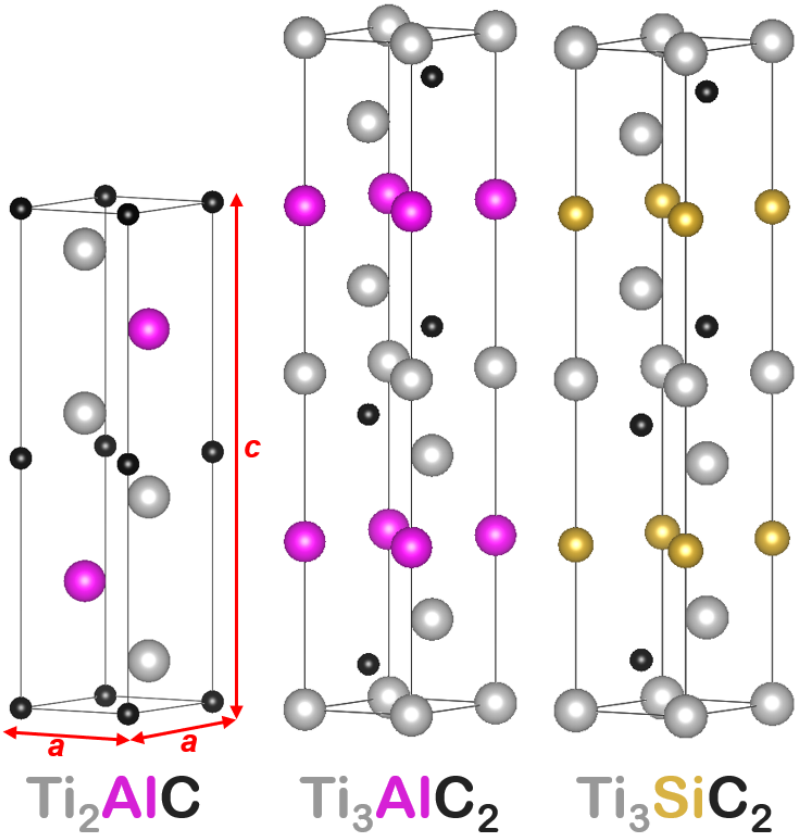

FIGURE 3.1: Unit cells generated in Materials Studio, visualised with VESTA

One of the most important requirements for DFT modelling is determining which exchange correlation functional best represents the system. Four different functionals were compared, from which a single functional would be used for further calculations. The different functionals used were:

- Local density approximation (LDA) (Perdew & Zunger, 1981),

TABLE 3.1: Initial MAX phase lattice parameters and internal coordinates

MAX Phase		**Ti_2AlC**	**Ti_3AlC_2**	**Ti_3SiC_2**
a (Å)		3.040	3.075	3.0665
c (Å)		13.60	18.58	17.671
Volume $\left(Å^3\right)$		108.847	152.148	143.906
Internal Coordinates	Ti(1)	($1/3$, $2/3$, 0.086)	(0, 0, 0)	(0, 0, 0)
	Ti(2)		($1/3$, $2/3$, 0.128)	($1/3$, $2/3$, 0.128)
	Al / Si	($1/3$, $2/3$, 0.75)	(0, 0, 0.25)	(0, 0, 0.25)
	C	(0, 0, 0)	($1/3$, $2/3$, 0.564)	($1/3$, $2/3$, 0.564)

In the 312 MAX phases, Ti(1) is the inner layer of M atoms, while Ti(2) is adjacent to the A layer (see Figure 3.8 and Figure 2.4). (Barsoum, 2000; Wang & Zhou, 2010)

- Generalised gradient approximation (GGA) (Perdew et al., 1992, 1996a), with Perdew-Wang 1991 (PW91) (Perdew & Wang, 1992),
- Perdew-Burke-Ernzerhof (PBE) (Perdew et al., 1996b), and
- Revised Perdew-Burke-Ernzerhof (RPBE) (Hammer et al., 1999).

The Chemical Engineering Department at the University of Cape Town (UCT) has a license for Vienna *Ab-initio* Simulation Package (VASP) (Kresse & Furthmüller, 1996) with which to run DFT calculations. Computations were performed using facilities provided by the UCT ICTS High Performance Computing team (`http://www.hpc.uct.ac.za`) and on the lengau cluster at the Centre for High Performance Computing (CHPC) (`https://www.chpc.ac.za`).

There are two important modelling parameters that need to be optimised for a material when performing a DFT study. These are the k-point grid and cut-off energy. The values for these parameters need to be determined such that the smallest k-point grid and lowest cut-off energy can be used while still maintaining a high degree of accuracy. A smaller k-point grid and low cut-off energy results in a short calculation time but can be inaccurate, while a large k-point grid and high cut-off energy provide greater accuracy but are computationally expensive. Therefore, the values that provide sufficient accuracy with the lowest computational time need to be found.

For all bulk calculations, the tetrahedron method with Blöchl corrections was used (Blöchl, 1994), while for surface calculations a 2nd order Methfessel-Paxton smearing scheme was used (Methfessel & Paxton, 1989). The electronic convergence criteria used was 1×10^{-4} eV. The finite difference using the second derivative method was used for the movement of atoms and the force criteria on each atom was required to be <0.03 eV/Å. The stress tensor and the forces on atoms were calculated, the relaxation of ions was allowed, and for automatic optimisation of the unit cell volume, the cell size and shape were permitted to change. The initial magnetic moments for each element were taken from Cohen et al. (2007). The initial magnetic moment was 0 for Ti, Si, and C, and 5 μ_B for Al.

3.1. k-point Grid Optimisation

The k-points of a unit cell in a DFT calculation are the points in reciprocal space at which the energy is calculated. The k-points form a 3D grid within the reciprocal unit cell, which then allows for summation of plane waves over discrete points instead of integrating over the whole space. Often some k-points are symmetrical, so an irreducible number of k-points is determined, which are weighted according to their symmetry (Eichler, 2003). Only the k-points that fall within the Brillouin zone are used in the calculation, therefore it is necessary to ensure sufficient k-points are used to yield a high enough k-point density to ensure accurate energy calculations (Payne et al., 1992). This is achieved by optimising the k-point grid, and as such, the k-point density.

Since MAX phases are hexagonal not cubic, both the *a* and *c* k-point grid dimensions need to be varied. The *a* (and therefore *b*) dimension were varied from 3 to 13 for all three MAX phases. For Ti_2AlC, the *c* grid dimension was varied from 1 to 4, while for Ti_3AlC_2 and Ti_3SiC_2, the *c* grid dimension was varied from 1 to 7. Each k-point grid yields an integer number of irreducible k-points within the Brillouin zone. The result of a single point energy calculation can then be plotted against the irreducible number of k-points. The different k-point grids were run using a cut-off energy of 500 eV. This cut-off energy is higher than the recommended cut-off energy required for accuracy for each element (Kresse & Marsman, 2012), therefore can be considered accurate for the bulk MAX phases. A gamma-centred k-point grid using the Monkhorst-Pack scheme was used for all calculations (Chadi & Cohen, 1973; Pack & Monkhorst, 1977). The gamma-centred grid is recommended in the VASP manual for use with hexagonal systems, as "the energy converges significantly faster with *Gamma* centred grids" (Kresse & Marsman, 2012: s. 5.5.4).

The k-point grid was chosen by calculating the difference between the energy from a k-point grid and the next largest k-point grid, which was termed the "difference to next". The absolute energy difference was plotted against the number of irreducible k-points and the k-point grid with the smallest number of irreducible k-points with an energy difference of less than 1 meV/atom was chosen. Smaller k-point grids generally have lower computational costs but can be inaccurate, while large k-point grids are more accurate but are computationally more expensive. Therefore, the smallest k-point grid that was sufficiently accurate (absolute energy difference to next <1 meV/atom) was used for further calculations. The energy differences are shown in Figure 3.2, for Ti_2AlC, Ti_3AlC_2, and Ti_3SiC_2.

Shown in Figure 3.2 are only those energy differences that were less than 40 meV/atom. There were multiple k-point grids that yielded energy differences in the order of tens or hundreds of meV/atom (see Appendix A). The optimum k-point grids, along with the k-point density, are shown in Table 3.2, where the k-point grid, irreducible number of k-points and system energy are shown. The k-point density for the *a* and *c* dimensions using the optimised lattice parameters are also shown in Table 3.2. Most functionals required less

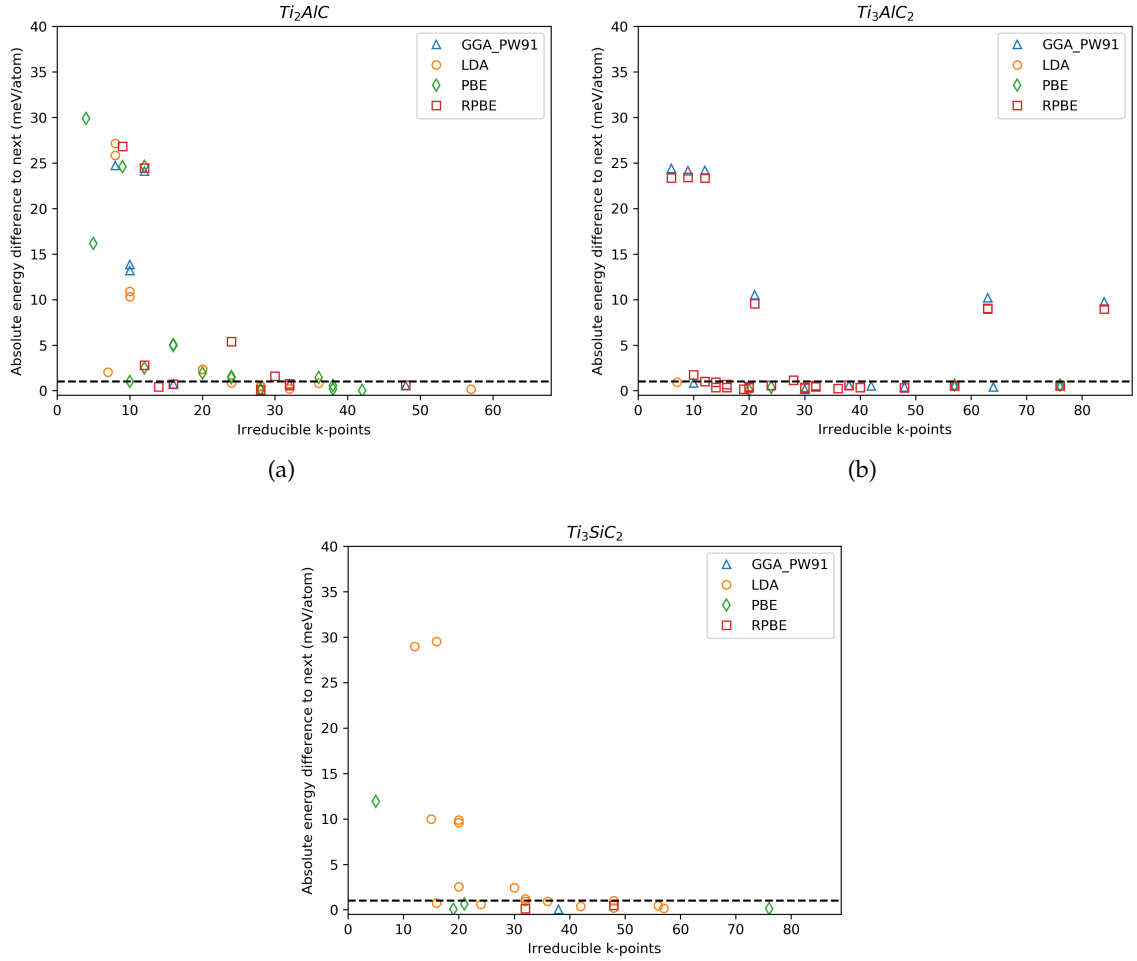

FIGURE 3.2: Energy difference at different irreducible k-points for (a) Ti_2AlC, (b) Ti_3AlC_2, and (c) Ti_3SiC_2. The black dashed line represents the convergence criteria of 1 meV/atom.

than 10 irreducible k-points to achieve an accuracy of within 1 meV/atom to a large k-point grid.

3.2. Cut-off Energy Basis Set Optimisation

The cut-off energy determines the number of planewaves that are included in the basis set. A high cut-off energy includes more plane waves, which is more accurate, but is computationally more expensive (Mattsson et al., 2005; Payne et al., 1992). Therefore, the cut-off energy that provides good accuracy while minimising computational cost is required.

Once the optimum k-point grid was determined for each functional and each MAX phase, the optimum cut-off energy basis set was determined. The single point energies of the systems were calculated with cut-off energies between 250 eV and 1000 eV. Once an approximate cut-off energy was obtained, the final cut-off energy was determined using 10 eV

intervals. Each of these were compared against the cut-off energy at 1000 eV. The convergence criteria used was 1 meV/atom, which is <0.1 kJ/mol/atom. The results are shown in Figure 3.3 for Ti_2AlC, Ti_3AlC_2, and Ti_3SiC_2.

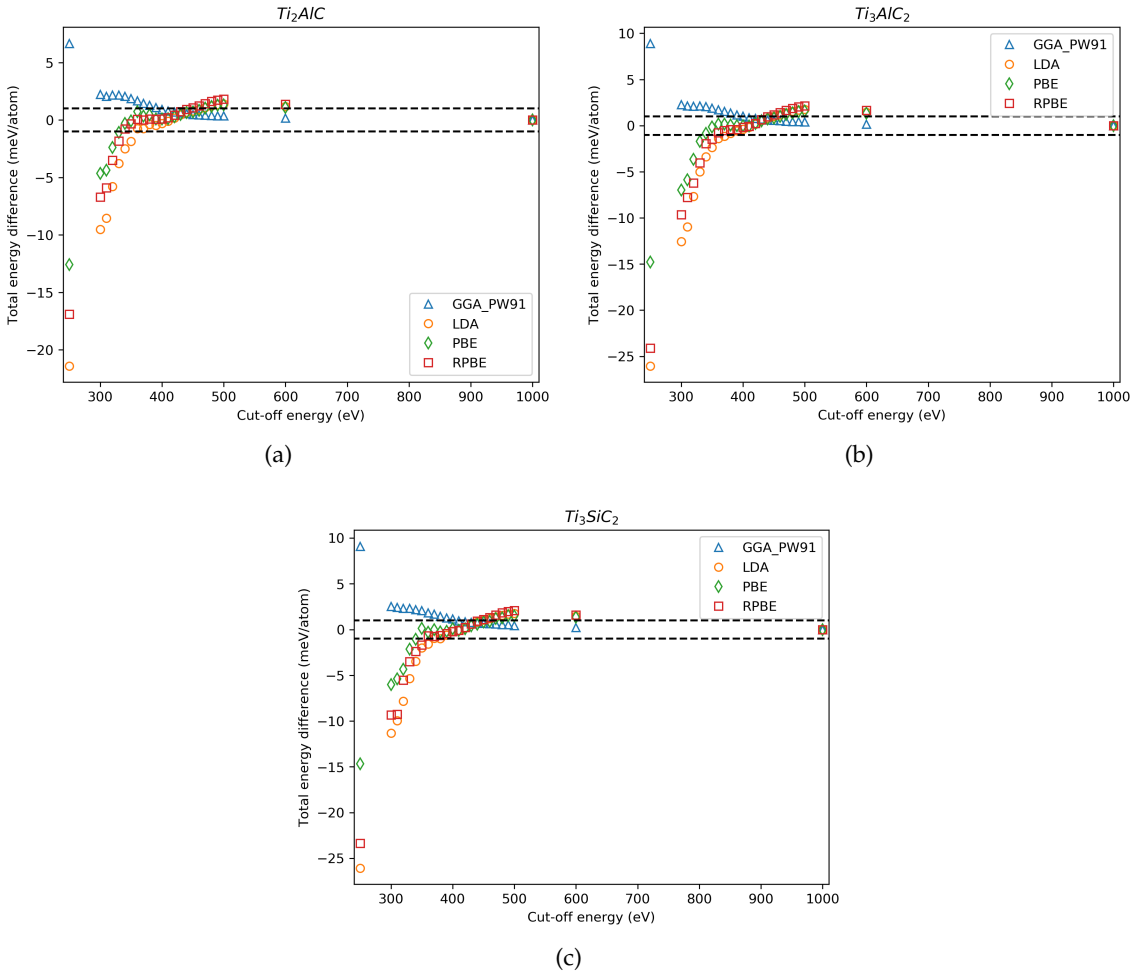

FIGURE 3.3: Energy difference compared to the energy at 1000 eV cut-off energy for (a) Ti_2AlC, (b) Ti_3AlC_2, and (c) Ti_3SiC_2. The black dashed lines indicate the convergence criteria of 1 meV/atom.

The optimised k-point grid, irreducible number of k-points, and lowest cut-off energies that were within the selection criteria are shown in Table 3.2. Each functional required a cut-off energy of between 340 eV and 410 eV.

3.3. Lattice Parameter Optimisation

Using the optimised k-point grid and cut-off energy, the unit cell volume was optimised. This determines the lattice parameters that yield the unit cell with the minimum system energy, calculated using single point energy calculations. Since MAX phases have hexagonal unit cells, where the *c* lattice parameter is longer than the *a* lattice parameter (see Figure 3.1), both lattice parameters need to be varied independently of each other. In order

TABLE 3.2: Optimised k-point grid, cut-off energy and system energy for different functionals

MAX Phase	Functional	k-point grid	Irreducible number of k-points	Cut-off energy (eV)	System energy (eV)	a k-point density ($Å^{-1}$)	c k-point density ($Å^{-1}$)
Ti_2AlC	GGA-PW91	7x7x1	8	400	-62.704018	0.0464	0.0727
	LDA	6x6x1	7	360	-68.92027	0.0552	0.0739
	PBE	6x6x1	7	340	-63.147733	0.0543	0.0727
	RPBE	7x7x2	16	340	-62.11857	0.0462	0.0362
Ti_3AlC_2	GGA-PW91	3x3x2	6	410	-100.58026	0.1077	0.0271
	LDA	7x7x1	8	380	-110.28648	0.0471	0.0546
	PBE	7x7x3	16	340	-100.96711	0.0465	0.0178
	RPBE	3x3x2	6	360	-99.392406	0.1074	0.0269
Ti_3SiC_2	GGA-PW91	3x3x2	6	410	-105.63352	0.1087	0.0279
	LDA	3x3x3	6	370	-116.01641	0.1105	0.0190
	PBE	3x3x7	12	350	-106.11378	0.1087	0.0080
	RPBE	4x4x2	8	360	-103.72298	0.0810	0.0281

to have comparable volumes, the a lattice parameter and cell volume was varied, with the c lattice parameter calculated using Equation 3.1. It was chosen to vary the volume with the a lattice parameter so that when the bulk modulus was fitted, the volumes would be at regular intervals and therefore more easily comparable.

$$V_{hexagonal\ unit\ cell} = a^2 c \sin(60°) \tag{3.1}$$

The a lattice parameter was varied by 0.01 Å from 0.07 Å smaller than the literature values (Table 3.1) to 0.05 Å larger. The unit cell volume was varied in steps of 1.73 $Å^3$ (2.0 $Å^3$ $\times$ $\sin(60°)$), spanning approximately 10 $Å^3$ larger and smaller than the literature volume (Table 3.1). The single point energy was then calculated at each combination of a lattice parameter and volume.

Additionally, VASP allows for the optimisation of the lattice parameters and volume automatically within its calculation procedure. It does this through the calculation of the stress tensor and forces on the atoms of the unit cell and then allowing the cell volume and cell shape to be adjusted. However, performing manual relaxation is recommended (Kresse & Marsman, 2012). The automatic relaxation lattice parameters were calculated and were compared to the manual optimisation.

For each MAX phase-functional combination, the lowest system energy over all a lattice parameter and volume combinations was found to determine the corresponding a lattice parameter. All the a and corresponding c lattice parameters for each MAX phase and functional combination are given in Table A.1. The range of volumes at that constant a lattice parameter were used to fit a cubic polynomial, from where the minimum of the curve was used to find the c lattice parameter. The normalised system energies are shown plotted against the unit cell volume in Figure 3.4. The automatic unit cell optimisation results are also shown, normalised to the lowest energy achieved through manual relaxation. Also shown is the volume from experimental results, which is shown to reference the calculated volumes.

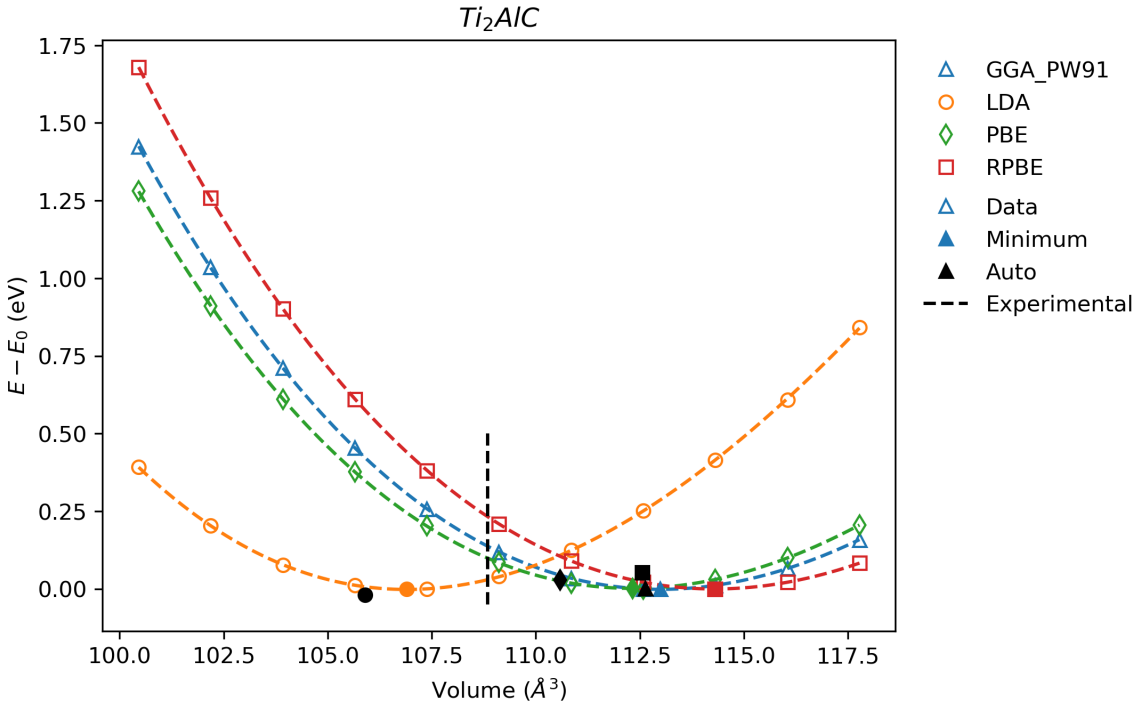

(a)

It is widely reported in the literature that the LDA functional tends to underestimate lattice parameters, while the GGA class of functionals tends to overestimate lattice parameters (Mattsson et al., 2005). This can be seen by the shift in the LDA curve from the other curves. For the LDA functional, it was found that the single point energy from the automatic relaxation was lower than any manual calculation for all three MAX phases. However, for the GGA-PW91, PBE, and RPBE functionals, the lowest energy from manual optimisation was always lower than the energy obtained through the automatic relaxation procedure. Each system with the fitted lattice parameters was rerun to confirm the energy of that system.

To compare the difference between the automatic unit cell volume optimisation and the manual optimisation with fitted parameters using different functionals, the differences between the calculated and experimental lattice parameters are shown in Figure 3.5 for the a and c lattice parameters.

It can be seen in Figure 3.5 that the LDA functional tends to underestimate the lattice parameters, which is consistent with literature observations. For most cases, the GGA-PW91 and RPBE functionals overestimate the lattice parameters, with the only anomaly occurring with the c lattice parameter for Ti_3AlC_2. The lattice parameter predictions by the PBE functional are all either overestimates or are the same as experimental results for the manually fitted results. However, the automatic relaxation results do not consistently over- or underestimate the lattice parameters.

This trend becomes more apparent when the predicted volumes are plotted against the experimental volume in the same way that the lattice parameters are compared. This is shown in Figure 3.6. It can be seen that the PBE functional is the most accurate in predicting the

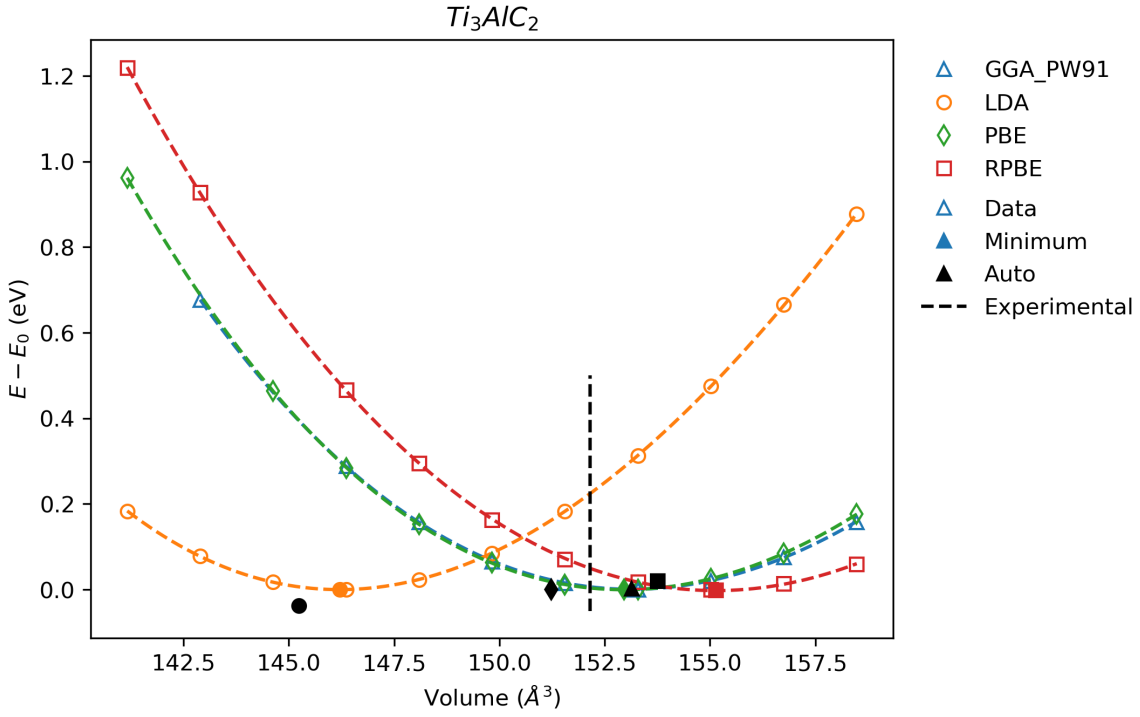

(b)

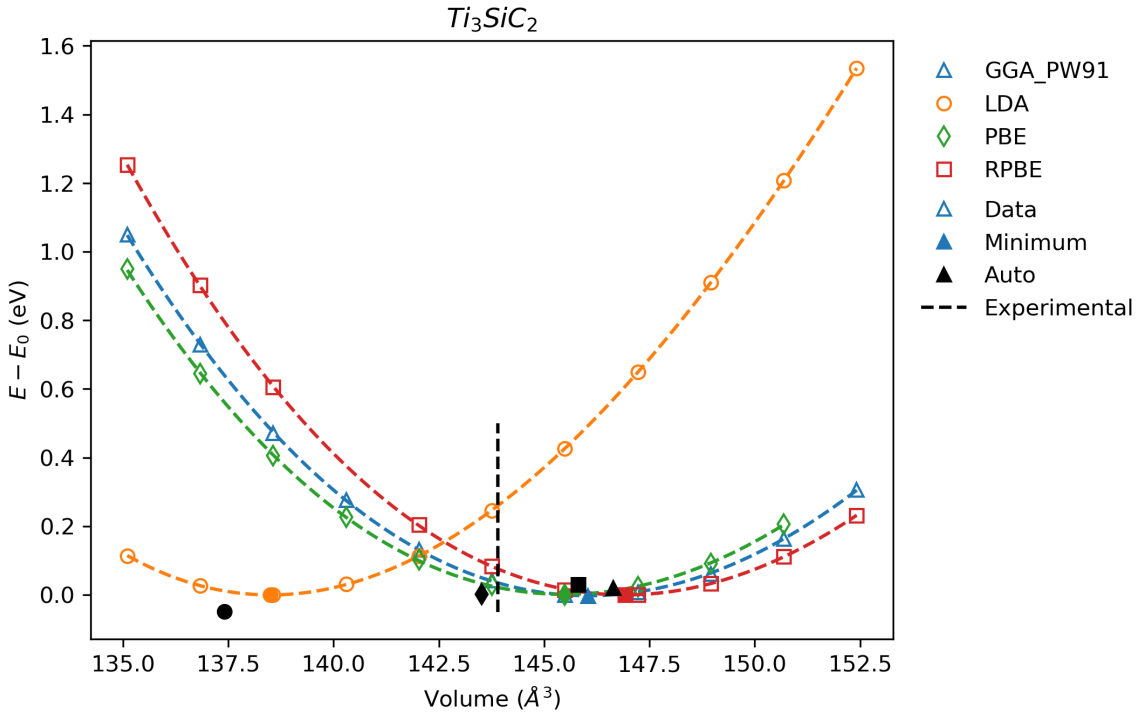

(c)

FIGURE 3.4: Normalised energies of minimum a lattice parameter over different unit cell volumes for each functional for (a) Ti_2AlC, (b) Ti_3AlC_2, and (c) Ti_3SiC_2. For each functional, the volume-energy data is shown as "Data", the miniumum energy point is shown as "Minimum", and the automatically fitted volume is shown as "Auto". Dashed lines are fitted using a cubic polynomial. Experimental volume from literature plotted as a reference.

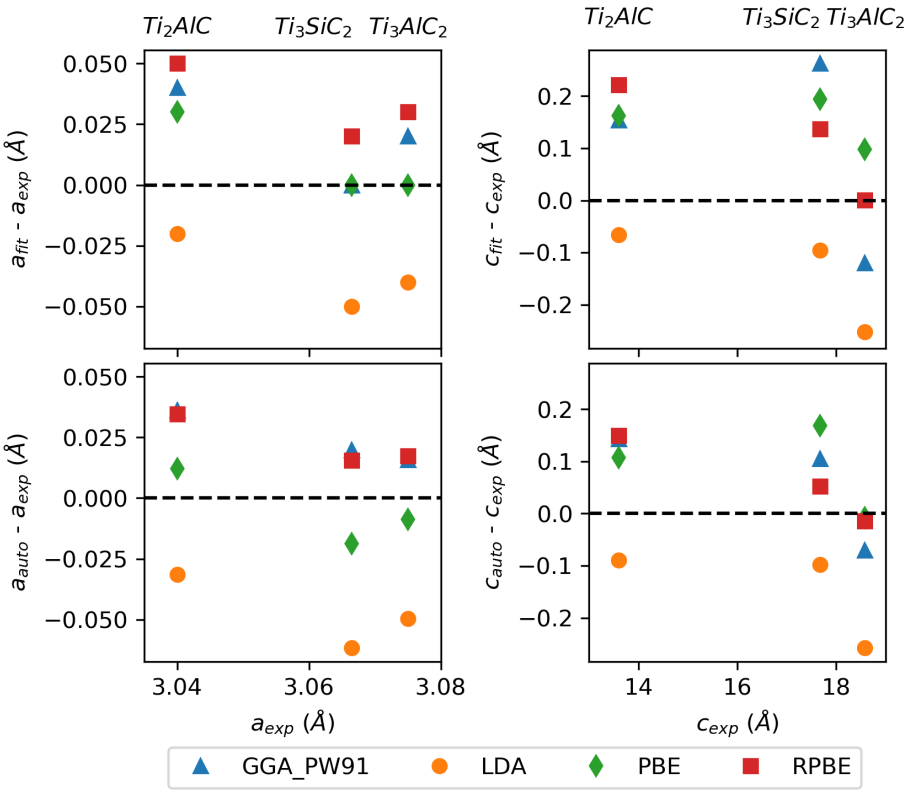

FIGURE 3.5: Differences between automatic and manually fitted a and c lattice parameters against experimental a and c lattice parameters ("fit" denotes manually fitted and "auto" denotes the automatic optimisation results). Labels for each MAX phase are shown at the top of the figure above the corresponding a and c experimental lattice parameters.

unit cell volume. It is interesting to see that although the manually fitted volumes all overestimate the volume, except the LDA functional, the same cannot be said for the automatic relaxation. When the volume of the unit cell was allowed to be optimised automatically, the PBE functional overestimates the volume of Ti_2AlC, and underestimates the volumes of Ti_3AlC_2 and Ti_3SiC_2.

To determine statistically which functional is best at predicting the unit cell volume, the root-mean-square error of the manually fitted and automatic volumes was calculated and is shown in Table 3.3.

3.4. Mechanical Properties

The predicted bulk modulus of the MAX phases from each functional were calculated based on the Birch-Murnaghan equation of state (BM-EOS) (Birch, 1947). A mathematical version of this equation is shown below.

$$E = E_0 + \frac{9V_0B_0}{16}\left\{\left[\left(\frac{V_0}{V}\right)^{\frac{2}{3}} - 1\right]^3 B_0' + \left[\left(\frac{V_0}{V}\right)^{\frac{2}{3}} - 1\right]^2\left[6 - 4\left(\frac{V_0}{V}\right)^{\frac{2}{3}}\right]\right\} \tag{3.2}$$

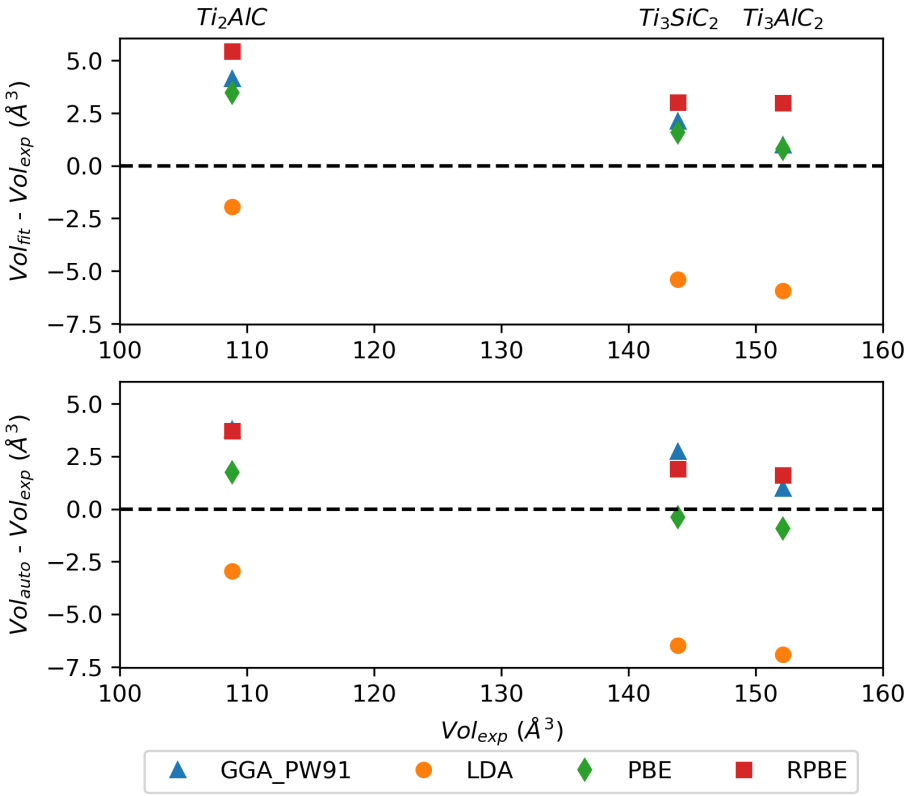

FIGURE 3.6: Differences between automatic and manually fitted unit cell volumes against experimental unit cell volume

In Equation 3.2, E is the internal energy in eV, E_0 is the equilibrium internal energy in eV, V_0 is the equilibrium unit cell volume in Å^3, B_0 is the equilibrium bulk modulus in eV/Å^3, and B_0' is the partial derivative of the bulk modulus with respect to the system pressure. The equation is fitted to unit cell volume vs energy data determined from the lattice parameter optimisation. However, to fit the Birch-Murnaghan EOS the c/a lattice parameter ratio of each system was calculated and compared to the experimental c/a ratio. Within each series where the a lattice parameter was kept constant, the system with the closest c/a ratio to the experimental ratio was chosen. By fitting the BM-EOS to cell volumes from a constant c/a lattice parameter ratio, the bulk modulus of the overall change in unit cell volume is determined. If the a lattice parameter was kept constant (like in determining the c lattice parameter earlier) then the bulk modulus in the c-direction would be determined, not the bulk modulus of the overall change in unit cell volume. The resulting series of volume–energy data was then fitted to the Birch-Murnaghan EOS and the bulk modulus for each MAX phase–functional pair was determined. The fitting was done using the open source code pymatgen (Ong et al., 2013). The individual graphs of each MAX phase-functional pair can be found in Appendix A (Figure A.2 for Ti_2AlC, Figure A.3 for Ti_3AlC_2, and Figure A.4 for Ti_3SiC_2). Figure 3.7 shows the comparison of the calculated bulk moduli to the experimental bulk moduli. The experimental bulk modulus of Ti_2AlC used was 144 GPa (Hettinger et al., 2005), and 165 GPa and 185 GPa for Ti_3AlC_2 and Ti_3SiC_2, respectively (Barsoum, 2000).

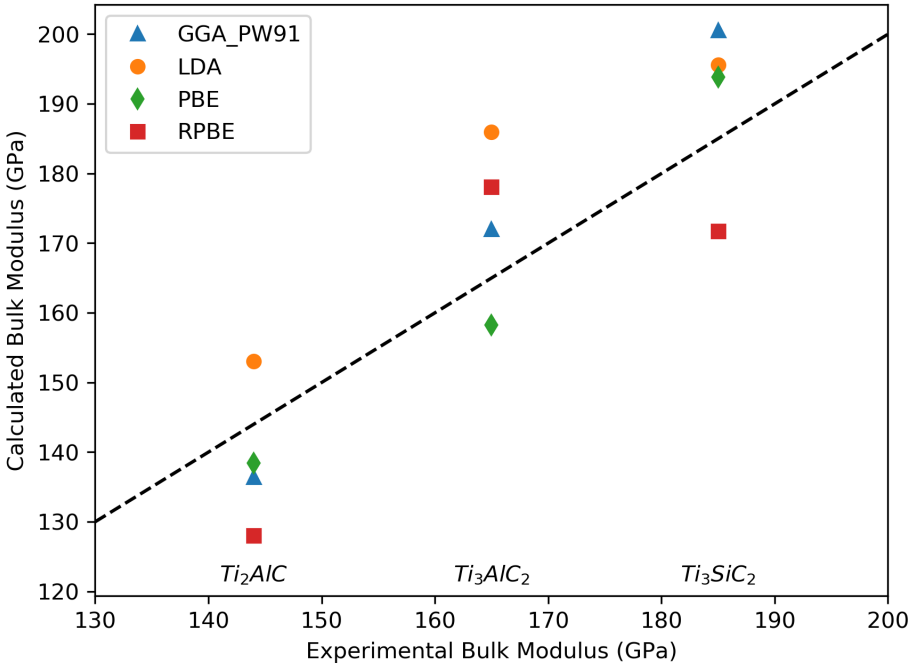

FIGURE 3.7: Comparison of calculated bulk moduli against experimental values. The black dashed line is where the experimental bulk modulus is equal to the calculated bulk modulus, i.e. the line $y = x$.

From Figure 3.7, it can be seen that the PBE functional has the closest bulk modulus to experimental value. For Ti_2AlC, the PBE bulk modulus is 3.9 % (5.6 GPa) less than literature, for Ti_3AlC_2 it is 4.1 % (6.7 GPa) less and for Ti_3SiC_2 it is 4.8 % (8.8 GPa) greater than the experimental value. The GGA-PW91 functional is the next closest functional for Ti_2AlC and Ti_3AlC_2, but struggles with Ti_3SiC_2. Both the LDA and RPBE functional have a much greater error than the PBE and GGA-PW91 functionals.

3.5. Choice of Functional

Since it is desirable to only use one functional for further calculations, the root-mean-square error (RMSE) can be calculated using the residuals from the calculated bulk moduli using Equation 3.3, where x_0 is the mean value, N is the number of data points, and the residual is represented by $x_i - x_0$: the deviation from the mean (Cort & Kenji, 2005). The results are shown in Table 3.3.

$$RMSE = \sqrt{\frac{\sum_{i=1}^{N} (x_i - x_0)^2}{N}} \tag{3.3}$$

From Table 3.3, it can be seen that the PBE functional is the best at predicting the unit cell volume for both the manually fitted unit cell volume and the automatic relaxation volume,

TABLE 3.3: Root mean square error (RMSE) of the calculated unit cell volume for the manually fitted and automatically relaxed cases, and the predicted bulk moduli from each functional

RMSE	Unit Cell Volume $\left(\text{Å}^3\right)$		Bulk Modulus (GPa)
	fitted	auto	
GGA-PW91	2.753	2.759	10.79
LDA	4.774	5.737	14.52
PBE	2.257	1.159	7.17
RPBE	3.985	2.577	14.20

as well as being the most accurate of the four functionals for the bulk modulus. The LDA functional is the least accurate of the four functionals.

The minimum energy calculated by both the Birch-Murnaghan EOS and the manually fitted data, as well as the energy from the automatic unit cell volume relaxation also have an influence on the overall decision of a functional. The system with the lowest energy will be the most stable; however, differences between the energies of different functionals do not necessarily indicate more or less stability. The minimum of the three values is shown in Table 3.4 along with the difference between the minimum and each of these three values. Since the energy differences between the systems are small they are shown in meV, while the actual minimum energy is in eV.

TABLE 3.4: Differences between minimum energies of Birch-Murnaghan EOS (B-M), manually fitted (fitted) and automatic (auto) relaxation systems and the minimum of the three energies. The values in meV show the difference to the lowest of the three methods.

MAX Phase	Functional	Minimum (eV)	B-M (meV)	Fitted (meV)	Auto (meV)
Ti_2AlC	GGA-PW91	-62.70402	0.19	0	1.80
	LDA	-68.93919	16.6	18.9	0
	PBE	-63.14903	0	1.29	28.7
	RPBE	-62.11857	0.09	0	53.2
Ti_3AlC_2	GGA-PW91	-100.58026	10.18	0	2.31
	LDA	-110.32359	37.0	37.1	0
	PBE	-100.96711	0.38	0	0.37
	RPBE	-99.39773	0	0.99	22.7
Ti_3SiC_2	GGA-PW91	-105.63352	15.4	0	24.0
	LDA	-116.06513	64.6	48.7	0
	PBE	-106.11378	16.1	0	1.98
	RPBE	-103.72298	1.42	0	30.3

Looking at the energies from the different functionals in Table 3.4, it can be seen that the LDA functional consistently has the lowest energy. However, it was also shown that LDA has the largest RMSE of the four functionals for the unit cell volume and bulk modulus (Table 3.3), therefore the LDA functional cannot be reliably used to produce accurate results.

This shows that the functional that produces the lowest energy does not automatically produce optimised lattice parameters. The functional that produces the next lowest energy is the PBE functional. This functional has the lowest RMSE in predicting the unit cell volumes, looking at both the manually fitted cell volume and the automatically relaxed volume. The PBE functional also has the lowest RMSE in predicting the bulk modulus. Therefore, PBE was deemed to be the best functional choice to take forward for further modelling of the MAX phases. Additionally, there are multiple other studies that have used the PBE functional, therefore this is not an anomalous choice (Ali et al., 2012; Lane et al., 2012; Li et al., 2013; Magnuson & Mattesini, 2017; Mauchamp et al., 2013; Son et al., 2016; Thore et al., 2014; Xiao et al., 2015; Xu et al., 2008).

3.6. Charge Density and Bader Charge Analysis

The charge density of the bulk MAX phases were calculated using VASP. The charge density allows a visual representation of the number of electrons per cubic angstrom as a three-dimensional output. The charge density output files were visualised using the program VESTA (Momma & Izumi, 2008, 2011). A two-dimensional representation of the charge density through a slice of the unit cell in the (1 1 0) plane was generated to visualise areas of high and low electron density.

While the charge density is useful to visualise electron distribution, it is unable to provide any quantitative information about the system. To calculate the charge on each atom, the Henkelman group developed code based on the theory by Bader (1985) to assign electrons to atoms based on zero flux surfaces (Henkelman et al., 2006; Sanville et al., 2007; Tang et al., 2009; Yu & Trinkle, 2011). This provides a way to determine the total charge on an atom based on the surrounding number of electrons, which is the sum of electrons within the zero flux surface. Since the pseudopotential utilises only the valence electrons in its calculation, it was necessary to combine the core electron and valence electron data (Dirac, 1929). The combined file was then run through the code. The output is the number of electrons assigned to each atom, called the Bader electrons (Equation 3.4).

$$Bader\ charge = number\ of\ valence\ electrons - Bader\ electrons \tag{3.4}$$

By subtracting the *Bader electrons* from the *number of valence electrons* of the element, the *Bader charge* can be calculated to show its charge relative to its valence state (Equation 3.4). A negative Bader charge indicates that the atom draws more electrons than it possesses in its elemental state, and for a positive Bader charge the atom donates electrons to the surrounding atoms.

For Ti the 3p, 3d, and 4s orbitals were considered valence orbitals, yielding 10 valence electrons; for Al and Si the 3s and 3p orbitals yield 3 and 4 valence electrons respectively; and for C the 2s and 2p orbitals yield 4 valence electrons. Therefore, the Ti_2AlC, Ti_3AlC_2, and

Ti_3SiC_2 unit cells have 54, 82, and 84 valence electrons respectively. The total valence electrons were compared against the total electrons calculated by the Bader code and were found to match. The charge density and Bader charge for the bulk unit cells is shown in Figure 4.2.

3.7. Density of States

The density of states (DOS) of the MAX phases were calculated for each atom in the bulk unit cells. These were resolved into the s, p, and d orbital contributions for each atom. The DOS was plotted against the energy minus the Fermi level energy. From this information one can see which orbitals of each atom are involved in bonding through hybridisation of orbitals. The strength of each bond can be seen from the energy of the DOS: a hybridised orbital at lower energy would be stronger than one at higher energy. Additionally, it is possible to determine whether a material is a conductor, semi-conductor, or an insulator by looking at the DOS over the Fermi level. A continuous DOS shows that there is no band-gap between the valence band and conduction band. The DOS's were calculated using a k-point grid twice as dense as the optimised k-point grid to ensure the resolution of the DOS would be high. A k-point grid twice as dense for the DOS is recommended by Kresse & Marsman (2012). The DOS for the bulk MAX phases can be found in Figure 4.1.

3.8. MAX Phase Surfaces

In catalytic systems, reactions occur on a surface. In PEMFCs, reactions occur on the surface of the Pt nanoparticles. Since these nanoparticles are on a support material, they will be in contact with the surface of the support material. Therefore, it will be beneficial to know which surfaces of each MAX phase would be present on a MAX phase particle. However, the layered structure of MAX phases means that there are multiple surfaces in the same plane that could be present. The most stable of these surfaces would be most likely to occur on a particle. Additionally, it will be these surfaces that will be exposed to oxidation.

The different surfaces are particularly prevalent when considering the (0 0 0 1) plane, which are the only planes considered in this thesis. Depending on the distance from the origin of the unit cell from which the surface is cleaved, different atoms will be present on the surface and in the subsurface layer. To differentiate between surfaces, the convention that was used indicates the element on the surface and the element in the subsurface layer in brackets, for example in the Ti_2AlC system, the surface with Al on the surface and Ti in the subsurface layer is denoted as Al(Ti). Similarly, for Ti_3AlC_2, the surface with Al is denoted as Al(Ti2). The labels of each layer are shown in Figure 3.8.

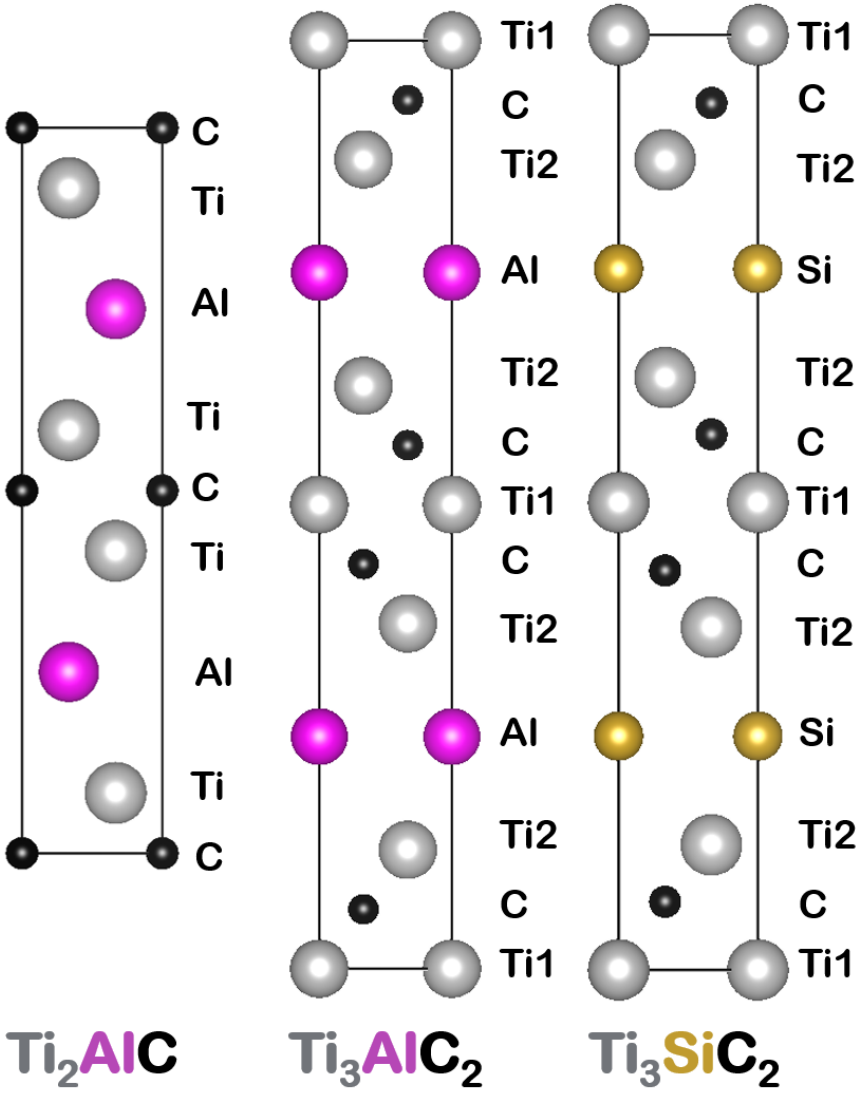

FIGURE 3.8: Atom labels for the Ti_2AlC, Ti_3AlC_2, and Ti_3SiC_2 bulk systems viewed in the (1 0 0) plane

A 2 x 2 supercell was created from the optimised bulk unit cell from which the different surfaces were cleaved. This created a unit cell with four atoms at the surface. Each system required re-optimisation of k-points and cut-off energy, as well as optimisation of the thickness of the surface slab used in the unit cell and of the size of the vacuum gap.

For layered systems like MAX phases, there will be an ordered repetition of layers from the surface extending downwards. For Ti_2AlC, there are 4 distinct layers (Al–Ti–C–Ti). A unit cell consisting of 4 atomic layers would maintain stoichiometry with the bulk phase. The combination of these 4 layers was termed a slab. A surface with the same number of atomic layers as a bulk unit cell was considered to have 2 slabs, since, for example, there are two Al layers in the bulk unit cell. Similarly, for Ti_3AlC_2 and Ti_3SiC_2, the bulk unit cell has 6 distinct layers, therefore for these systems a slab consisted of 6 layers (e.g. Al–Ti2–C–Ti1–C–Ti2). Throughout the surface calculations, the stoichiometry of the systems was maintained

by ensuring that an integer number of slabs was present in the surface unit cell.

3.8.1. k-point Grid Optimisation

The same procedure used for optimising the k-point grid for the bulk systems was used for the surface systems. However, some parameters were changed to account for the surface and vacuum system. A Methfessel-Paxton smearing of order 1 (Methfessel & Paxton, 1989) with a smearing width of 0.1 was found to provide good convergence, while maintaining an entropy term of <1 meV/atom for the surface calculations. Another factor that was taken into consideration was the dipole moment. For surfaces, the vacuum space above the surface can have an effect on the energy of the system. To account for this, the IDIPOL-tag in the input parameter file was set to 3, so that the dipole moment would be corrected in the z-direction of the unit cell.

Because of the large z-dimension of the surface unit cells, a single k-point will create a high k-point density, which can then adequately describe the small reciprocal lattice vector. Therefore, the k-point grid for surfaces is usually only optimised for the a- and b-dimensions. However, if the same k-point grid was used with different numbers of slab layers, the k-point grid density would change. Therefore, in order to keep the k-point grid density consistent, the c value was investigated for each a and b value. So, a k-point grid of $axbx1$ for a 6 slab system would have the same k-point grid density as an $axbx3$ grid for 2 slabs in a unit cell. But since only integer values for the k-point grid can be used, the c value was rounded to the nearest integer value.

Shown in Figure 3.9 is the absolute energy difference between consecutive k-point grids plotted against the irreducible number of k-points. The "x1" and "x3" after each surface shows the c parameter of the k-point grid that was used. The k-point grid was considered converged when the change in energy of the "x3" grid was less than 1 meV/atom. A cut-off energy of 600 eV was used for all k-point optimisation runs and all atoms were allowed to move freely, meaning that the system was fully relaxed, allowing the change in energy to be attributed solely to the change in k-point grid. For all k-point grid and cut-off energy optimisations, a slab thickness of 2 slabs was used.

3.8.2. Cut-off Energy Basis Set Optimisation

The cut-off energy was optimised using the same procedure as for the bulk systems. The cut-off energy was varied between 250 eV and 1000 eV. The lowest cut-off energy that was within the convergence criteria for all the surfaces of each MAX phase was selected as optimal. Figure 3.10 shows the cut-off energy convergence for Ti_2AlC, Ti_3AlC_2, and Ti_3SiC_2. Table 3.5 shows the k-point grid and cut-off energy for each surface, as well as the lowest common converged k-point grid and cut-off energy.

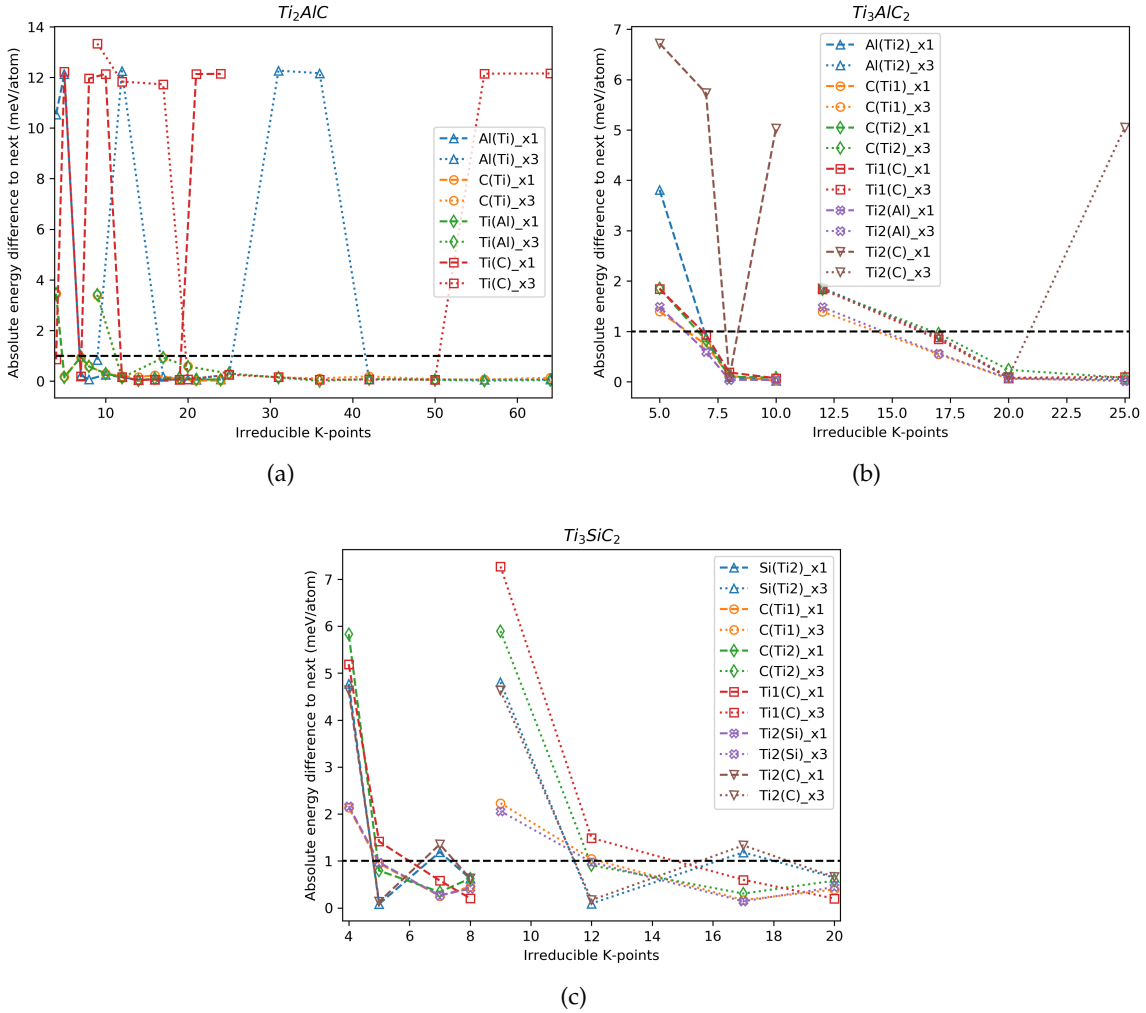

FIGURE 3.9: Energy difference at different irreducible k-points for different surfaces for (a) Ti_2AlC, (b) Ti_3AlC_2, and (c) Ti_3SiC_2. The number after the surface name represents the c k-point grid value

3.8.3. Slab Thickness

The number of atomic layers in the slab has a large influence on the calculation time. Too many layers is computationally expensive; too few and the energy of the system may not be sufficiently accurate. If there are not enough atomic layers in a slab, the vacuum from the unit cell beneath can interact through the slab to the top atomic layers and so that layer is influenced by two vacuum gaps. This has an effect on the calculated system energy, rendering it inaccurate. Therefore, the number of layers of the slab was optimised to ensure minimal calculation time while maintaining accuracy.

Usually, the number of atomic layers is varied and optimised, but to preserve stoichiometry, the number of slabs was used to optimise the thickness of the system instead. The number of slabs was varied from 2 to 5. The same cut-off energy was used for each surface within each MAX phase. To preserve k-point grid density, the c parameter of the k-point grid was changed according to slab thickness. All atoms were allowed to relax. The cleavage

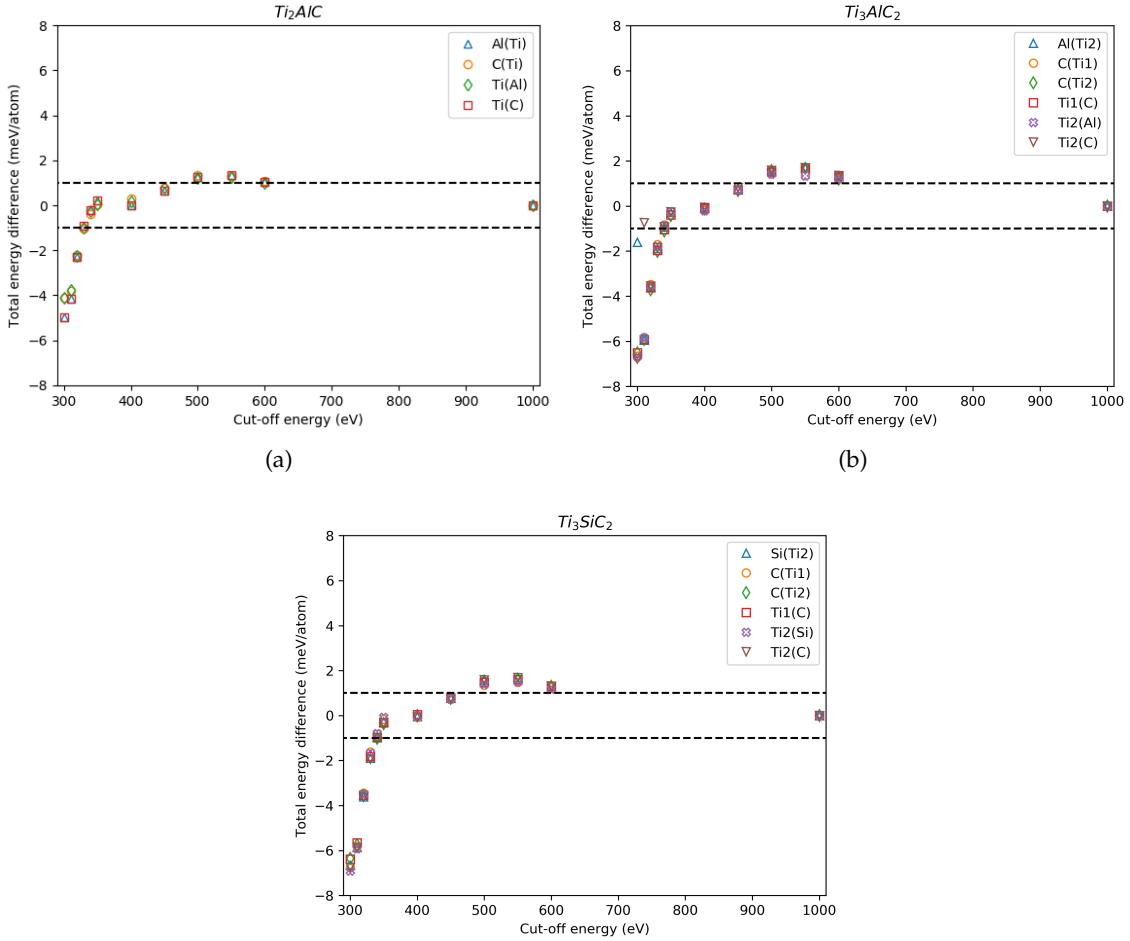

FIGURE 3.10: Energy difference at different cut-off energies for different surfaces for (a) Ti_2AlC, (b) Ti_3AlC_2, and (c) Ti_3SiC_2

energy of the systems was used to check for convergence. It was noted that each surface had a "mirror" surface, where the cleavage energy was approximately the same (less than 0.5 meV/atom for almost all slabs and surfaces). This is due to the different surfaces that are present on the top and the bottom of a slab when a surface is cleaved from the bulk. For the four possible Ti_2AlC (0 0 0 1) surfaces, Al(Ti) and Ti(C) are mirror images of each other, as are C(Ti) and Ti(Al). For Ti_3AlC_2, the pairs are Al(Ti2) and Ti2(C), C(Ti1) and Ti2(Al), and C(Ti2) and Ti1(C). Similarly, for Ti_3SiC_2, the pairs are Si(Ti2) and Ti2(C), C(Ti1) and Ti2(Si), and C(Ti2) and Ti1(C). These are summarised in Table 3.6. These pairs are simply the two top and bottom surfaces that are created when a surface is cleaved. To reduce computational cost, only one of each surface pair was optimised for slab thickness and vacuum gap.

The cleavage energy (E_C) is calculated using the surface system energy (E_S), a stoichiometric factor (n), the energy of the bulk system (E_b), and the number of surface atoms (N_S) and is shown in Equation 3.5. This is termed the bulk method since it uses the energy of the optimised bulk system as the reference energy in the equation.

TABLE 3.5: Optimised k-point grid and cut-off energy for different surfaces of each MAX phase. The bottom three rows show the k-point grid and cut-off energy used for further calculations

MAX phase	Surface	k-point grid	Irreducible k-points	Cut-off energy (eV)
Ti_2AlC	Al(Ti)	11x11x3	42	330
	C(Ti)	11x11x3	42	340
	Ti(Al)	11x11x3	42	330
	Ti(C)	11x11x3	42	330
Ti_3AlC_2	Al(Ti2)	6x6x3	17	340
	C(Ti1)	6x6x3	17	340
	C(Ti2)	6x6x3	17	350
	Ti1(C)	6x6x3	17	350
	Ti2(Al)	6x6x3	17	340
	Ti2(C)	7x7x3	20	340
Ti_3SiC_2	Si(Ti2)	7x7x3	20	340
	C(Ti1)	6x6x3	17	340
	C(Ti2)	6x6x3	17	350
	Ti1(C)	6x6x3	17	340
	Ti2(Si)	6x6x3	17	340
	Ti2(C)	7x7x3	20	340
Ti_2AlC		11x11x3	42	340
Ti_3AlC_2		7x7x3	20	350
Ti_3SiC_2		7x7x3	20	350

$$E_C = \frac{E_S - nE_b}{N_S} \tag{3.5}$$

However, the cleavage energies of the MAX phase systems using the bulk method were found to be divergent. Therefore, the approach by Lu et al. (2005) was used to calculate the bulk atom energy and the cleavage energy through a linear fitting of the series of surface system energies to the number of atomic layers. Lu et al. (2005) used surface energy in their equations, therefore the adapted equation that was used to fit the system energy and number of atomic layers is shown in Equation 3.6. Here, N is the number of atomic layers in the slab.

$$E_S = NE_b + N_S E_C \tag{3.6}$$

The cleavage energy for each surface was then recalculated using Equation 3.5. This method is termed the slab method. Figure 3.11 shows the cleavage energy calculated using the bulk method, the slab method, and the fitted cleavage energy from the slab method for each surface.

The slab and bulk methods yield similar results for the surfaces of Ti_2AlC, albeit that the slab method converges on the fitted cleavage energy better. However, for Ti_3AlC_2 and Ti_3SiC_2,

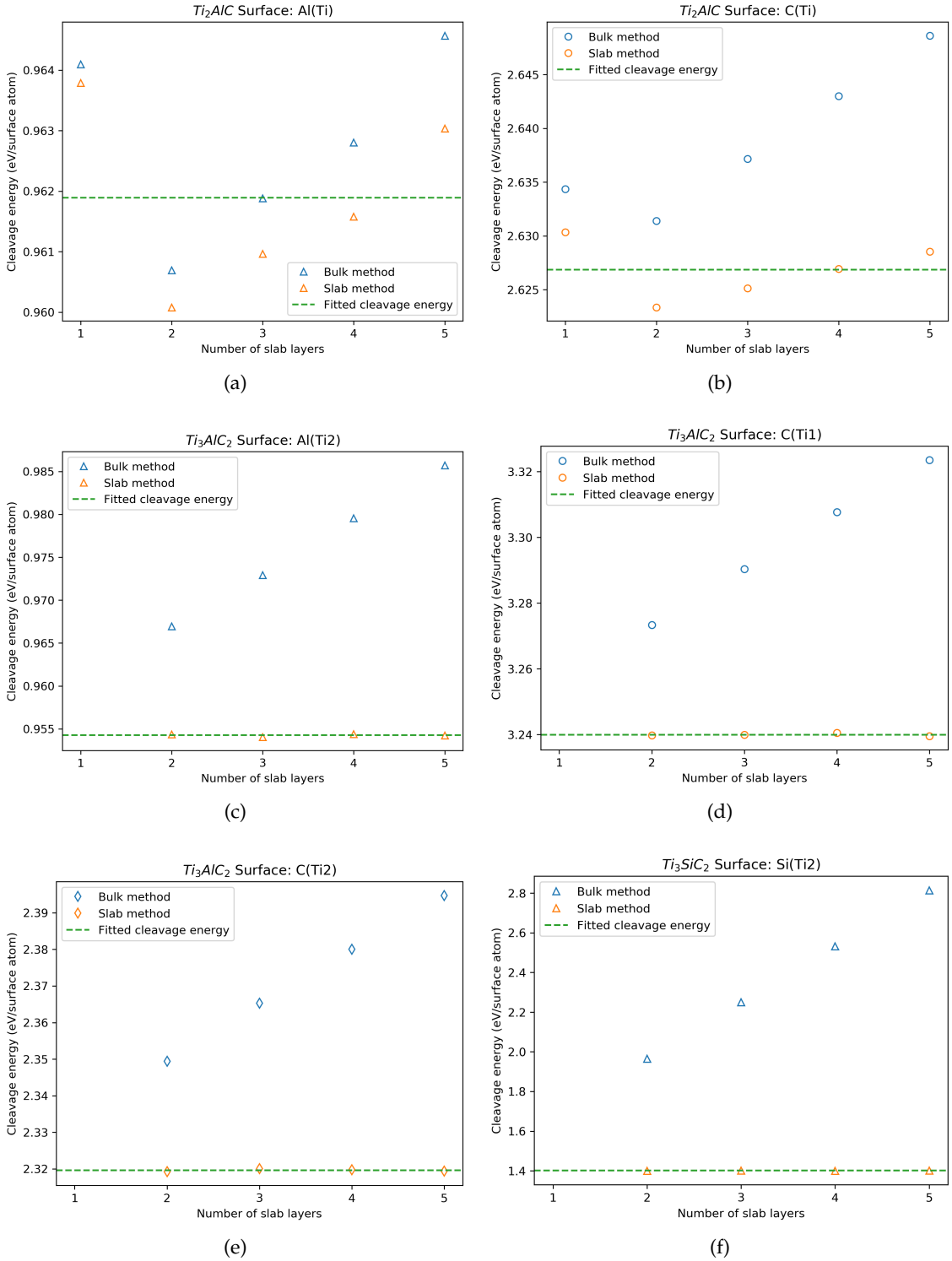

FIGURE 3.11: Cleavage energy per surface atom for (a) Ti_2AlC–Al(Ti), (b) Ti_2AlC–C(Ti), (c) Ti_3AlC_2–Al(Ti2), (d) Ti_3AlC_2–C(Ti1), (e) Ti_3AlC_2–C(Ti2), and (f) Ti_3SiC_2–Si(Ti2)

TABLE 3.6: MAX phase (0 0 0 1) surfaces and their mirror image surfaces

MAX phase	Surface	Mirror surface
Ti_2AlC	Al(Ti) C(Ti)	Ti(C) Ti(Al)
Ti_3AlC_2	Al(Ti2) C(Ti1) C(Ti2)	Ti2(C) Ti2(Al) Ti1(C)
Ti_3SiC_2	Si(Ti2) C(Ti1) C(Ti2)	Ti2(C) Ti2(Si) Ti1(C)

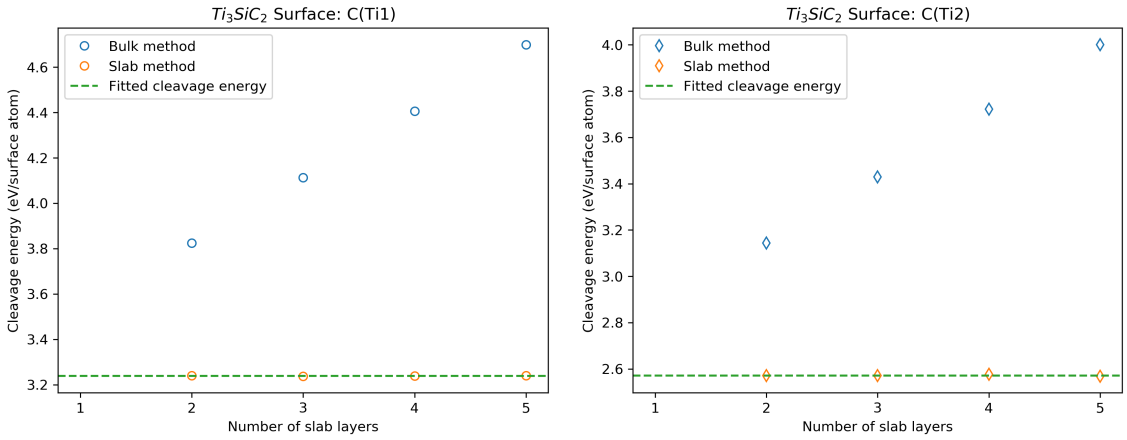

(g) (h)

FIGURE 3.11: Cleavage energy per surface atom for (g) Ti_3SiC_2–C(Ti1), and (h) Ti_3SiC_2–C(Ti2)

the cleavage energy derived from the bulk method is divergent for all the surfaces. The trend of the cleavage energy using the slab method follows the fitted cleavage energy well, as is evident from Figure 3.11. This fit was not unexpected, since the fitted cleavage energy is derived from fitting the slab energies. It is clear to see the divergence of the cleavage energies from the bulk method. However, the convergence of the slab method does not help in determining the number of slabs needed for the system to be thick enough. Therefore, the atomic distance between layers was measured and the change between slab thicknesses used to determine the number of slabs required.

3.8.4. Atomic Layer Distance Relaxation

To aid in determining the number of slabs that were needed for sufficiently accurate calculations, the distance between atoms in each layer was measured. Since a full stoichiometric slab is added when the number of slabs is increased the centre of consecutive slabs does not lie between the same atomic layers. However, by considering all the surfaces of each MAX phase it was possible to match surfaces such that the centre remained between the same

atomic layers while increasing the number of slabs in the calculation. A visualisation of these atomic layers are shown in Appendix A along with the distances between each layer.

In theory, when the surface slab is thick enough for the vacuum to have a negligible effect on the atoms in the centre of the slab, the bond length between atomic layers will be the same as the bond length in the bulk material. Therefore, to use this method, the distance between atoms in each layer was measured from the fully relaxed surfaces. The difference in atomic layer distance between slabs was then calculated to see how the bond length changed. These differences are shown in Figure 3.12, Figure 3.13, and Figure 3.14. The dotted horizontal line shows the centre of the slabs.

For Ti_2AlC, each unit slab that was added consisted of four atomic layers. Therefore, by adding two of those layers to the top of the slab and the other two to the bottom of the slab, the centre of the slab remained between the same two atomic layers, despite the surface changing. By investigating two surfaces, the surfaces can be alternated with increasing number of slabs. Additionally, the bottom of each surface continued to follow the mirror trend from Table 3.6. For Ti_3AlC_2 and Ti_3SiC_2, the centres are not as simple to align. Each slab consists of six atomic layers. However, like with Ti_2AlC, if half the layers were added to the top and bottom respectively, not all the surfaces would be taken into consideration. However, if the centres of the slabs are not aligned and there is a four/two split in atomic layers that are added to each slab, the centre will remain adjacent to the centre from the preceding slab number. Therefore, the centre of each slab is either on the horizontal dotted line or one layer beneath the line in Figure 3.13 and Figure 3.14. The title of each plot shows the layers within which the centre lies.

As expected, near the surfaces of the slabs there are large changes in the bond length as the atoms are able to relax to more energetically stable positions. For the smaller slabs, e.g. "slab2-slab3", the bond length change continues to be pronounced near the centre of the slab. However, once there are four slabs present in the surface, i.e. "slab4-slab5", the bond length changes by less than 0.005 Å near the centre of the slab. Depending on the bulk bond length, a change of 0.005 Å is between 0.172 % and 0.241 %. Therefore, slabs of 4 layers thick (or two complete unit cells) were considered the optimum slab thickness.

3.8.5. Vacuum Gap Optimisation

An important parameter to optimise to avoid interaction between the top layer of atoms of a slab and the bottom layer of atoms of the slab in the unit cell above it, is the distance of the vacuum that is built into the unit cell. This is called the vacuum gap. Too small a vacuum gap will create inaccurate energies since the top layers of the unit cell and bottom layers of the unit cell above can interact with each other through the vacuum. Too large a vacuum gap is more accurate but extends the calculation time, since it takes more computational resources to create a larger vacuum out of plane waves. The vacuum gap was adjusted from 8 Å to 12 Å for Ti_2AlC and to 14 Å for Ti_3AlC_2 and Ti_3SiC_2. These were compared to a large vacuum gap of 20 Å. The convergence criteria used was <1 meV/atom, relative to

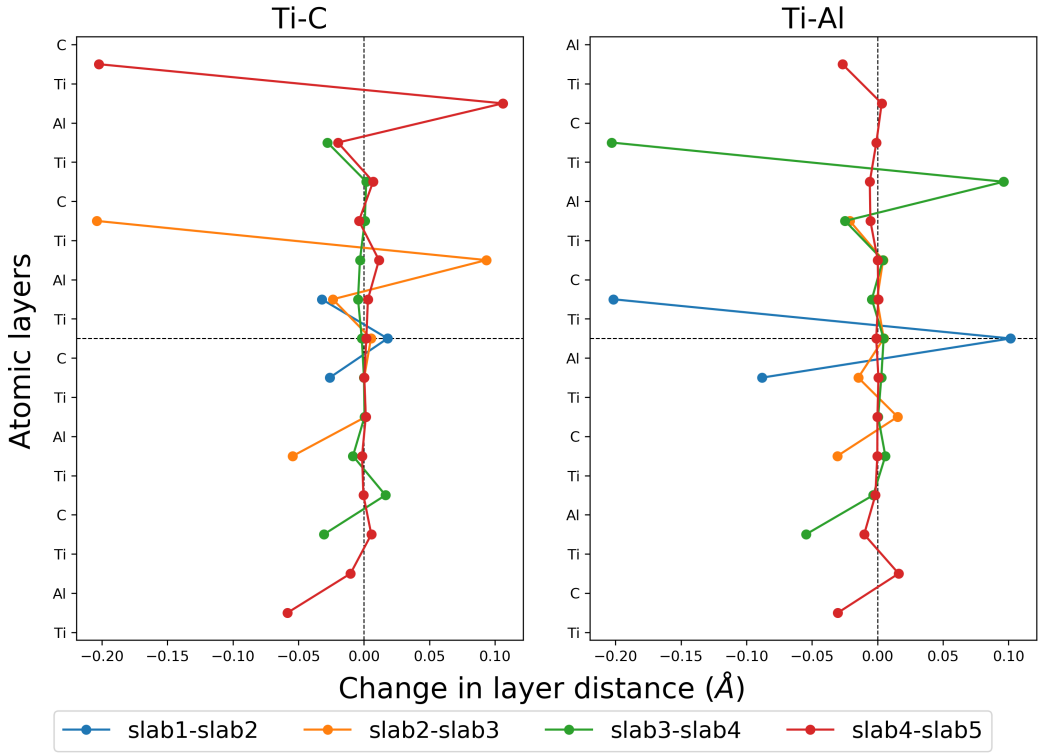

FIGURE 3.12: Difference between atomic layer distances with an increase in slab number for Ti_2AlC

the energy of the 20 Å system. The results are shown in Figure 3.15. It was determined that a vacuum gap of 12 Å was sufficient for the Ti_2AlC surfaces, and 14 Å for the Ti_3AlC_2 and Ti_3SiC_2 surfaces.

Another way to confirm that the vacuum gap is thick enough is to check the local electrostatic potential of the unit cells. In the vacuum, the electrostatic potential should decrease past zero and flatten out. The electrostatic potential was averaged over the x and y co-ordinates for each point in the z co-ordinate of the unit cell. The results are shown in Appendix A Figure A.8. It can be seen that there is no electrostatic potential in the vacuum.

Some electrostatic potential curves show a kink in the potential in the vacuum. This is not unusual and is due to VASP adjusting the dipole moment in the z direction, which can cause the electrostatic potential to show a step-like behaviour in the vacuum. This is due to the slab being asymmetric, which is this case was done to preserve the stoichiometry of the surface slabs. This asymmetry also occurs when molecules are adsorbed on one surface of the slab. The different surfaces cause the electrostatic potential from each surface to be slightly different, therefore to maintain periodicity of the unit cell, the correction factor is required (Bengtsson, 1999; Makov & Payne, 1995; Neugebauer & Scheffler, 1992).

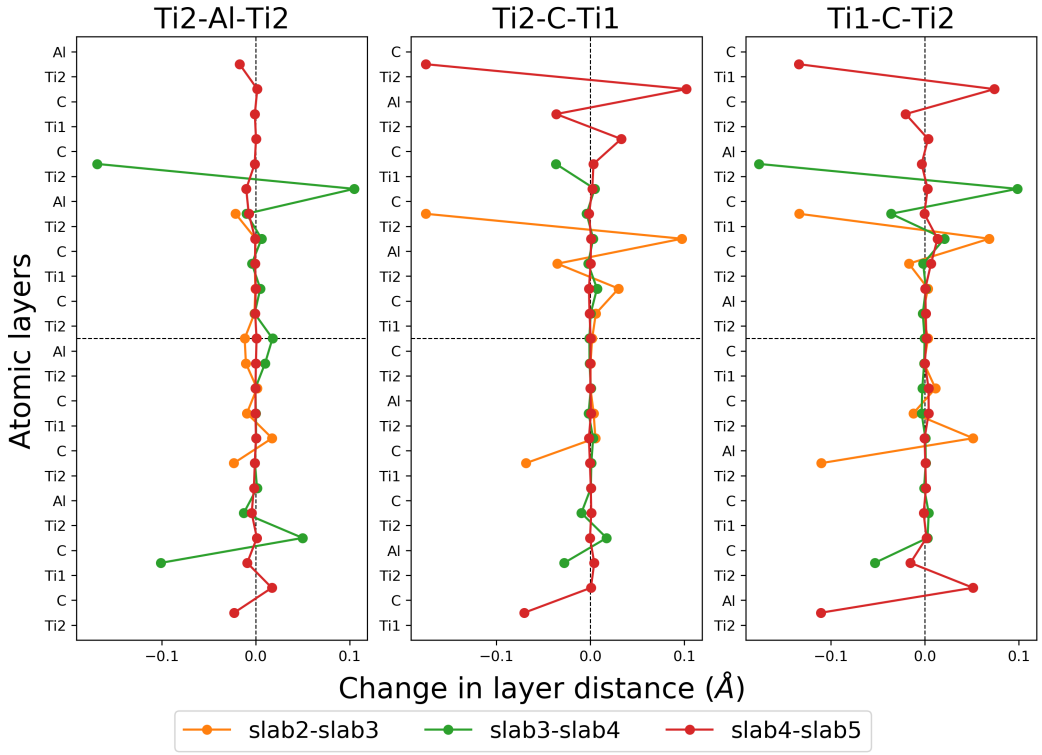

FIGURE 3.13: Difference between atomic layer distances with an increase in slab number for Ti_3AlC_2

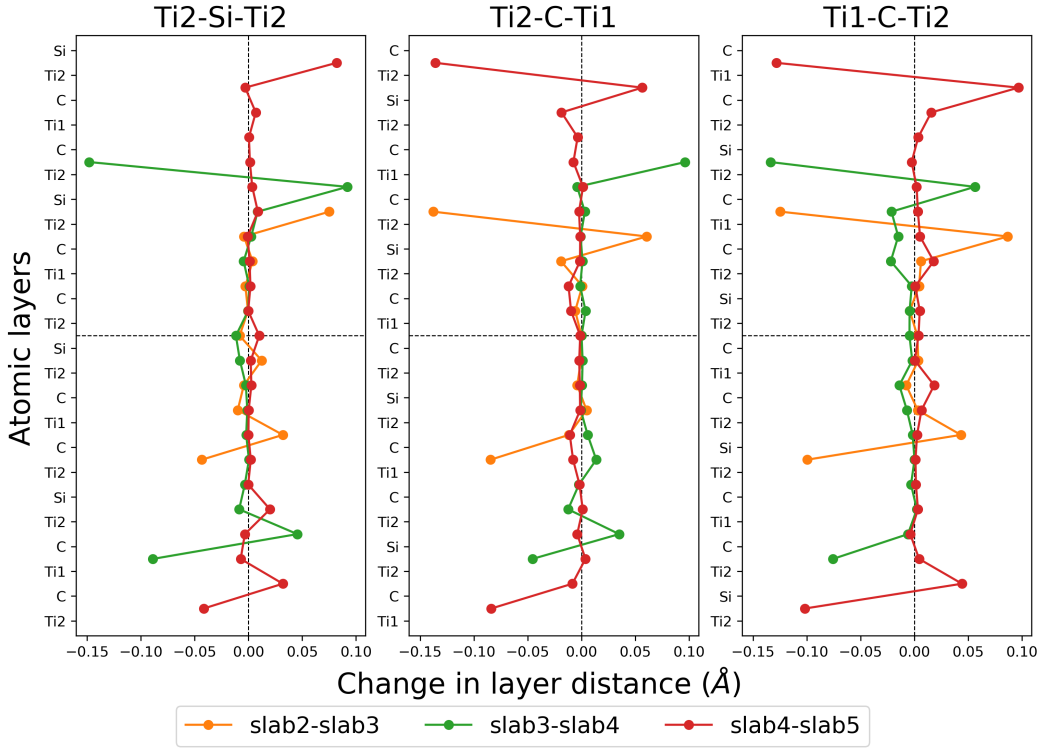

FIGURE 3.14: Difference between atomic layer distances with an increase in slab number for Ti_3SiC_2

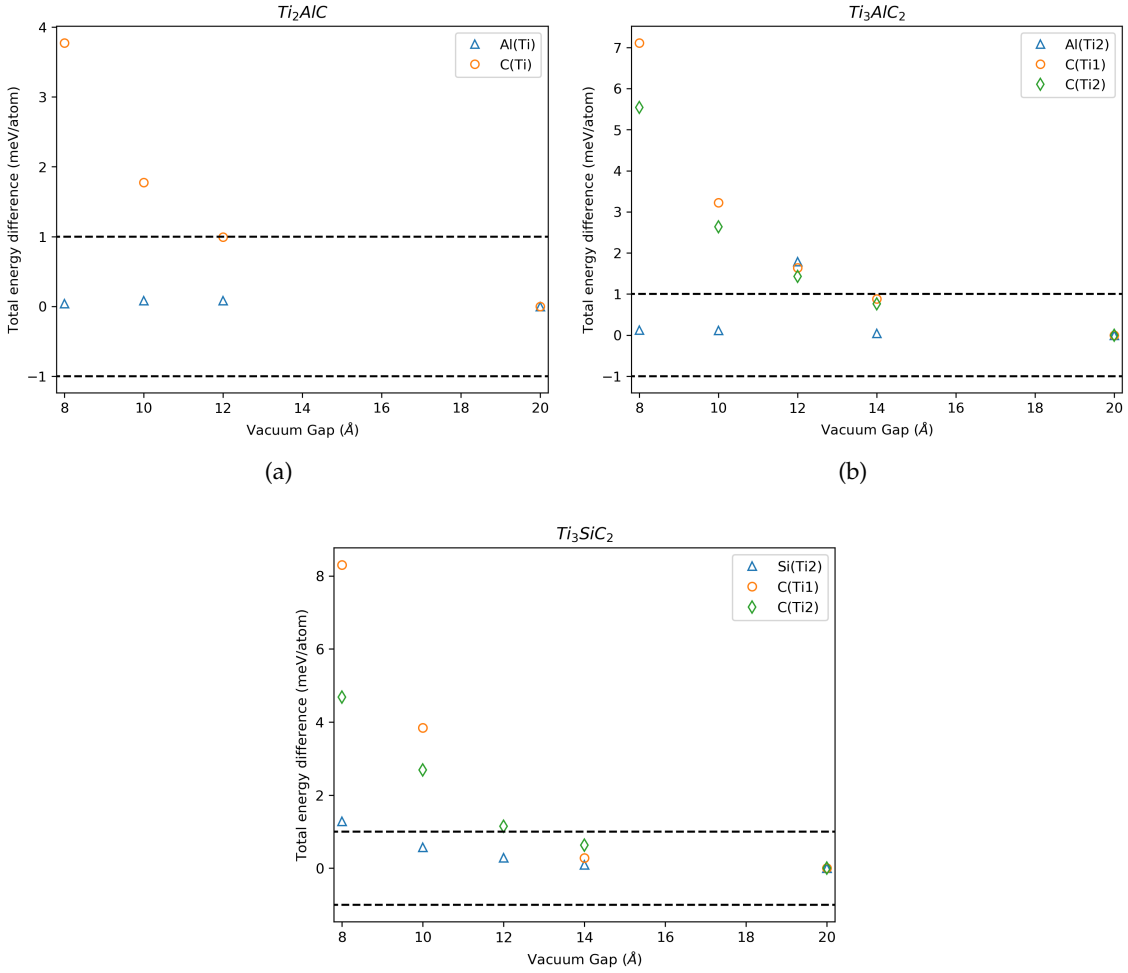

FIGURE 3.15: Vacuum gap energy difference against 20 Å for different surfaces for (a) Ti_2AlC, (b) Ti_3AlC_2, and (c) Ti_3SiC_2

3.8.6. Charge Density and Bader Charge Analysis

The charge density and Bader charge analysis was performed on each surface in the same way as in Section 3.6. A cut through the (1 1 0) plane through each surface with the Bader charge of each atom is shown in Figure 5.4, Figure 5.5, and Figure 5.6. The difference between the Bader charge of each atomic layer and the same atom in the bulk systems are shown in Figure 5.7, calculated using Equation 3.7.

$$Bader\ charge\ change_i = Bader\ charge_{i,surface} - Bader\ charge_{i,bulk} \tag{3.7}$$

3.8.7. Density of States

The density of states of the surfaces systems were calculated in the same manner as in Section 3.7. Since the position of each atom in the surface slab has an effect on the DOS,

the DOS was calculated for each layer in each surface. The Ti-d orbital, Al-p, Si-p, and C-p orbitals were compared against the bulk DOS of the same element. Additionally, the difference between the Ti1 and Ti2 atoms were taking into account for Ti_3AlC_2 and Ti_3SiC_2.

A descriptor that is used to compare the d-bands of materials is the d-band centre. The d-band centre was calculated by integrating over the normalised DOS of the d-orbital (or the p-orbital for elements without valence electrons in the d-orbital). The equation used to calculate the d-band centre is shown in Equation 3.8 (Hammer & Nørskov, 2000).

$$\begin{aligned} N(\epsilon) &= \frac{D(\epsilon)}{\int_0^\infty D(\epsilon)\mathrm{d}\epsilon} \\ d &= \int_0^\infty \epsilon N(\epsilon)\mathrm{d}\epsilon \end{aligned} \tag{3.8}$$

In Equation 3.8, D is the density of states at some energy ϵ, $N(\epsilon)$ is the normalised DOS and d is the d-band centre.

3.9. Vacancies

To investigate the oxidation resistance of the MAX phases, the formation of an Al or Si vacancy was investigated. It is known that the A group element migrates out of the MAX phase structure during oxidation (Barsoum et al., 1997; Wang & Zhou, 2002b). By looking at the formation energy of a vacancy, it is possible to determine which MAX phase would be more prone to oxidation.

3.9.1. Bulk Vacancies

A 2 x 2 x 2 supercell was created out of the optimised unit cell from which to create an Al or Si vacancy. Since in the unit cell there are only two A group atoms, removing one of them would create systems of $Ti_2Al_{0.5}C$, $Ti_3Al_{0.5}C_2$, and $Ti_3Si_{0.5}C_2$, which are not realistic. Therefore, by creating a supercell the number of A atoms was increased to 16 atoms. Removing one of the A atoms creates bulk systems of $Ti_2Al_{0.9375}C$, $Ti_3Al_{0.9375}C_2$, and $Ti_3Si_{0.9375}C_2$. These unit cells are shown in Figure 3.16.

Each system was run both with and without the vacancy present so that they could be compared directly. The optimised parameters from the bulk system were used. It is also necessary for the calculation energy to include the energy of the atom that was removed. Therefore, the energy of bulk aluminium and bulk silicon was calculated. For each of these systems, the k-points, cut-off energy, and lattice parameter were optimised. The energy per atom was then used in the calculation of the vacancy formation energy. The equation is shown in Equation 3.9, where E_V is the vacancy formation energy, E_B is the bulk energy,

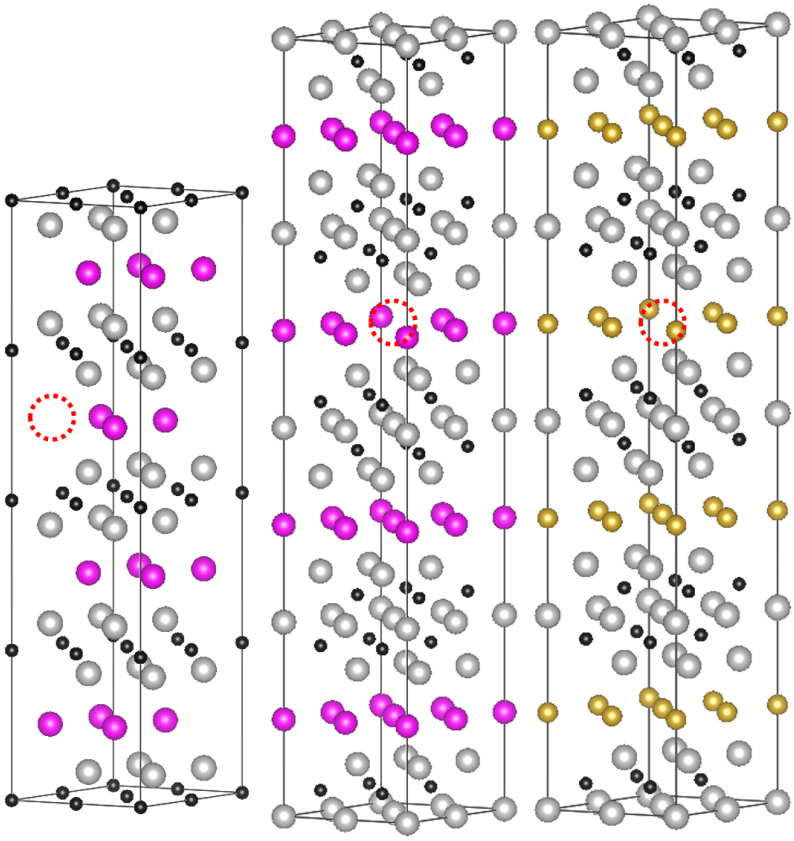

FIGURE 3.16: Bulk unit cells with Al/Si vacancies. Left is Ti_2AlC, centre is Ti_3AlC_2, and right is Ti_3SiC_2.

E_{BV} is the energy of the bulk with the vacancy, and E_M is the energy of the atom that was removed in its bulk state.

$$E_V = (E_{BV} + E_M) - E_B \tag{3.9}$$

The density of states for atoms around the vacancy as well as the charge density and Bader charge were calculated and are shown in Section 5.3.

3.9.2. Surface Vacancies

The surface slabs used so far were fully relaxed systems. To reduce computational cost, the number of slabs in each unit cell was reduced to two slabs. Seeing that the distance between atomic layers near the centre of the slabs did not change significantly from the bulk atomic layer distances (Figure 3.12, Figure 3.13, and Figure 3.14), the atoms in the bottom slab of the new unit cells were fixed in position. This then mimics the fact that the atomic layer distance doesn't change while reducing the total number of atoms in the system, thereby reducing the computational cost. Each surface then had one Al/Si atom removed from the Al/Si layer in the top slab of the surface. Vacancies were therefore present in the top four layers for Ti_2AlC and in the top six layers for Ti_3AlC_2 and Ti_3SiC_2. Again, each surface was

calculated with and without the vacancy present so that they could be compared directly. The surfaces with the vacancies for Ti_2AlC before being run are shown in Figure 3.17 along with an indication of which portion of the slab is relaxed and which layers are kept fixed.

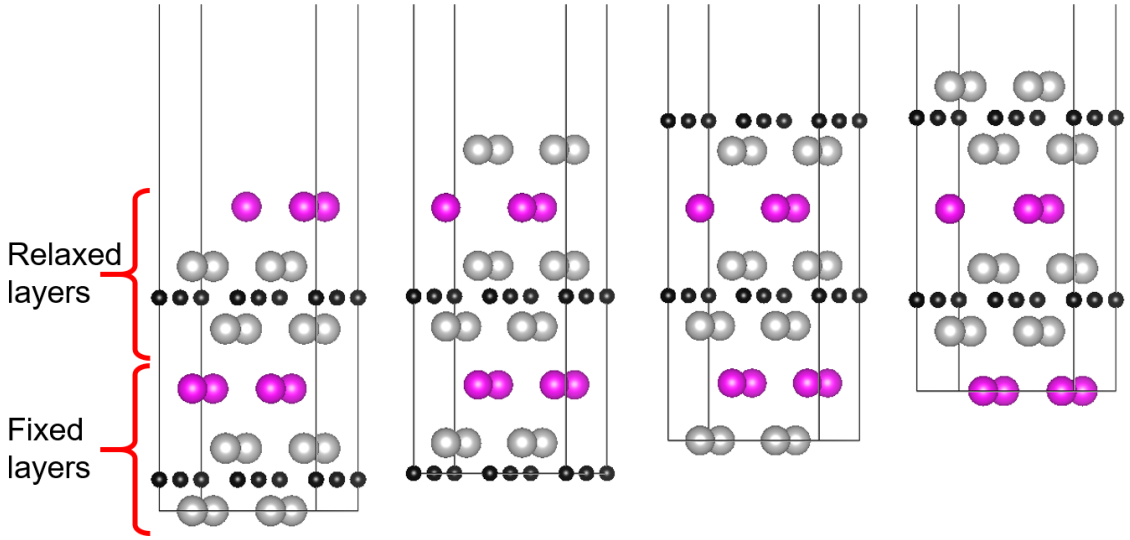

FIGURE 3.17: Vacancies for the four surfaces of Ti_2AlC. From left to right: Al(Ti), Ti(Al), C(Ti), Ti(C).

The density of states for each layer in the surface as well as the charge density and Bader charge for each layer in each surface were calculated and are presented in Section 5.4.

3.10. Boltzmann Transport Properties

To calculate Boltzmann transport properties, the program `BoltzTraP2` was installed on a virtual Ubuntu 18-04 machine. This program interpolates the transport coefficients from the band structure of a material to calculate different properties, which include the Seebeck co-efficient, electrical conductivity, thermal conductivity, and Hall co-efficient, over a range of temperatures and chemical potentials by solving the Boltzmann Transport Equation (BTE), given in Equation 2.23 (Madsen & Singh, 2006; Madsen et al., 2018). As the code has not yet been equipped to deal with spin polarised systems, the bulk and surface systems, both with and without vacancies, were rerun as a non-spin polarised calculation. The density of states of the systems with and without spin polarisation were compared and found to be in agreement. Additionally, none of the elements in the three MAX phases require spin polarisation, therefore accuracy of calculation would not be problem for non-spin polarised calculations.

`BoltzTraP2` was first run in "interpolate" mode to create a k-point grid three times as dense as the k-point grid used in the VASP calculation, using the process described by Montaña (2018), one of the authors of `BoltzTraP2` (Madsen et al., 2018). Then the program was run in "integrate" mode to integrate the band structure over a temperature range of 50 K to 400 K in 1 K increments. The conductivity data was extracted from the results files to be plotted

over the range of temperatures. To calculate the conductivity of a material, `BoltzTraP2` uses a constant relaxation time τ, and reports the value of conductivity over relaxation time as σ/τ ($\Omega^{-1}\,m^{-1}\,s^{-1}$). In theory, the relaxation time is dependent on both temperature and energy, however `BoltzTraP2` assumes a constant relaxation time and so outputs σ/τ. Assuming that this constant is reasonably accurate, the σ/τ value was converted to a σ value, and then converted to a more readily comparable resistivity value. The τ value used was 3×10^{-14} s (Barsoum, 2013: 179). This value is close to the default value of 1×10^{-14} s found in the source code of `BoltzTraP2`, available to view on GitHub.com, which is used with the built-in plotting functions of the code. The results are shown in Section 5.4.3.

4. Bulk Systems and Properties

4.1. Introduction

The optimisation of bulk Ti_2AlC, Ti_3AlC_2, and Ti_3SiC_2 is required for an accurate analysis of the properties of the systems. The results from this section will take the final results from the optimisation of the calculation parameters presented in Section 3, as well as the choice of an exchange-correlation functional, and report on the results obtained for the bulk systems. Included in that, the lattice parameters and bulk modulus will be validated against literature values. Subsequently, the bond lengths, density of states, charge density, Bader charge, and electrical resistivity of the materials will be analysed and compared.

It is well documented that the A group elements are most likely to react with their surroundings to form, for example, Al_2O_3 or SiO_2 (Barsoum, 2013: ch. 7). To investigate the oxidation resistance of the MAX phases, A group vacancies were created to simulate the effect that the removal of an aluminium or silicon atom would have.

4.2. Optimisation of Bulk Systems

The optimisation of the calculation parameters of any material in a DFT study is of first importance before any real properties can be determined. Each MAX phase was optimised independently, with the k-point grid, cut-off energy, and lattice parameters optimised for four different functionals; LDA, GGA-PW91, PBE, RPBE (see Section 3). The PBE functional was chosen for all further calculations as it provided the results which were most accurate compared to the literature. Table 4.1 compares the optimised lattice parameters and bulk modulus of Ti_2AlC, Ti_3AlC_2, and Ti_3SiC_2 to calculated and experimental values from the literature. In general, there is good agreement between the lattice parameters from this report and the experimental values. The displayed results from this work and from the compared literature are all from the PBE functional (except for Sun & Zhou (1999) who used the linear combination of atomic orbitals (LCAO) method). It is well-known that GGA functionals tend to overestimate lattice parameters (Mattsson et al., 2005), therefore the slightly larger lattice parameters calculated in this study compared to experimental values are not unexpected. However, the lattice parameters are in good agreement with lattice parameters from other DFT studies (Lane et al., 2012; Magnuson & Mattesini, 2017; Son et al., 2016; Sun & Zhou, 1999; Xiao et al., 2015).

Using the PBE functional, all of the three MAX phases showed good agreement with experimental values for the bulk modulus. For Ti_2AlC, the bulk modulus was 138.4 GPa, while the experimental value from Hettinger et al. (2005) was 144 GPa using the velocity of sound

TABLE 4.1: Calculated lattice parameters and bulk modulus compared to theoretical and experimental values from the literature

MAX phase	a (Å)	c (Å)	Bulk Modulus (GPa)	Type	Source
Ti_2AlC	3.070	13.762	138.4	DFT	this work
	3.067	13.75	136	DFT	Lane et al. (2012)
	3.08	13.77	-	DFT	Magnuson & Mattesini (2017)
	3.068	13.716	160	DFT	Xiao et al. (2015)
	3.052	13.64	-	Experimental	Schuster et al. (1980)
	-	-	144	Experimental	Hettinger et al. (2005)
	3.04	13.6	-	Experimental	Wang & Zhou (2010)
	3.063	13.645	186	Experimental	Lane et al. (2012)
	3.065	13.71	186	Experimental	Manoun et al. (2006)
Ti_3AlC_2	3.075	18.678	158.3	DFT	this work
	3.083	18.66	156	DFT	Lane et al. (2012)
	3.083	18.652	163.35	DFT	Son et al. (2016)
	3.081	18.633	177	DFT	Xiao et al. (2015)
	3.075	18.58	-	Experimental	Pietzka & Schuster (1994)
	3.072	18.54	-	Experimental	Gao et al. (2016)
	3.06	18.661	-	Experimental	Lane et al. (2012)
	3.0654	18.487	-	Experimental	Tzenov & Barsoum (2004)
	3.075	18.58	165	Experimental	Wang & Zhou (2010)
	3.075	18.578	165	Experimental	Barsoum (2000)
Ti_3SiC_2	3.0665	17.865	193.8	DFT	this work
	3.077	17.715	192.61	DFT	Son et al. (2016)
	3.077	17.688	190	DFT	Xiao et al. (2015)
	3.08	17.68	-	DFT	Magnuson & Mattesini (2017)
	3.068	17.645	-	DFT	Sun & Zhou (1999)
	3.068	17.67	-	Experimental	Jeitschko et al. (1964)
	3.065	17.67	-	Experimental	Gao et al. (2016)
	3.0665	17.671	185	Experimental	Barsoum (2000)
	3.066	17.671	-	Experimental	Jeitschko & Nowotny (1967)

to measure the bulk modulus. Hettinger et al. (2005) also report a value of 186 GPa for the bulk modulus of Ti_2AlC using a diamond-anvil cell from an as then unpublished work by Manoun, but the same value was found published in a later paper (Manoun et al., 2006). Despite the difference to the experimental bulk modulus, the calculated bulk modulus is just over 2 GPa (1.76 %) different from the calculated bulk modulus from Lane et al. (2012).

The calculated bulk modulus of Ti_3AlC_2 shows a similar agreement with the study by Lane et al. (2012), being slightly larger at 158.3 GPa compared to 156 GPa. Similarly to Ti_2AlC, the calculated bulk modulus is 4.1 % smaller than the experimental value reported by Barsoum (2000). Lane et al. (2012) also reports an experimental bulk modulus of 226 GPa for Ti_3AlC_2, however the paper that was cited reports that value for $Ti_3(AlSn_{0.2})C_2$, not Ti_3AlC_2 (Manoun et al., 2007). The experimental value of 165 GPa is reported by both Barsoum (2000) and Wang & Zhou (2010), both review papers by leading researchers, therefore this value is more trustworthy with which to compare the calculated value. This bulk modulus was measured using sound velocities.

Contrary to the other two MAX phases, the calculated bulk modulus for Ti_3SiC_2 is 4.8 %

larger than the experimental value reported by Barsoum (2000). However, it is similar to the value reported by Son et al. (2016), who also used DFT, as well as Xiao et al. (2015). These are within an agreeable range of the experimental value, which when coupled with the agreement of the lattice parameters to literature values, shows that the optimisation of all three MAX phases was successful, and that the models can be considered accurate.

4.3. Bulk Properties

The properties of the bulk MAX phases are presented in the following section. First, the bond lengths will be investigated. Then the density of states (DOS) will be analysed. Finally, the charge density and Bader charge analysis will be presented.

4.3.1. Bond Lengths

The MAX phases possess a layered structure, with M octahedral cages in which the X atom sits, and a layer of A atoms on either side of this prism (see Figure 2.4) (Barsoum, 2013). Bond lengths between the M and X atoms are much shorter than between the M and A atoms. Shorter bond lengths can show a stronger bond between atoms, depending on the atomic radius. Therefore, MAX phases are made of strongly bonded MX prisms, interleaved with a layer of weaker bonded A atoms. The bond lengths between atoms in the optimised unit cell are presented in Table 4.2.

TABLE 4.2: Bond lengths between atoms in bulk unit cells in Å. For Ti_2AlC, all Ti atoms are equivalent, but are shown using nomenclature used for the 312 systems for simplicity

Atoms	**Ti_2AlC**	**Ti_3AlC_2**	**Ti_3SiC_2**
Ti1–C	-	2.198	2.198
Ti2–C	2.110	2.078	2.076
Ti2–Al/Si	2.901	2.901	2.731

The bond lengths are in good agreement with experimental bond lengths. The bond lengths of Ti_2AlC have been reported as 2.119 Å for Ti–C and 2.855 Å for Ti–Al (Barsoum, 2013; Jeitschko et al., 1964). For Ti_3AlC_2, the Ti1–C bond length was 2.207 Å, Ti2–C was 2.089 Å, and Ti2–Al was 2.878 Å (Zhou et al., 2001). For Ti_3SiC_2, Ti1–C was 2.181 Å, Ti2–C was 2.085 Å, and Ti2–Si was 2.693 Å (Barsoum et al., 1999).

Comparing the bond lengths between Ti_2AlC and Ti_3AlC_2, it can be seen that the addition of extra Ti and C atoms does not have an effect on the bond length between Ti and Al. There is a difference in the bond length between Ti and C though, where the bond length between the inner Ti atom, Ti(1), and C is 0.088 Å longer than the Ti-C bond in Ti_2AlC. Conversely, the bond length between the Ti adjacent to the Al layer, Ti(2), and C is less than the Ti-C bond in Ti_2AlC, but only by 0.031 Å.

The bond lengths between the Ti and C atoms hardly changes between Ti_3AlC_2 and Ti_3SiC_2, indicating that the replacement of Al with Si does not have an effect on the bond lengths of the Ti-C octahedral prism. However, the bond length between Ti(2) and Al and between Ti(2) and Si decreases by 0.169 Å. This is due to Si being more electro-negative than Al, enabling it to have a stronger bond to Ti, and is therefore responsible for the smaller c lattice parameter of Ti_3SiC_2 compared to Ti_3AlC_2.

4.3.2. Density of States

The density of states of a material can give an indication into whether a material is a conductor, a semi-conductor, or an insulator. Another feature that it gives insight into is the bonding characteristics of a material. The energy level relative to the Fermi level can give an indication as to the strength of a bond between two atoms and show which orbitals are involved in hybridisation. In Figure 4.1 the total DOS as well as the orbital resolved DOS for each element is shown for the bulk MAX phases.

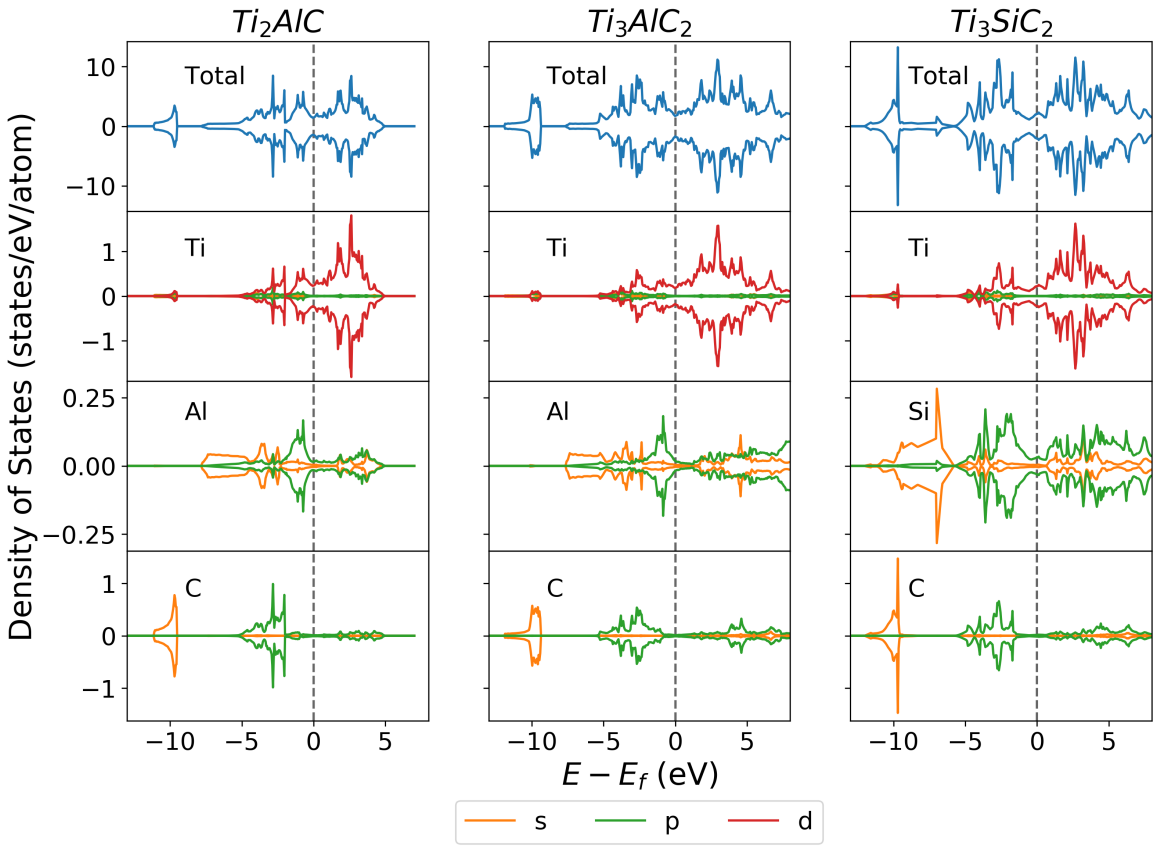

FIGURE 4.1: Orbital resolved density of states for Ti_2AlC, Ti_3AlC_2, and Ti_3SiC_2. The Fermi level is shown by the black dashed line.

The total DOS for the bulk MAX phases shows that all three MAX phases are conductive, since the DOS is continuous across the Fermi level. This means that electrons are able to move from the valence band below the Fermi level to the conduction band above the Fermi level with relative ease compared to a material where the DOS is not continuous across

the Fermi level. This is a promising initial result for the electrical conductivity of the MAX phases. The electrical conductivity results are presented later in Section 4.4.3.

Looking at the individual orbitals for each element it is possible to see which orbitals are involved in bonding to other elements. The lowest energy feature of the DOS around $-10\,\text{eV}$ belongs to the s orbital of C and the orbitals of Ti indicating that the Ti-C bond is strong, which makes sense looking at how the C atom sits in the Ti cage. The p orbital of C is also bonded to the d and p orbital of Ti just below the Fermi level. Also just below the Fermi level is the bond between the p orbital of Al and the d orbital of Ti for Ti_2AlC and Ti_3AlC_2. Ti_3SiC_2 also has the same feature for Si. The bigger DOS of Si could also indicate that it is more strongly bonded than Al in Ti_3AlC_2. The larger DOS of Si also agrees with the bond lengths of Ti2-Al/Si (Table 4.2), where the Ti2-Si bond is shorter than the Ti2-Al bond indicating a stronger bond with of Ti2 with Si.

4.3.3. Charge Density and Bader Charge Analysis

The charge density of a material is useful for analysing the electron distribution in a unit cell. One is able to visualise areas of high and low electron density and can see changes in electron density between systems. The charge density was calculated for the bulk MAX phases and is shown through a (1 1 0) plane in Figure 4.2 through two unit cells.

The Bader charge of atoms can also give information about how the charge in a system is distributed, as well as providing quantitative information for each atom. The core and valence electron data were combined and the Bader charge calculated (Henkelman et al., 2006). The Bader charge of each atom in the bulk MAX phases is shown in Figure 4.2. The formula used and the number of valence electrons for each atom that were used are presented in Section 3.6.

The first observation that is apparent from looking at the charge density is that the Ti and C atoms have a much higher charge density than the Al and Si atoms due to the red colour around them, representing an electron density greater than $0.25\ e^-/Å^3$. The large core of red colour inside each Ti atom is due to Ti having many more core electrons than the other elements, creating a much higher electron density close to the atom. Another observation is that the space around atoms in Ti_3SiC_2 has a higher electron density than in Ti_3AlC_2. This could be due to the higher electro-negativity of Si over Al, or it could be due to the smaller c lattice parameter that Ti_3SiC_2 has compared to Ti_3AlC_2, thereby having a smaller unit cell volume for the electrons and subsequently a higher density. Most likely it is a combination of the two effects.

The Bader charge analysis gives quantifiable information than the charge density as the charge on each atom can be analysed. A negative Bader charge indicates a gain in electrons, or a more negative charge than its elemental state, and vice versa for a positive Bader charge. It is plain to see that the Ti atoms have fewer electrons than in their pure metal state, and Al, Si, and C all gain more electrons. For Ti_2AlC, Ti has a Bader charge of 1.289, C has

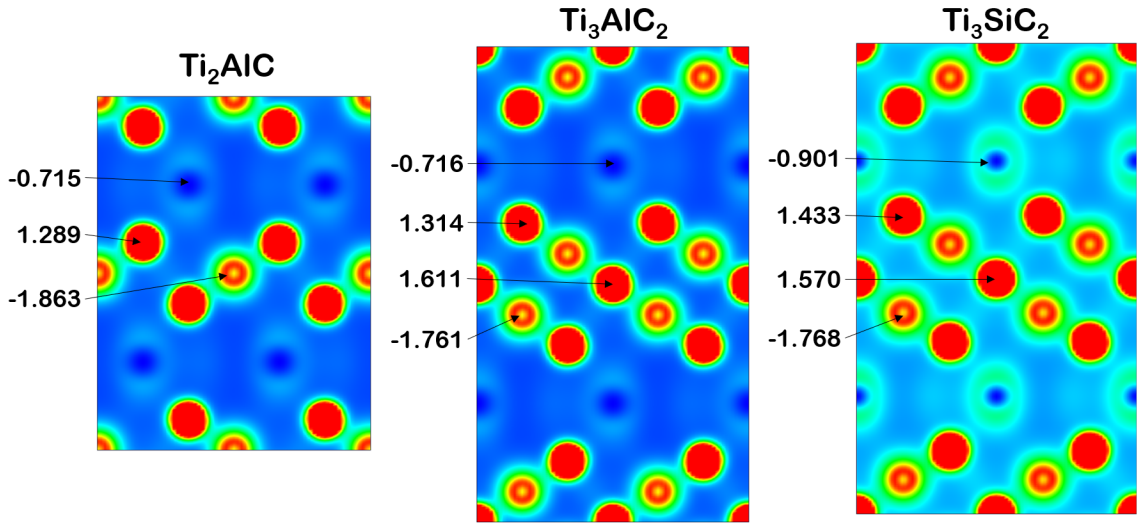

FIGURE 4.2: Charge density colour map in the (1 1 0) plane and the Bader charge of each element in the bulk MAX phases. The colour map of the iso-surface for all three goes from blue at 0 $e^-/Å^3$ to red at 0.25 $e^-/Å^3$ and above.

-1.863, and Al has -0.715. Both C and Al therefore draw electrons away from Ti strongly, although C draws 1.148 more electrons than Al does due to the higher electro-negativity of C. This makes sense given the position of the C atom in the Ti cage, along with the shorter Ti-C bonds as a consequence of the higher charge transfer and subsequently higher ionic bonding compared to Ti-Al. For Ti_3AlC_2, Al has a Bader charge of -0.716 which is effectively the same as in Ti_2AlC. This is expected since the environment of the Al atom is essentially unchanged in Ti_2AlC and Ti_3AlC_2. The C atom draws fewer electrons than in Ti_2AlC, drawing 1.761 electrons more than in its elemental state. Both the Ti1 and Ti2 atoms are more positive than the Ti in Ti_2AlC, having a charge of 1.611 and 1.314 respectively. Since the Al charge is the same, this change in Ti Bader charge is due to the increased stoichiometric ratio of C in Ti_3AlC_2. C being strongly electronegative draws electrons away strongly from Ti, and therefore the increase in C to Ti ratio (2:3 in Ti_3AlC_2 compared to 1:2 in Ti_2AlC) causes more electrons from Ti1 and Ti2 to be drawn away.

Comparing the Bader charge of the two 312 MAX phases, it can be seen that Si draws more electrons from the Ti atoms than Al does, with a Bader charge of -0.901 compared to -0.716. The charge on the C atoms is not affected much by the change from Al to Si, with a charge of -1.768, which is close to that in Ti_3AlC_2. The distribution of charge around the Ti atoms does change with the difference between the charges on the Ti1 and Ti2 atoms reducing. The Ti1 atom has a charge of 1.570 and Ti2 has a charge of 1.433 in Ti_3SiC_2. Therefore, less electrons are drawn away from the Ti1 atoms and more are drawn from the Ti2 atoms. Since the Ti2 atoms are in contact with the Si layer, and Si has a larger negative charge compared to Al, it makes sense that more electrons are drawn from Ti2.

4.4. Bulk Systems with A Group Vacancies

The vacancy formation of an A group atom was investigated to see the effect on the MAX phases should an A group atom be removed through oxidation. The energy of each MAX phase in a 2 x 2 x 2 supercell with and without an Al/Si vacancy was calculated, as well as the energy of bulk Al and Si, using Equation 3.9 to determine the vacancy formation energy (Table 4.3). The optimisation of Al and Si was performed and the results are included in Appendix A (Figure A.9 and Figure A.10).

TABLE 4.3: Vacancy formation energy of an A group atom in bulk MAX phases

MAX phase	Vacancy formation energy (eV)
Ti_2AlC	2.882
Ti_3AlC_2	2.812
Ti_3SiC_2	2.167

The vacancy formation energy of Al is slightly lower in Ti_3AlC_2 than in Ti_2AlC, suggesting that the increase in the number of Ti-C layers reduces the strength of the Ti-Al bonds (Table 4.2 and Figure 4.2), making it easier for an Al atom to be removed. Comparing the two 312 MAX phases, the vacancy formation energy of Si is 0.645 eV smaller than that of Al, suggesting that Si is more easily removed than Al. This goes against the fact that the Bader charge of Si is more negative than that of Al and the fact that the bond length of Ti2-Si is shorter than Ti2-Al. It maybe be that Si, in its diamond cubic structure, prefers to be in its pure state, hence creating a lower vacancy formation energy. Alternatively, it may be that the removal of a Si atom allows the surrounding Ti2 atoms to regain some electrons, which could potentially be more energetically favourable.

The vacancy formation energy of Al in Ti_2AlC is 5.57 % (0.152 eV) larger than that reported by Wang et al. (2008b), with a mono-vacancy formation energy of 2.73 eV. However, they used the CASTEP code with the GGA-PW91 functional, therefore the differences could be due to the functional, since PW91 typically results in larger bond lengths, and thus less strong bonds. Additionally, Wang et al. (2008b) used a smaller 2 x 2 x 1 super cell, creating a unit cell with a $Ti_2Al_{0.875}C$ stoichiometry, while the supercell used in this study (2 x 2 x 2) had a stoichiometry of $Ti_2Al_{0.9375}C$. Tan et al. (2014) also used a 2 x 2 x 1 supercell for Ti_2AlC and report an Al vacancy formation energy of 6.336 eV using VASP and the PBE functional, more than double the value calculated in this study. The much higher vacancy formation energy presented by Tan et al. (2014) could be because of the reference state of the removed atom that they used. They state that they used the energy of an isolated atom (in this case A group atom), whereas in this study (and in Wang et al. (2008b)) the energy used was from the A group element as a pure solid. This could explain the discrepancy of values. When corrected using a calculated value of a single Al atom in a 30 x 31 x 32 Å unit cell and the metallic reference energy used in this study, this value changes to -0.716 eV, very different to the value calculated in this study.

TABLE 4.4: Vacancy formation energy of Al and Si in eV in the 312 MAX phases compared to literature values. The values in brackets are the original reported values where an isolated Al or Si atom was used as the reference.

Source	Ti_3AlC_2	Ti_3SiC_2	Supercell size	Functional
This study	2.812	2.167	2 x 2 x 2	PBE
Wang et al. (2015)	2.2	2.1	2 x 2 x 1	PBE
Wang et al. (2017)	-0.8 (6.3)	1.9 (7.3)	2 x 2 x 1	PBE
Zhao et al. (2014)	2.25	1.46	3 x 3 x 1	PW91
Middleburgh et al. (2013)	-0.67 (6.38)	1.19 (6.60)	3 x 3 x 1	PBE
Zhang et al. (2013)	-	2.1	2 x 2 x 1	PBE

The vacancy formation energy of Al and Si in Ti_3AlC_2 and Ti_3SiC_2 against literature values are presented in Table 4.4 using a consistent reference energy of metallic Al or Si. The original reported vacancy formation energy is given in brackets when the authors used an isolated Al or Si atom as the reference energy. It can be seen that there is good agreement between the values calculated in this study and those calculated by Wang et al. (2015) and Zhang et al. (2013), as well as the corrected values of Wang et al. (2017) and Middleburgh et al. (2013). Middleburgh et al. (2013) states that they used the energy of a single isolated gas phase molecule as the reference energy for the vacancy atom, not an atom in its pure bulk state, which explains the discrepancy in their reported values. Wang et al. (2017) used the same method. Additionally, with Middleburgh et al. (2013) and Wang et al. (2017), the reported vacancy formation energy of Si is larger than that of Al, contrary to this study, Wang et al. (2015) and Zhao et al. (2014), while the corrected values still do not agree with those from this study.

4.4.1. Density of States

The d-band centre is used as a descriptor of the mean of the d-band DOS (Hammer & Nørskov, 2000). To investigate the effect that an Al or Si vacancy has on the d-band centre, the differences between the d-band centre with and without a vacancy were calculated and the average change for each layer above and below the vacancy is shown in Figure 4.3. Since only Ti has electrons in the d orbital, the p orbital was used for Al, Si, and C (although the term "d-band" is still used to describe the p orbital for conciseness). The d-band centre was calculated using Equation 3.8.

For all three MAX phases, the d-band centre in the vacancy layer is at a higher energy than all the other layers in the bulk. For Ti_2AlC, the d-band centre for the atoms in the vacancy layer moves to a slightly lower energy, but in Ti_3AlC_2 and Ti_3SiC_2, the d-band centre moves to a higher energy. For all the layers around the vacancy, the d-band centre shifts to lower energy, except for the Ti2 layer directly around the Si vacancy in Ti_3SiC_2. In Ti_2AlC, the C p-band has the largest change, while in Ti_3AlC_2 and Ti_3SiC_2, the Ti1 layer experiences the largest change. Despite the oscillating appearance of the change, the absolute value of the

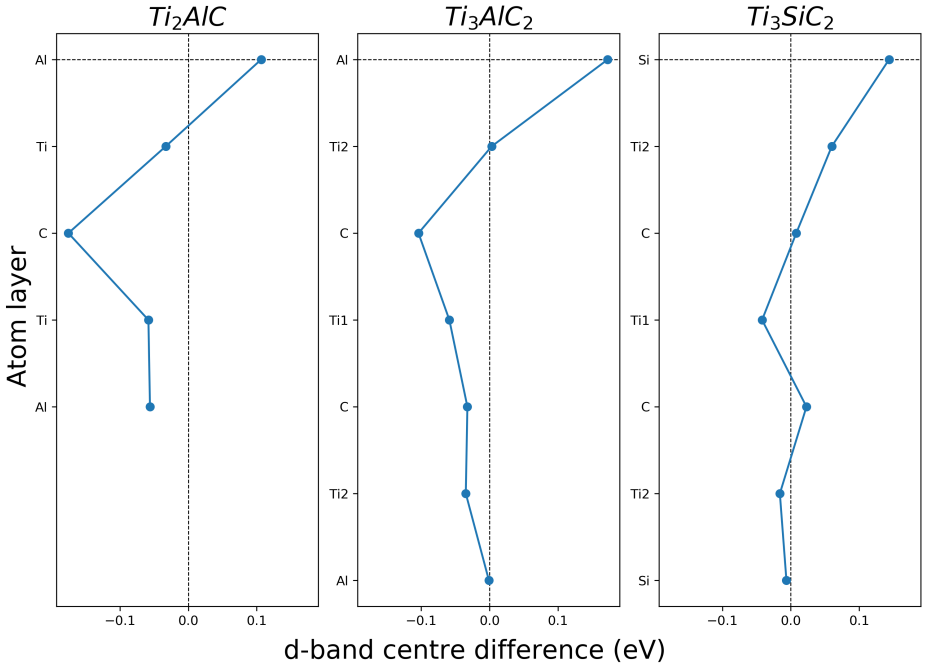

FIGURE 4.3: Difference between the d-band centre of the bulk MAX phases with and without an Al/Si vacancy. The layer with the vacancy is represented by the dashed line. The average of each layer above and below the vacancy is shown.

changes is not large, with the biggest change being 0.2 eV. The DOS for each layer with and without the vacancy is shown in Appendix B, Figure B.1.

4.4.2. Charge Density and Bader Charge Analysis

The charge density and the Bader charge were calculated for the supercells with and without the A group vacancy present. The charge density difference shows where the removed atom was, but without determining the charge density of an Al/Si atoms and including it, it does not reveal much about changes to other atoms. The Bader charge on the other hand is able to give quantitative information about how the vacancy affects the charge on the atoms in each layer. In the same manner as in Figure 4.3, the mean difference between the Bader charge of each layer above and below the vacancy layer is shown in Figure 4.4. The difference is shown for a full slab above and below the vacancy layer.

The largest change in the Bader charge is unsurprisingly in the layer where the vacancy occurs, with the biggest change of the three MAX phases in Ti_3SiC_2 at $-0.157\,e^-$/atom. The magnitude of the change in Bader charge reduces the further away from the vacancy the layer is, only really affecting the two adjacent layers. The atoms in the A group layer become more negative, indicating that they draw more electrons than without a vacancy present. The Bader charge in the Ti, or Ti(2), atoms in the adjacent layer to the vacancy becomes less positive, indicating that they donate less electrons to the surrounding atoms. In all three MAX phases, the C atoms in the second layer from the vacancy draw more electrons than they would without the vacancy.

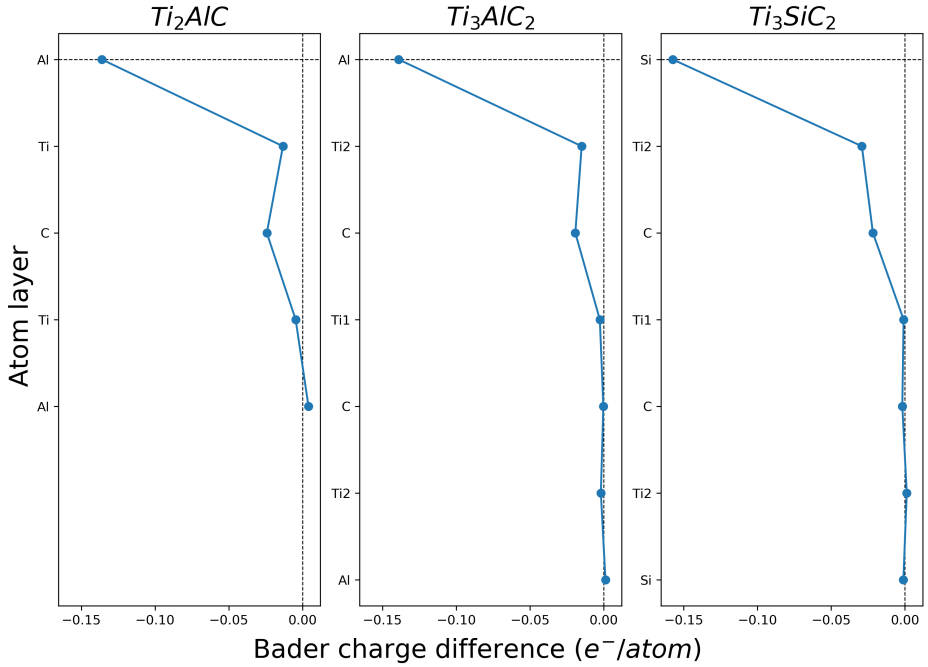

FIGURE 4.4: Difference between Bader charge in bulk MAX phases with and without an Al/Si vacancy. Values are averaged across each atomic layer.

Combining the information from Figure 4.3 and Figure 4.4, one can see why the d-band of the atoms around the vacancy shifts to a higher energy level. Valence electrons occur at higher energy levels than core electrons, with the valence electrons being closer to the Fermi level. As the atoms gain more electrons, creating a more negative Bader charge, the extra electrons fill up orbitals closer to the Fermi level. Therefore, there are more electrons at higher energy levels, which would then cause the d-band centre to shift to a higher energy level.

4.4.3. Boltzmann Transport Properties

The Boltzmann Transport Equation was solved for the bulk MAX phases, both with and without an A group vacancy present. This would provide conclusive evidence of the electrical conductivity of the MAX phases. Using a constant relaxation time value of 3×10^{-14} s (Barsoum, 2013: 179) with the results from `BoltzTraP2`, the resistivities of the bulk MAX phases with and without an Al/Si vacancy over a range of temperatures were calculated and are shown in Figure 4.5. The resistivity for each system at the chemical potential closest to the Fermi level was used. The resistivities at 300 K are presented in Table 4.5, along with literature values at room temperature. The resistivities at a temperature of 353 K are also shown to represent the resistivity at the normal operating temperature of a PEMFC (Borup et al., 2007).

Comparing the resistivities of the MAX phases to literature values in Table 4.5, it can be seen that the resistivities are all in the same range as those from literature. The resistivity of Ti_2AlC is in good agreement with that from Magnuson & Mattesini (2017) and the value for

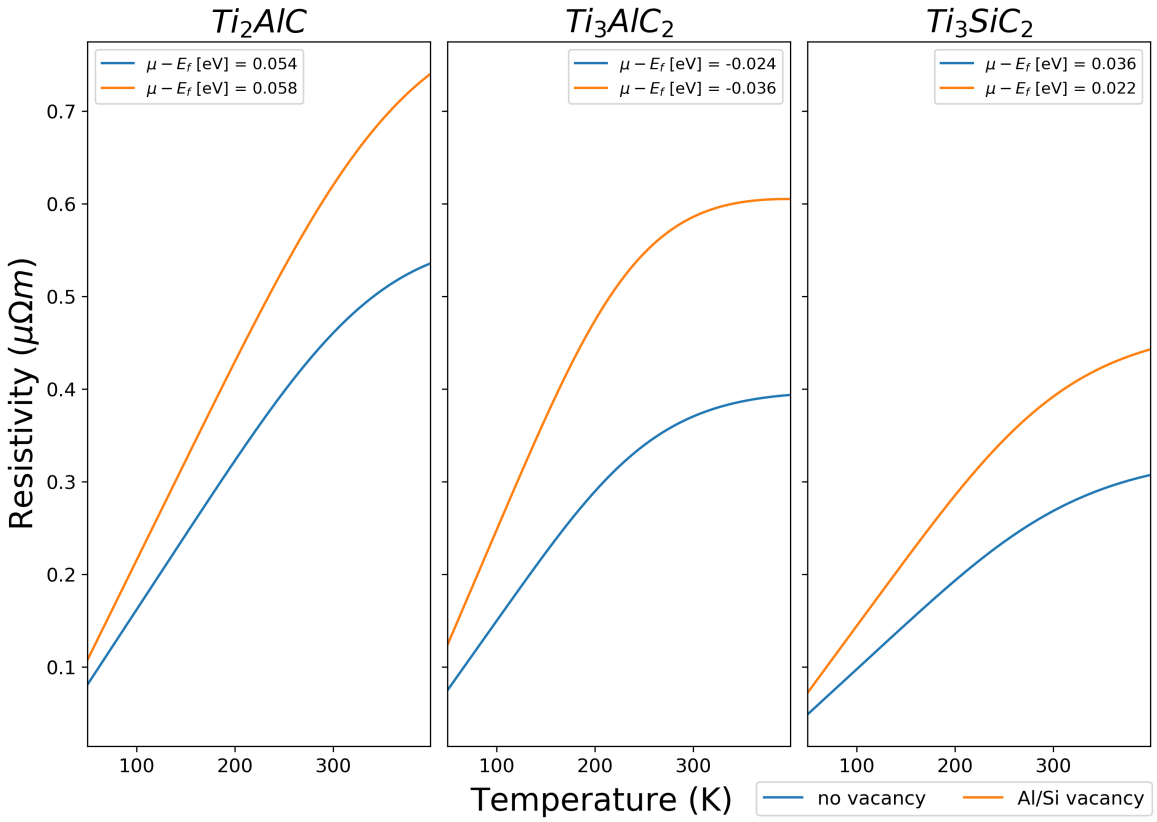

FIGURE 4.5: Resistivity of bulk MAX phases against temperature with and without an Al/Si vacancy. Resistivities are taken at the chemical potential closest to zero.

Ti_3AlC_2 agrees well with that from Scabarozi et al. (2008), while the resistivity for Ti_3SiC_2 is in good agreement with Barsoum (2000) and Magnuson & Mattesini (2017). The calculated resistivity of Ti_2AlC is greater than that of Ti_3AlC_2, which agrees with the values presented by Scabarozi et al. (2008). However, Magnuson & Mattesini (2017) reports that the resistivity of Ti_3AlC_2 is larger than Ti_2AlC. Magnuson & Mattesini (2017) is the only source that reports the resitivities for all three MAX phases, and they report that Ti_3SiC_2 has the lowest resistivity of the three, which agrees with the values calculated in this study.

The trend of the resistivity of each MAX phase in Figure 4.5 is that the resistivity increases as the temperature increases before tending towards a constant value at higher temperatures. It can be seen that Ti_3AlC_2 converges to a specific resistivity at higher temperatures, about $0.6\,\mu\Omega\,m$ for the system with no vacancy present and about $0.4\,\mu\Omega\,m$ with the Al vacancy. The other two MAX phases start to converge, but will potentially only converge at higher temperatures.

It is apparent in Figure 4.5 that the vacancy has a large influence on the resistivity of the MAX phase. With a vacancy present the resistivity increases, reducing the electrical conductivity. However, all the MAX phases are still conductive with vacancies present, therefore they should still be operational after undergoing some oxidation in a PEMFC. From the fact that the MAX phases lose electrical conductivity when a vacancy is formed, it can be deduced that the A group atom contributes towards the electrical conductivity.

TABLE 4.5: The resistivity of bulk MAX phases at 300 K with and without an A group atom vacancy. All values are in μΩ m.

Source	Ti_2AlC	Ti_3AlC_2	Ti_3SiC_2
This work —no vacancy	0.460	0.370	0.268
Magnuson & Mattesini (2017)	0.44	0.5	0.25
Barsoum (2000)	-	-	0.23
Scabarozi et al. (2008)	0.36	0.353	-
Wang & Zhou (2002a)	-	0.287	-
This work —Al/Si vacancy	0.620	0.586	0.392
This work —no vacancy (353 K)	0.509	0.387	0.293
This work —Al/Si vacancy (353 K)	0.694	0.602	0.425

Considering that a vacancy in the bulk MAX phases moves the d-band centre to lower energy (Figure 4.3), more energy is required to excite electrons into the conduction band. Therefore, there will be fewer electrons in the conduction band with a vacancy present than without a vacancy should the same amount of energy be applied during electrical conduction. This would result in the conductivity decreasing and the resistivity increasing. This could account for the increase in resistivity observed.

If the A group atoms were the primary contributor to the electrical conductivity, a reduction in the number of A atoms would logically decrease the electrical conductivity. However, looking at Figure 4.1, it was seen that the d orbital of Ti contributes the most to the DOS at the Fermi level, indicating its contribution towards electrical conductivity. With a vacancy present, the d-band centre of the Ti atoms moves to lower energy (Figure 4.3). Therefore, it can be said that as the d-band centre of the Ti atoms shifts to lower energy, the electrical conductivity decreases. This could be explained through the presence of the A group atom layer. When this layer is present, it changes the bonding characteristics of the Ti atoms, weakening the Ti-C bonds and allowing electrons to be not as strongly bound to the Ti atoms. Removing A group atoms starts to create environments closer to pure TiC, which is an insulator, meaning that the electrical conductivity reduces.

Additionally, when looking at the change in the Bader charge, it was seen that the Ti atoms directly surrounding the vacancy site show a decrease in their Bader charge (Figure 4.4). Since Ti has a positive Bader charge in the bulk systems, this decrease in Bader charge means that the Ti atoms donate fewer electrons compared to when there is no vacancy present. This supports the theory of the shifting of the d-band centre of the Ti atoms to lower energy causing the electrical conductivity to decrease, since the Ti atoms donated less electrons to the other atoms in the bulk systems and the electrical conductivity reduced. It can be said that the M atoms in a MAX phase therefore also contribute towards the electrical conductivity, particularly the d orbitals, as seen from Figure 4.1.

5. MAX Phase Surfaces and Properties

5.1. Introduction

The end-goal application for MAX phases is as a catalyst support material in PEMFCs. Platinum, the catalyst used in PEMFCs, would be deposited as nanoparticles on the surface of the MAX phase, which would then be placed as a catalyst layer in the fuel cell. The surfaces of the MAX phase that would be predominant on a particle is unknown, therefore a few potential surfaces were investigated. Due to the layered structure of MAX phases, multiple (0 0 0 1) surfaces are possible, depending on the layers between which the surface is cleaved.

This section presents results from the optimisation of some of the different surfaces, compares the calculated cleavage energies to the literature, shows how the density of states changes at the surface, and investigates the charge density and Bader charge of each surface. These results are repeated for surfaces with an A group atom vacancy present in the first slab of each surface. Afterwards, the electrical resistivity through the Boltzmann transport equations is investigated.

For this study only the (0 0 0 1) surfaces were investigated due to time constraints, however other surface planes are sure to be present on a real MAX phase particle. Therefore, it is not possible to predict the most stables surfaces overall or construct a Wulff diagram, however the most stable (0 0 0 1) can be determined. However, the methodology has now been developed for another study to investigate other surfaces.

5.2. Optimisation of Surface Systems

The step-by-step optimisation of the different surfaces of Ti_2AlC, Ti_3AlC_2, and Ti_3SiC_2 are outlined in Section 3.8. The different surfaces and their nomenclature are summarised in Table 3.6. For the optimisation steps, only one of each of the mirror surfaces was optimised, and it was assumed that the optimisation would remain valid for the mirror surface. Once the surfaces were optimised, the thickness of the surface slab was halved and the atoms in the bottom slab were fixed in position to reduce the computational cost. This was valid since the thickness of the slab was shown to be sufficient in order for the vacuum not to be felt by atoms on the opposite side of the slab (see Section 3.8).

5.3. Surface Properties

This section presents the results from the cleavage energy optimisation, compares the density of states of the surface layers to the equivalent bulk DOS, and investigates the charge density and Bader charge for the atomic layers of each MAX phase surface.

5.3.1. Cleavage Energy

Using the method from Lu et al. (2005), the cleavage energies were calculated during the process of optimising the thickness of the slab. A 2 x 2 unit cell was used to calculate the slab energies. The cleavage energies and bulk reference energies were fitted using the energies from surface systems with between either 1 and 5 slabs or 2 and 5 slabs. It was shown that this slab method of calculating the cleavage energy was accurate. The cleavage energy for each surface is shown in Table 5.1, where three cleavage energies are shown: the cleavage energy per surface atom, per unit cell and in J/m^2. Also shown is the mirror surface, which is the other surface that is produced when the surface is cleaved. Since stoichiometric slabs were used, the mirror surface is on the bottom of the slab.

TABLE 5.1: Cleavage energies of each surface for each MAX phase

MAX phase	Surface	Cleavage energy (eV/surface atom)	Cleavage energy (eV/unit cell)	Cleavage energy (J/m^2)	Mirror surface
Ti_2AlC	Al(Ti)	0.962	1.924	1.888	Ti(C)
	C(Ti)	2.627	5.254	5.156	Ti(Al)
Ti_3AlC_2	Al(Ti2)	0.954	1.909	1.867	Ti2(C)
	C(Ti1)	3.240	6.480	6.339	Ti2(Al)
	C(Ti2)	2.320	4.639	4.538	Ti1(C)
Ti_3SiC_2	Si(Ti2)	1.401	2.802	2.756	Ti2(C)
	C(Ti1)	3.239	6.479	6.373	Ti2(Si)
	C(Ti2)	2.572	5.143	5.059	Ti1(C)

Comparing the cleavage energies of the different surfaces against each other, it can be seen that there are various similarities between MAX phases. The cleavage energy for Al(Ti) in Ti_2AlC is similar to that of Al(Ti2) in Ti_3AlC_2, indicating that the Ti-Al bond and the Ti2-Al bond are very similar. This agrees with what was observed in the bond length and Bader charge of the bulk systems. In Ti_3AlC_2, the cleavage energy for C(Ti1) is the same as in Ti_3SiC_2, at 6.480 eV/unit cell and 6.479 eV/unit cell, which is unsurprising given that the Ti2-C bond lengths in bulk Ti_3AlC_2 and Ti_3SiC_2 are the same. This shows that the presence of Al and Si does not create a difference when breaking the Ti2-C bond. However, breaking the Ti1-C bond, forming C(Ti2), is different in Ti_3AlC_2 and Ti_3SiC_2, despite that fact that the Ti1-C bond is the furthest bond from the Al/Si layer and that the bond length is the same in the two bulk systems. This could be because the sum of the Ti Bader charges in Ti_3AlC_2 is lower than that of Ti_3SiC_2. The sum of the Bader charge of Ti1 and two Ti2 atoms for

Ti_3AlC_2 is 4.239, while for Ti_3SiC_2 it is 4.436. Therefore, it is more difficult to break the Ti-C cage of Ti_3SiC_2 than Ti_3AlC_2, resulting in a higher cleavage energy for the Ti1-C bond for Ti_3SiC_2 than for Ti_3AlC_2.

Looking at the surfaces with C on the top, the cleavage energy for C(Ti) for Ti_2AlC is 0.305 eV/unit cell less than the average of the cleavage energies for C(Ti1) and C(Ti2) for Ti_3AlC_2, with 5.254 eV/unit cell compared to 5.559 eV/unit cell. The average for C(Ti1) and C(Ti2) for Ti_3SiC_2 is higher than in Ti_3AlC_2, at 5.811 eV/unit cell, indicating that the Ti-C bonds in Ti_3SiC_2 could be stronger than in Ti_3AlC_2.

The cleavage energies reported by Wang et al. (2008a) show good agreement with the calculated values for Ti_2AlC. Breaking the Ti-Al bond, creating Al(Ti) and Ti(C) surfaces, has a cleavage energy of 1.888 J/m^2, compared to their reported value of 1.982 J/m^2. However, breaking the Ti-C bond, creating C(Ti) and Ti(Al) surfaces, has a cleavage energy of 5.156 J/m^2, compared to their value of 6.234 J/m^2.

The cleavage energies of the 312 MAX phases can be compared against those reported by Zhang & Wang (2007). Starting with Ti_3AlC_2, when the Ti2-Al bond is broken, the Al(Ti2) and Ti2(C) surfaces are produced. The authors report a cleavage energy of 2.07 eV for that bond. All their calculations involved a single unit cell, therefore this value can be compared to the eV/unit cell cleavage energy in Table 5.1. Breaking the Ti2-C bond produces C(Ti1) and Ti2(Si), the most unstable surfaces with a cleavage energy of 6.44 eV. The third broken bond, Ti1-C, produces C(Ti2) and Ti1(C), with a cleavage energy of 4.68 eV. These values agree well with the cleavage energies calculated in this study, of 1.909 eV, 6.480 eV, and 4.639 eV respectively.

The cleavage energies for Ti_3SiC_2 from Zhang & Wang (2007) also have good agreement with the values in Table 5.1. They report cleavage energies of 2.88 eV for Si(Ti2) compared to 1.909 eV in this study, 6.33 eV for C(Ti1) compared to 6.479 eV, and 5.07 eV for C(Ti2) compared to 5.143 eV.

5.3.2. Density of States

As in Section 4.3.2, it is possible to calculate the orbital resolved DOS for individual atoms in a surface slab, so it is of interest how the DOS of near surface atoms changes when a surface is cleaved from the bulk. Since bonding characteristics of atoms in the surface change, the DOS should give an indication as to what changes take place. The DOS was calculated on a surface system with four slabs, and the top 5 layers for Ti_2AlC, and 7 layers for the 312 systems, are shown in Figures 5.1, 5.2, and 5.3. The DOS for surfaces with either Al, Si, or C at the surface are shown. Only the d orbital for Ti, and p orbital for Al, Si, and C, are shown and are compared to the equivalent atom in the bulk system.

Looking at Ti_2AlC, the p orbital DOS of Al in Al(Ti) is affected greatly by being in the surface. The p orbital shows two big peaks above the Fermi level which are not present in the bulk system. Ti in the second layer of Al(Ti) is slightly affected and shows that same two

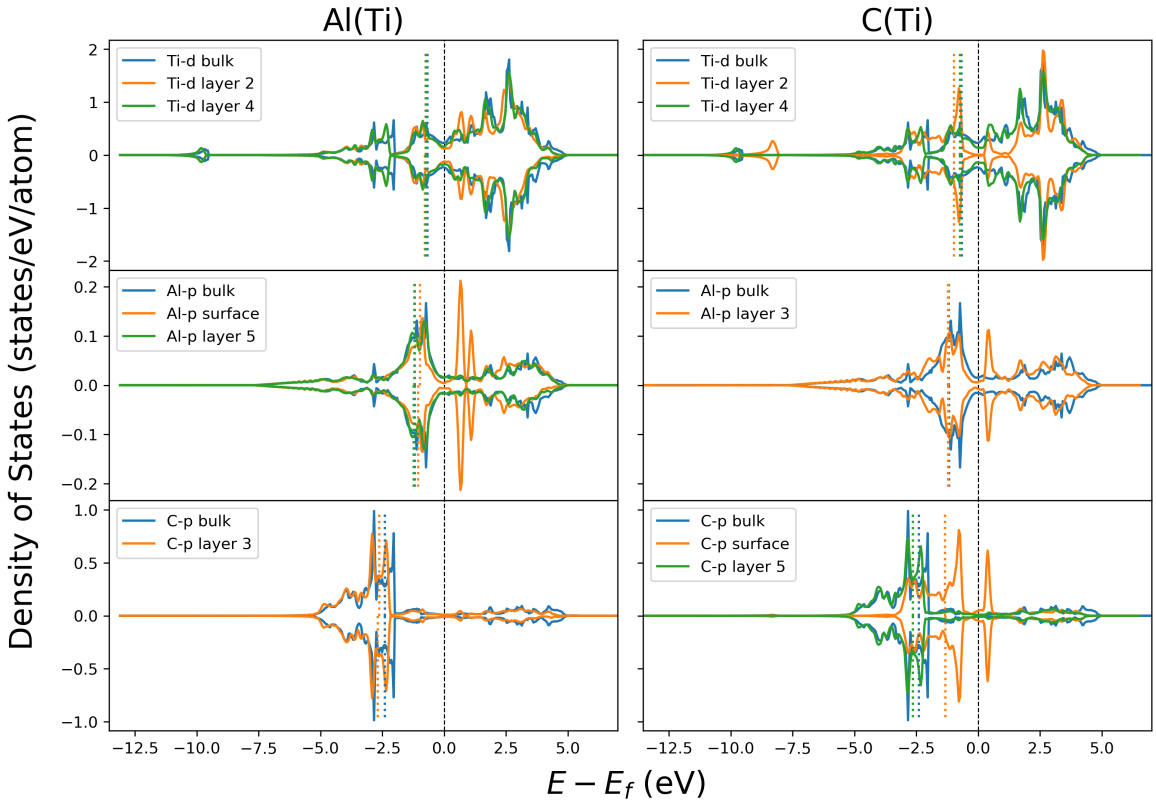

FIGURE 5.1: Density of states for the top 5 layers for surfaces in Ti_2AlC compared to bulk. Dashed lines show the d-band centre

peaks above the Fermi level, indicating that the Ti-d and Al-p orbitals show hybridisation in the surface and subsurface layer above the Fermi level. The d-band centre of C in the third layer moves to lower energy compared to the bulk and shifts the hybridisation of the C-p orbital with the Ti-d orbital of layer 4 to slightly lower energy. The last Al layer shows the same DOS as bulk Al, indicating that the Al(Ti) surface only affects the DOS four layers deep.

Looking at C(Ti) in Ti_2AlC, all five layers are affected by the surface. The DOS of the C surface layer shifts to a higher energy, with the d-band centre shifting 0.879 eV higher. The change in shape of the C surface layer DOS corresponds to the change in shape of the Ti subsurface layer DOS, which shows that the surface changes the hybridisation of the surface to subsurface bond. The d-band centre of the Ti DOS in the subsurface layer shifts to a lower energy, but the d-band centre of Al in the third layer does not move, despite the shape of the DOS changing shape. Even the d-band centres of Ti in layer 4 and C in layer 5 shift slightly, with the d-band centre of Ti shifting to a slightly higher energy and that of C shifting to a lower energy compared to the bulk. The DOS of Ti in layer 4 and of C in layer 5 show the same change in hybridisation as was seen in layer 3 and 4 of Al(Ti). Since the DOS of lower layers seems to change more in C(Ti) than in Al(Ti), one explanation could be that the Al(Ti) surface is more stable than the C(Ti) surface.

The DOS's for all the atoms in the Ti_3AlC_2 surfaces all show large differences at higher

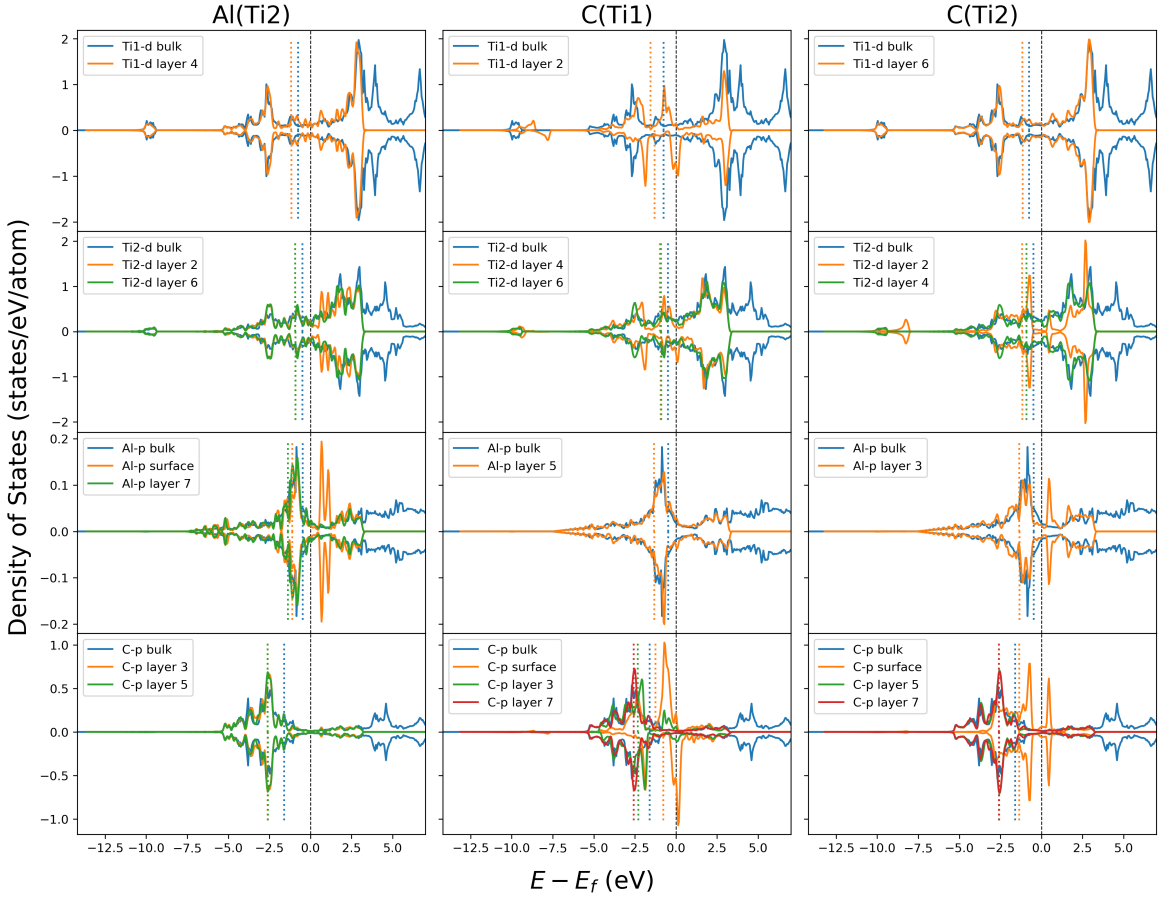

FIGURE 5.2: Density of states for the top 7 layers for surfaces in Ti_3AlC_2 compared to bulk. Dashed lines show the d-band centre

energies. The DOS of each surface atom does not extend past about 3 eV above the Fermi level, while the DOS for the bulk atoms extends to much higher energies. This means that the d-band centres are consistently at lower energies compared to the bulk d-band centres. Upon closer inspection it can be seen that these differences for some atoms lower down in the surface are superficial, as their DOS's follow the pattern of the bulk DOS very well, and simply stop just above the Fermi level. This indicates that the bulk DOS has many more states in the conduction band above the Fermi level, whereas the surface atoms do not have as many states above the Fermi level. Because of this difference, it is not practical to compare the d-band centres to the bulk d-band centres, however the d-band centres can at least be compared to other atoms in the surface slab where more than one layer of that atom is present.

In a similar manner to Al(Ti) in Ti_2AlC, the Al(Ti2) surface in Ti_3AlC_2 shows a change in DOS for the Al and Ti2 layer near the surface. The Al layer has two big peaks above the Fermi level that are not present in bulk Al. The Ti2 layer also shows some deviation in DOS above the Fermi level, showing that the hybridisation between the surface Al and the subsurface Ti2 shifts to higher energy. The d-band centre of Al shifts to higher energy but Ti2 does not shift. The DOS of layers further from the surface layer do not change much compared to the corresponding bulk DOS.

For C in the surface of C(Ti1), the DOS shows a large peak at the Fermi level, with a shift in the d-band centre to higher energy compared to the other C layers in the surface slab. Additionally, the DOS shows a difference between the up and down spins, with the peak of the down spin DOS at the Fermi level shifting to slightly higher energy compared to the up spin. This change in DOS can be seen in the subsurface Ti1 layer, where the bonding characteristics due to orbital hybridisation give the same split in the up and down DOS. This difference between the up and down spins can also be seen at lower energy, for which the hybridisation cannot be seen in this figure, but from Figure 4.1 it can be inferred that the C-s orbital experiences the same split between spin polarisation. Even the DOS of C in layer 3 and of Ti2 in layer 4 changes shape, showing their hybridisation, but not as severely as the first two layers, although the d-band centre does not shift much compared to lower layers. Some hybridisation change can also be seen between Ti2 in layer 4 and Al in layer 5 just below the Fermi level.

Similar to the C surface in C(Ti1), the DOS of the C surface layer in C(Ti2) changes shape with two new peaks around the Fermi level. The d-band centre also shifts to a higher energy relative to the d-band centre in lower C layers. However, unlike C in C(Ti1), the C surface layer in C(Ti2) does not show a difference between the DOS of the up and down spins. These two peaks in DOS around the Fermi level are replicated in the subsurface Ti2 layer, showing their hybridisation of this bond. The DOS of Al in layer 3 also shows a change in shape compared to the bulk and the lower layers' DOS, at the same energy level as the hybridisation peaks between the surface C and subsurface Ti2 atoms. Hybridisation features can be seen between Ti1 in layer 6 and the C atoms in layers 5 and 7.

The DOS of the surfaces in Ti_3SiC_2 experience the same lack of continuation at higher energies as in Ti_3AlC_2, where the DOS does not extend far past the Fermi level for the surface layers but extends much further for the bulk atoms.

The DOS of Si in the Si(Ti2) surface shows a similar change to that of Al in the Al(Ti2) surface, where the whole DOS shifts to a higher energy with peaks occurring at the Fermi level while they are not there for the Si DOS in the lower layer. The shift to higher energy can be seen by the shift of the d-band centre of the surface Si layer compared to that of the lower Si layer. Similar hybridisation features are also observed. However, unlike Al(Ti2), the second and third layers of Si(Ti2) do not show the same change as the equivalent layers in Al(Ti2).

The different layers of C(Ti1) in Ti_3SiC_2 show a similar change in DOS to those in C(Ti1) of Ti_3AlC_2, however, no difference between the up and down spins are observed like in Ti_3AlC_2. The d-band centre of the C surface layer shifts to a higher energy than the C layers lower down in the surface. The Ti1 subsurface layer also changes but does not show the same change in up and down spins as for C(Ti1) in Ti_3AlC_2. There is a new hybridisation peak at the Fermi level between the surface C layer and subsurface Ti1 layer. This high energy hybridisation peak could indicate why the cleavage energy of C(Ti1) is higher than the other surfaces, indicating an inherent instability.

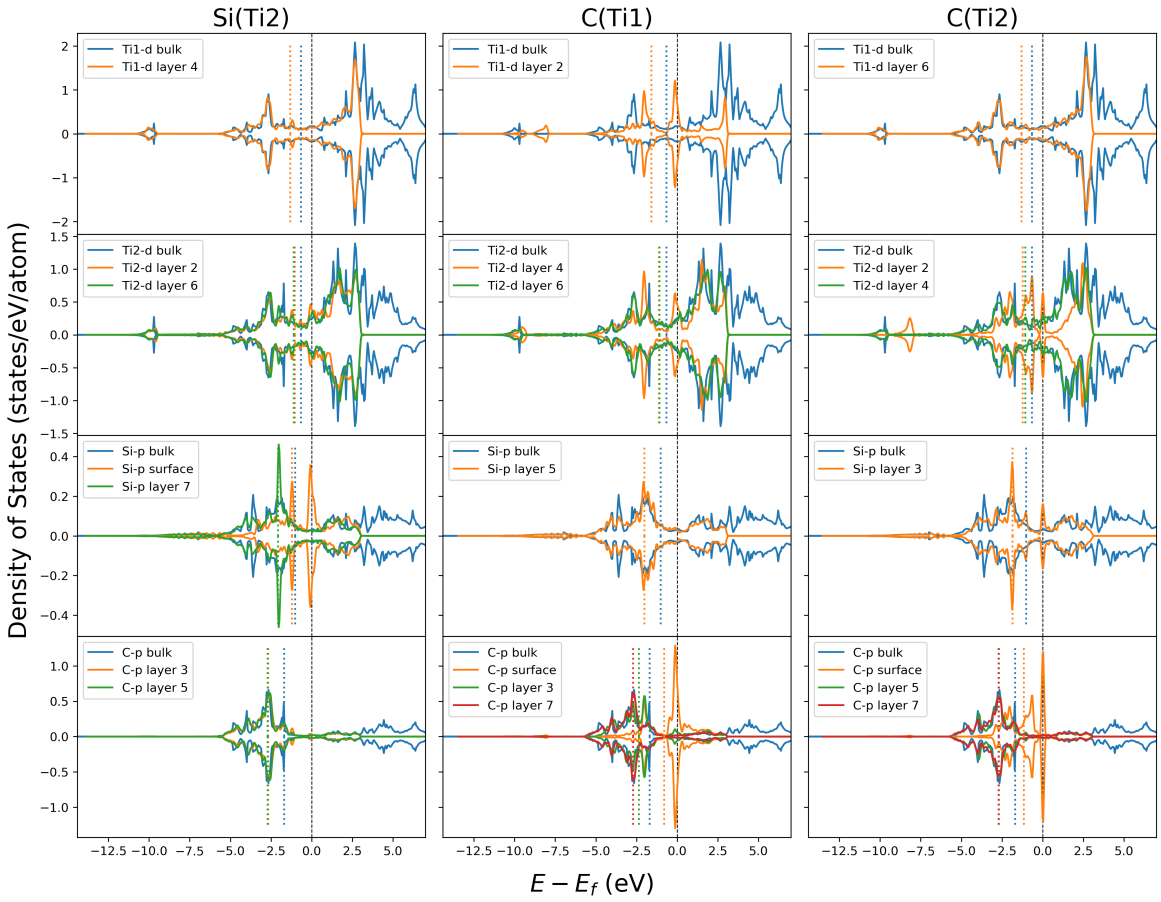

FIGURE 5.3: Density of states for the top 7 layers for surfaces in Ti_3SiC_2 compared to bulk. Dashed lines show the d-band centre

For the C(Ti2) surface in Ti_3SiC_2, the DOS of the first two layers shifts to a higher energy compared to layers further down in the slab. This is the same trend as for the C(Ti2) surface in Ti_3AlC_2. The peak at the Fermi level of the surface C is thinner than the same peak in the surface C in C(Ti1), however, the C surface in C(Ti2) has more hybridisation peaks at lower energy, indicating that the C(Ti2) surface is more stable than C(Ti1). Changes to the DOS of Si in layer 3 is also observed, however, little change is seen in the layers below that.

5.3.3. Charge Density and Bader Charge Analysis

The charge density plots of the surface systems, similar to Figure 4.2, are shown in Figures 5.4, 5.5, and 5.6. A slice through the (1 1 0) plane is shown through the 2 x 2 unit cell with 4 slabs. A small portion of the vacuum gap is shown above each slab, with the top of the vacuum from the unit cell below shown at the bottom. The Bader charge for each layer of atoms is shown next to each charge density plot. On the left of each surface plot are the Bader charges for Ti and on the right for Al/Si and C. Additionally, the mirror, or complementary, surface of each surface can be seen on the bottom of each slab for all three MAX phases.

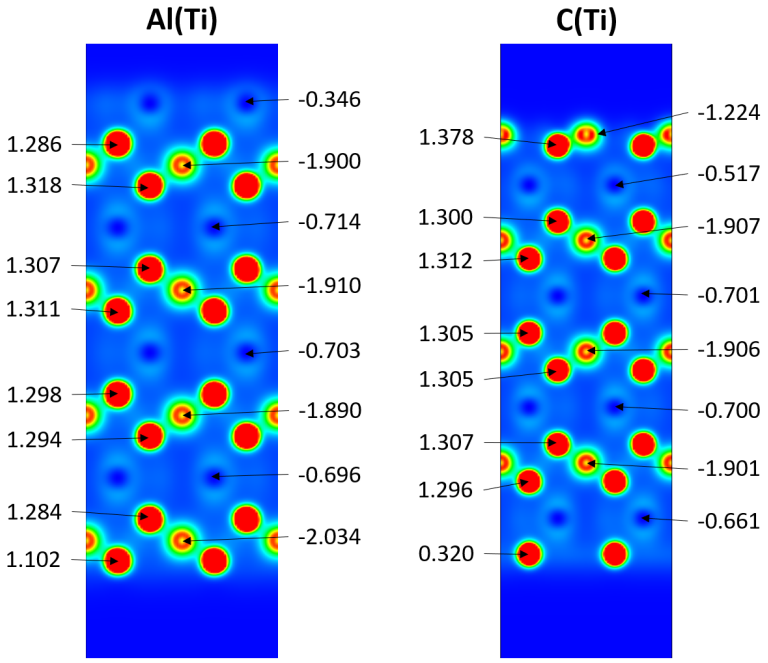

FIGURE 5.4: Charge density colour map in the (1 1 0) plane and the Bader charge of each element for surfaces of Ti_2AlC. The colour map goes from blue at 0 $e^-/Å^3$ to red at 0.25 $e^-/Å^3$ and above

Analysing the Ti_2AlC surfaces, it can be seen that the Al(Ti) and C(Ti) surface charge densities display the same characteristics as bulk Ti_2AlC. Looking at the surface layer of C(Ti), it can be seen that the C atoms undergo relaxation and are closer to the Ti atoms as the shape of the charge density around the C atoms flattens. This was also evident through the change in bond length near the surface (Figure 3.12)

The charge density plots of the surfaces of Ti_3AlC_2 show similar characteristics to that of the bulk. Similar relaxation of surface C atoms to C(Ti) of Ti_2AlC can be seen in the C surface layers of C(Ti1) and C(Ti2) (see also Figure 3.13).

For the surfaces of Ti_3SiC_2, the same increase in charge density between atoms compared to those of Ti_3AlC_2 as is present in the bulk systems can be seen, along with the relaxation of the C surface atoms in the C(Ti1) and C(Ti2) surfaces (Figure 3.14).

To get a better understanding of how cleaving surfaces changes the charge density, the difference between the Bader charge and the Bader charge of the corresponding bulk element for each MAX phase was calculated. This is shown in Figure 5.7. The Bader charges are aligned to their atomic layer.

With reference to Figure 5.7, it can be seen that the Bader charge has the greatest magnitude of change near the surface, usually only in the outer three layers. Surfaces with Al, Si or C in the surface layer show an increase in Bader charge, thereby becoming more positive. The surfaces with C at the surface show a greater change in Bader charge than the surfaces with Al / Si on the surface, as well as flattening in shape. The subsurface Ti layers do not show

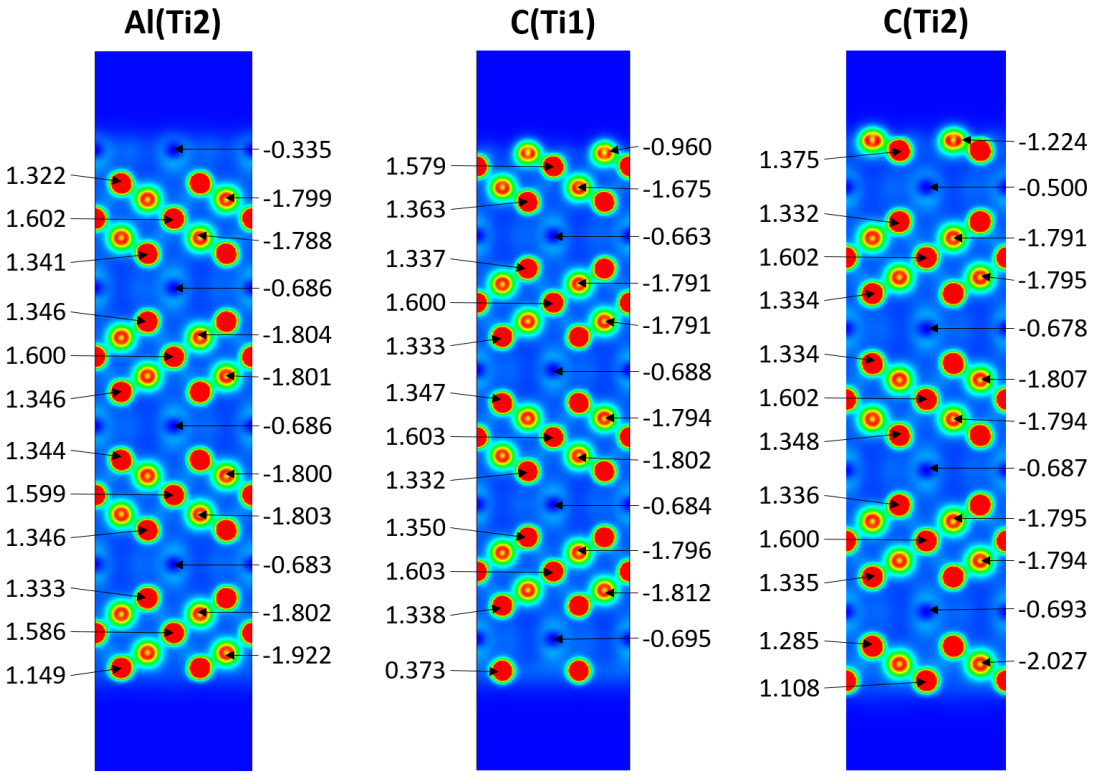

FIGURE 5.5: Charge density colour map in the (1 1 0) plane and the Bader charge of each element for surfaces of Ti_3AlC_2. The colour map goes from blue at 0 $e^-/Å^3$ to red at 0.25 $e^-/Å^3$ and above

a big change in Bader charge, thereby having a very similar Bader charge to the equivalent bulk Ti atoms.

At the bottom of each surface slab, where surfaces with Ti are present, the Bader charge of the surface layer decreases, thereby losing fewer electrons compared to Ti in the bulk. The change is the greatest for the Ti(Al), Ti2(Al), and Ti2(Si) surfaces, showing that the presence of the A group atom in the subsurface causes a large change in the Bader charge of the Ti surface atoms. This makes sense since the environment in which the surface Ti atoms find themselves is very different from their bulk environment. This might indicate that these surfaces are unstable. For the 312 MAX phases, the Ti1(C) surface has a larger change than the Ti2(C) surface, suggesting that the Ti2(C) surface is more stable than the Ti1(C) surface.

Comparing the cleavage energies against the change in Bader charges, it can be seen that the surfaces with the lower cleavage energies have a smaller change in the Bader charge of the surface atoms. For Ti_2AlC, the cleavage energy of Al(Ti) is lower than that of C(Ti), and the combined change in surface atom Bader charge change is smaller for Al(Ti) than for C(Ti). For Ti_3AlC_2, the cleavage energy of Al(Ti2) is the lowest, followed by C(Ti2), and then C(Ti1). The change in Bader charge for Al(Ti2) is the lowest of the three surfaces, followed by C(Ti2), and the C(Ti1). The same trend is observed for Ti_3SiC_2, where the surface with the lowest cleavage energy, Si(Ti2), has the smallest change in Bader charge for the surface

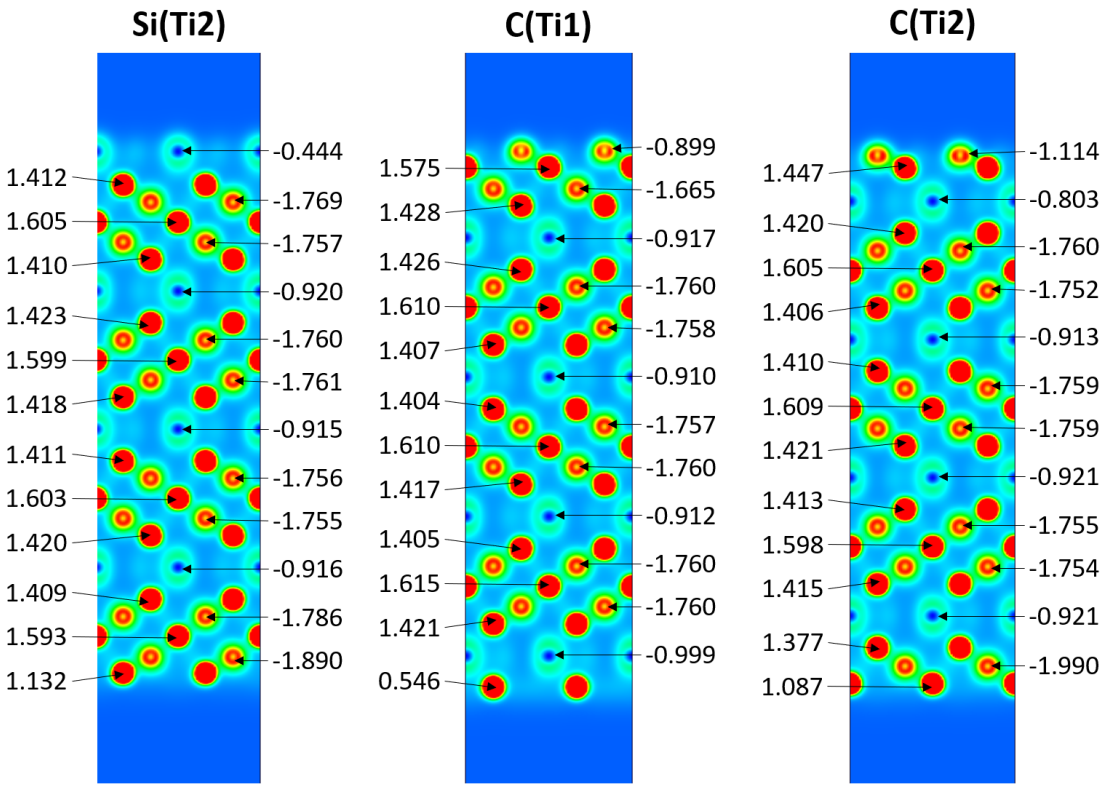

FIGURE 5.6: Charge density colour map in the (1 1 0) plane and the Bader charge of each element for surfaces of Ti_3SiC_2. The colour map goes from blue at 0 $e^-/Å^3$ to red at 0.25 $e^-/Å^3$ and above

atoms. Since surfaces with a lower cleavage energy tend to be more stable, it could be concluded that surfaces with a small change in Bader charge are more stable than surfaces with a large change in Bader charge at the surface.

Using this observation, it can be seen that the surfaces with the A group atom in the subsurface are likely to be unstable, since the change in Bader charge at the surface is large. At the top end of those slabs, surfaces of C with Ti2 in the subsurface are more stable than C surfaces with Ti1 in the subsurface layer.

If this Bader charge trend holds for surfaces within the same slab, it can be said that for Ti_2AlC the Ti(C) surface is more stable than the Al(Ti) surface since the change in Bader charge of Ti in Ti(C) is less than that of Al in Al(Ti). However, if the first two layers both need to be accounted for, then Al(Ti) would be more stable than Ti(C), since the total change in Bader charge of the first two layers of Al(Ti) is 0.367 e^-, while the top two layers of Ti(C) have a Bader charge change of 0.728 e^-.

Comparing Figure 5.7 to Figure 5.1, the change in Bader charge at the surface correlates with a change in the d-band centre of that layer. Looking at the Al(Ti) surface, the d-band centre of the Al surface layer shifts to higher energy, while the Bader charge increases, meaning that the Al atoms draw fewer electrons from the surrounds. The same thing is true in the C(Ti) surface, where the d-band centre of the surface C layer shifts to higher energy while

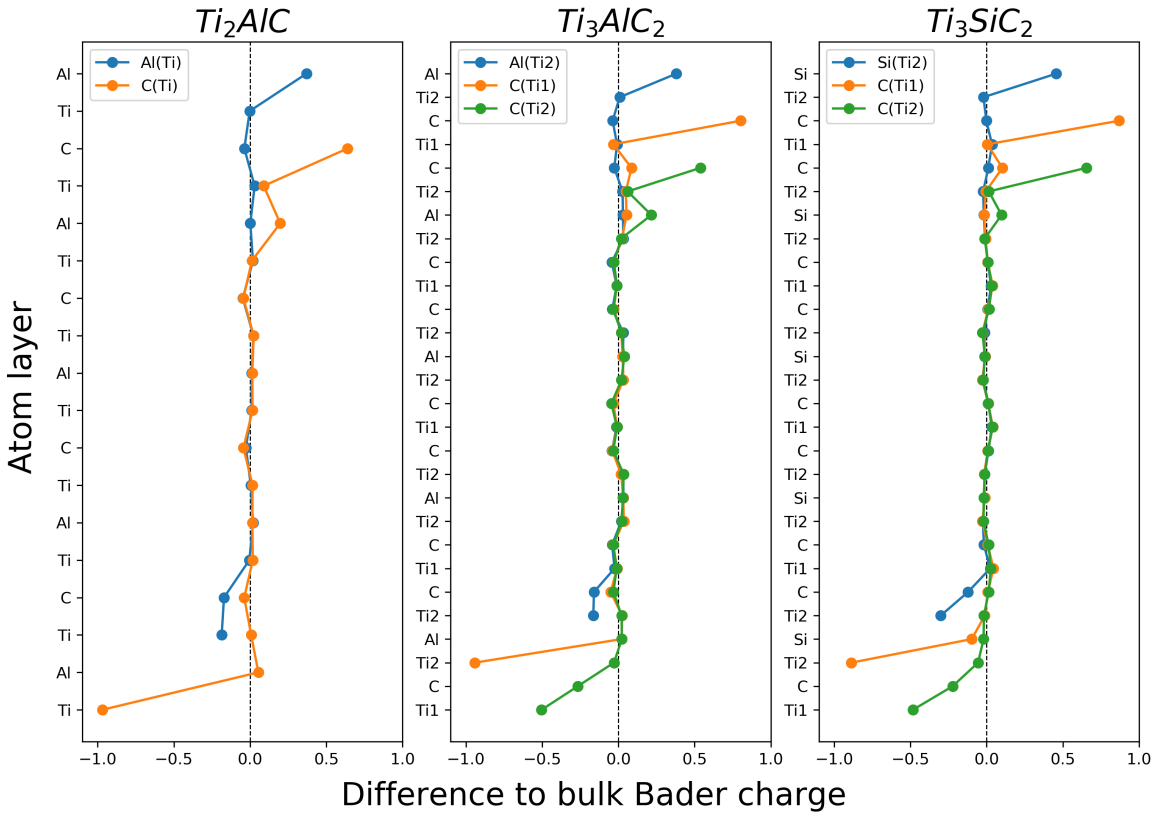

FIGURE 5.7: Bader charge difference for each surface of Ti_2AlC, Ti_3AlC_2, and Ti_3SiC_2 compared to the corresponding bulk Bader charge

the Bader charge becomes more positive. Or more generally, an atomic layer that shows an increase in Bader charge will show a shift in the d-band centre to higher energy.

Due to the DOS not extending far past the Fermi level for the 312 systems, it is not as easy to compare the change in d-band centre to the change in Bader charge. However, the d-band centre of the surface layer can be compared to the d-band centre of a layer further down in the slab. Therefore, it can be seen that the same trend holds for Al in the surface of Al(Ti2) of Ti_3AlC_2, where the d-band centre shifts to a higher energy compared to that of the Al layer in the seventh layer. It can also be seen in the C layer at the surface of C(Ti1) and C(Ti2) where the d-band centre shifts to a higher energy compared to the d-band centre of lower C layers. The same is true for Si in the surface of Si(Ti2) of Ti_3SiC_2, as well as the C surface layers of C(Ti1) and C(Ti2).

5.4. Surfaces with A Group Vacancies

The vacancy formation of an A group atom was determined for the surfaces of each MAX phase to investigate how the vacancy formation would change in each surface. Surfaces two slabs thick were constructed with a 2 x 2 unit cell. It was demonstrated in Section 3.8 that surfaces two slabs thick were thick enough to prevent vacuum interaction through the slab. The atoms in the bottom slab were fixed in position, while the atoms in the top slab

were allowed to relax (Figure 3.17). Each surface was calculated with and without an Al/Si vacancy in the top slab. The vacancy formation energy is shown in Figure 5.8, where the atom layer represents the atomic layer beneath the surface where the vacancy occurs. The order of layers from the surface down is as follows: for Ti_2AlC, Al(Ti) – Ti(Al) – C(Ti) – Ti(C); for Ti_3AlC_2, Al(Ti2) – Ti2(Al) – C(Ti2) – Ti1(C) – C(Ti1) – Ti2(C); and for Ti_3SiC_2, Si(Ti2) – Ti2(Si) – C(Ti2) – Ti1(C) – C(Ti1) – Ti2(C). One set of each of these layers constitutes a slab.

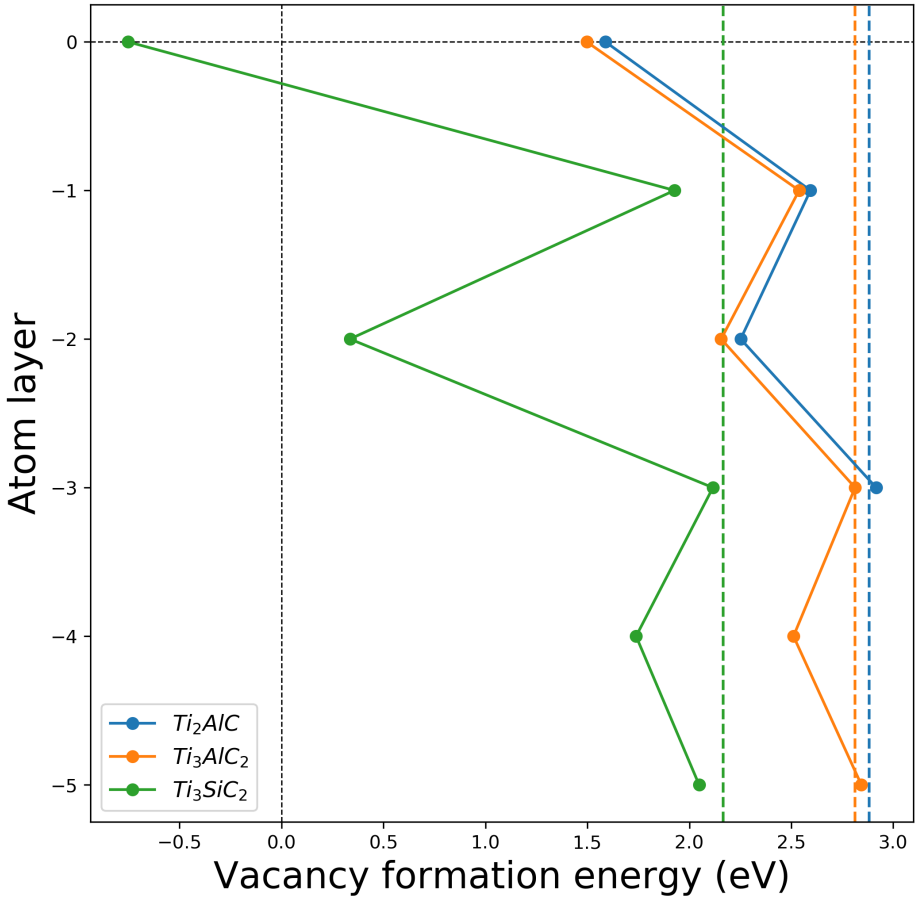

FIGURE 5.8: Vacancy formation energy of MAX phase surfaces. The vacancy formation energy is plotted against the number of layers beneath the surface where the vacancy occurs. The bulk vacancy formation energies are plotted as dashed lines.

Looking at how the vacancy formation energy changes as the vacancy layer moves down from the surface of the three MAX phases, it can be seen that the energy required to form a vacancy increases as the vacancy layer moves further away from the surface. In fact, the formation energy at the bottom of each surface system is close to that calculated in the bulk systems. For Ti_2AlC, the vacancy formation energy of the lowest layer is 2.916 eV, compared to 2.882 eV in the bulk, while for Ti_3AlC_2, it is 2.844 eV compared to 2.812 eV, and finally for Ti_3SiC_2, it is 2.048 eV compared to 2.167 eV in the bulk. This indicates that, in terms of vacancy formation, only one slab is required before bulk-like conditions are experienced.

The surfaces with Ti at the surface tend to show a higher vacancy formation energy than the surfaces with Al, Si, or C at the surface. This might indicate that the formation of a vacancy

when a complete Ti octahedral prism, with C in the centre, is present at the surface makes the vacancy formation of Al or Si require more energy.

In this section, the difference between the d-band centres between the vacancy and non-vacancy surface systems will be analysed, then the difference in Bader charges will be discussed, and finally the resistivities of the surfaces will be compared to each other and to the bulk systems.

5.4.1. Density of States

The mean change in d-band centre between surfaces with and without an A group vacancy were calculated and are shown in Figure 5.9. Each surface is shown for each MAX phase and the atomic layers have been aligned so that the layer with the vacancy is in the same position, represented by a black dashed horizontal line. The mean of the d-band centre was calculated over all the atoms in the layer.

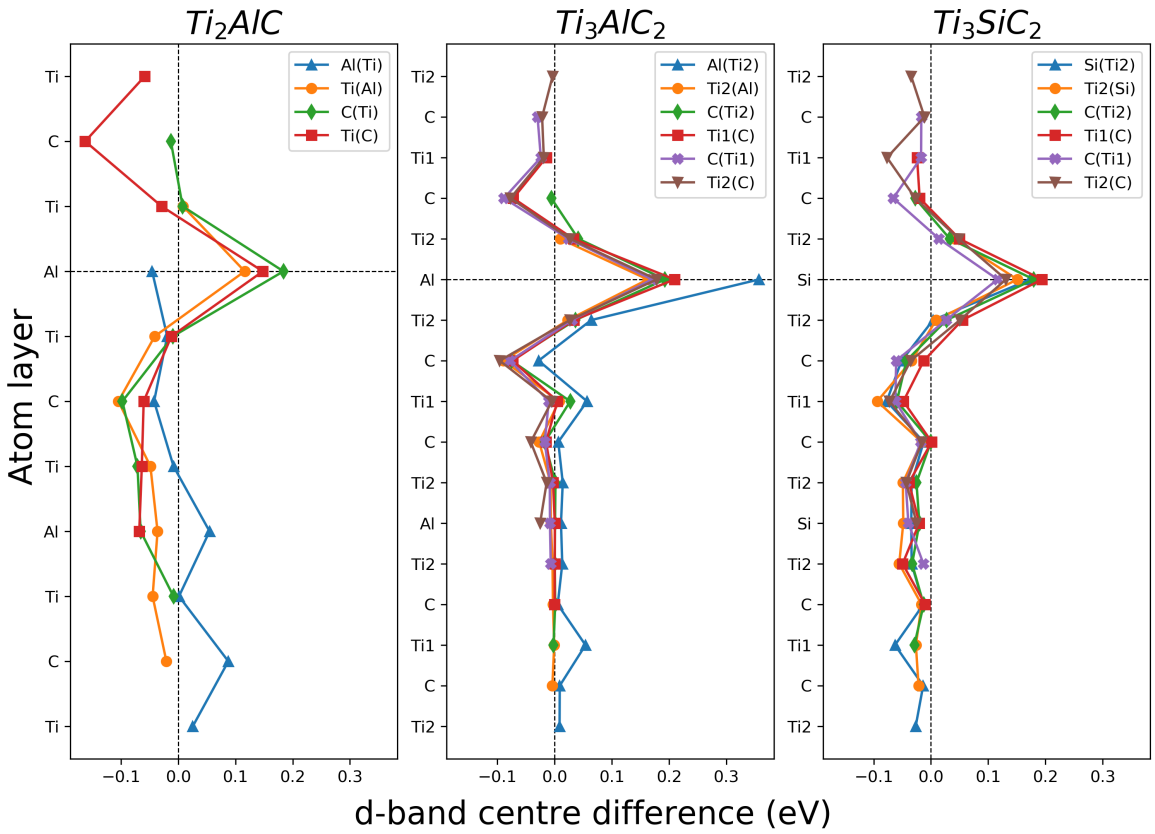

FIGURE 5.9: Difference between the d-band centre of each atomic layer with and without an A group vacancy present for the surfaces of Ti_2AlC, Ti_3AlC_2, and Ti_3SiC_2

Looking at Figure 5.9, it is evident that the d-band centre of the layer with the vacancy shifts to higher energy compared to without the vacancy. It also can be seen that for Ti_2AlC and Ti_3SiC_2 the d-band centre for the atoms in the other layers shifts to a lower energy most of the time, while for Ti_3AlC_2, the d-band centre for other layers does not show a large difference to the system without the vacancy.

The d-band centre for the Al layer in the Al(Ti) surface of Ti_2AlC is no different to the surface without the vacancy, but for the equivalent surface in Ti_3AlC_2, Al(Ti2), the d-band centre shifts by more than 0.4 eV, the largest shift of any layer.

Comparing the d-band centres of the different surfaces of Ti_3AlC_2 and Ti_3SiC_2, it can be seen that the d-band centre shifts less as the vacancy layer moves to lower layers. The largest change occurs when the d-band centre is at the surface, while the smallest change in the Al/Si vacancy layer is for the C(Ti1) layer, when the vacancy is five layers beneath the surface of the slab. This is closely followed by Ti2(C), the sixth layer vacancy.

5.4.2. Charge Density and Bader Charge Analysis

The charge density and Bader charge for the surface systems with and without the vacancy were calculated. The charge density of the unit cell with the vacancy was subtracted from the unit cell without the vacancy. The difference between the charge density shows where the A group atom was removed, along with some changes to surrounding atoms. Only one of the surfaces is shown in Figure 5.10, namely the Ti(C) surface of Ti_2AlC, where changes to the surrounding atoms can be clearly seen.

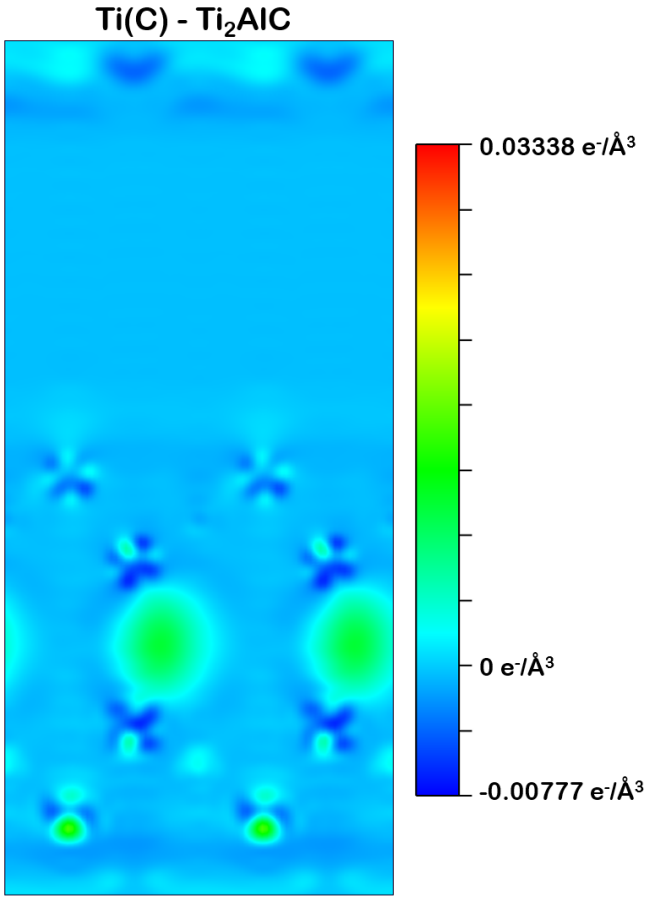

FIGURE 5.10: Charge density difference through a (1 1 0) plane between the surface with and without an Al vacancy for the Ti(C) surface of Ti_2AlC.

It is evident that in the position where the Al vacancy occurs there is a positive difference in the charge density, showing where charge has been removed. The change in the orbitals around the Ti atoms can also be seen. Dark blue shows a negative charge, indicating that the system with the vacancy has a higher charge density in that area. The different lobes show the orbitals of the Ti atoms.

Again, since the Bader charge provides quantitative information about the charge density, the difference between the Bader charge of the surfaces with and without the A group vacancy was calculated for each surface of each MAX phase. The mean Bader charge of the atoms in each layer were calculated and the Bader charge of the surface with the vacancy subtracted from the surface without the vacancy, with the results shown in Figure 5.11. The vacancy layer of each surface has been aligned so that the same atoms can be compared to each other.

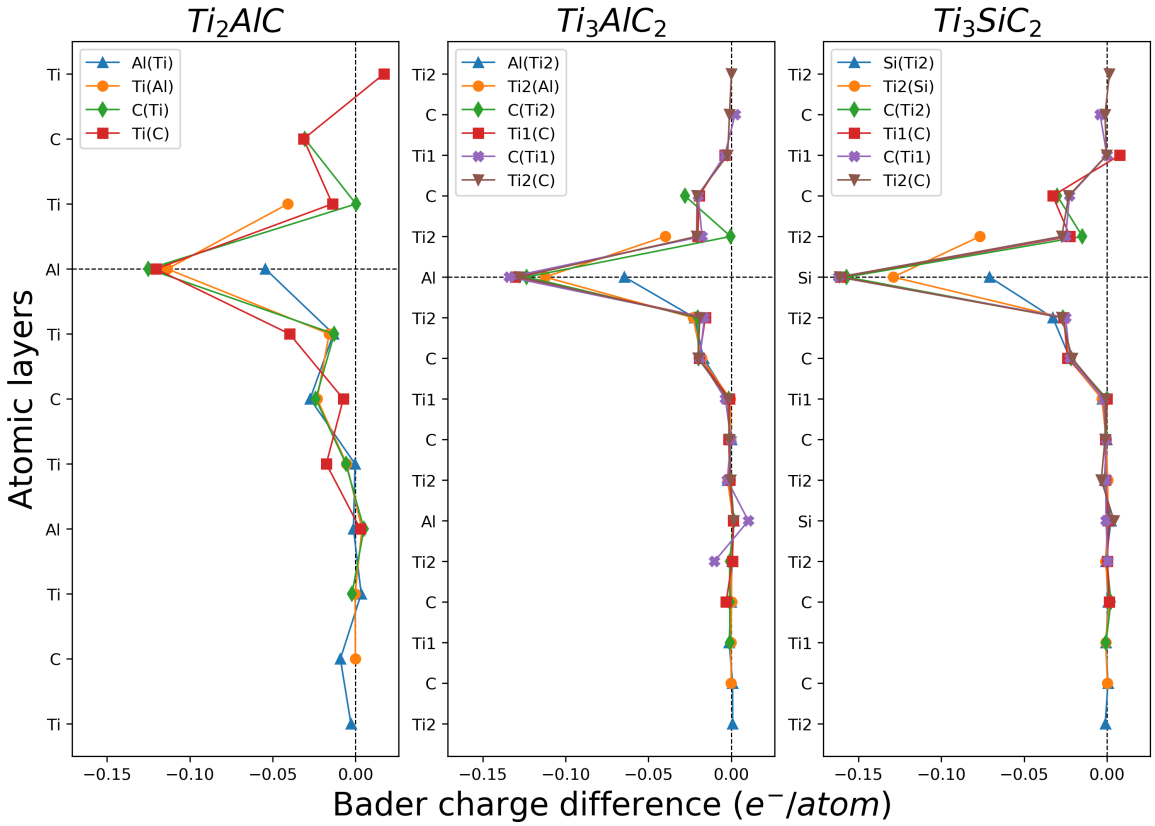

FIGURE 5.11: Bader charge difference between surfaces of Ti_2AlC, Ti_3AlC_2, and Ti_3SiC_2 with an A group vacancy and without it

It can be seen that the Bader charge in the layer with the A group vacancy decreases, i.e. a more negative Bader charge. The remaining Al/Si atoms therefore draw more electrons away from the surrounding atoms than without a vacancy. However, the change in Bader charge is larger when the vacancy layer is not at the surface. The change in Bader charge fluctuates down the rest of the surface slab between the Ti and other atoms, where the change for the Ti atoms is generally lower than for the C and Al layers.

The surfaces with Al/Si in the surface layer have about half the Bader charge difference than slabs with the vacancy layer below the surface. This is probably because the Al/Si atoms below the surface have Ti atoms above and below them, and can therefore draw electrons from both layers. The slabs with the vacancy layer in the surface only have one layer of Ti atoms from which to draw electrons, therefore show half the change in Bader charge.

For most surfaces, the vacancy in the A group layer only affects the atoms two layers above and below it. This is consistent with the results from the bulk calculation, where only two layers above and below the vacancy layer were affected (see Figure 4.4). There are some surfaces with exceptions to this, such as C(Ti) in Ti_2AlC and C(Ti1) in Ti_3AlC_2. For C(Ti) in Ti_2AlC, three layers above and beneath the vacancy layer are affected by the formation of a vacancy. This could be because the layer with the vacancy is near the middle of the slab, and since unit cells two slabs thick were used and the bottom slab was fixed, the slab might not be thick enough for that surface. For the C(Ti1) surface of Ti_3AlC_2 there is a deviation from zero in the bottom two layers of the slab. The bottom two layers of the slab comprise of Ti2 atoms in the bottom surface and Al atoms in the subsurface. It could be that the unrelaxed bond lengths of Ti2-Al required a rearrangement of Bader charge to be stabilised.

5.4.3. Boltzmann Transport Properties

The Boltzmann transport properties were calculated for each surface slab of the MAX phases both with and without a vacancy present in order to determine how the electrical conductivity of the system with a surface would affect the overall electrical conductivity. The same parameters that were used for the bulk were used for the surface slabs. The resistivity at the chemical potential nearest to the Fermi level is shown in Figure 5.12 along with the bulk resistivities. Since the Fermi level is where the highest occupied orbital is, this is the most meaningful place where electrons relate to conductivity. Owing to `BoltzTraP2` calculating the resistivities at different chemical potentials, a single chemical potential needed to be chosen to compare resistivity against temperature. Additionally, the resistivity of each surface slab at 300 K is shown in Table 5.2.

Looking at Figure 5.12, it can be seen that there is a variation between the resistivities of different surface slabs with the same MAX phase. For Ti_2AlC, the resistivity of the slab with Ti(C) at the surface is the closest to the bulk resistivity, while Ti(Al) and C(Ti) show a lower resistivity than the bulk. However, none of the surface slabs with vacancies present match the trend of the bulk resistivity with an Al vacancy. All the surface slabs, except Al(Ti), show an increased resistivity with a vacancy present. The Al(Ti) surface slab shows a decreased resistivity with an Al vacancy compared to the slabs without the vacancy. Overall, there is fairly good agreement between the resistivities shown by the surface slabs compared to the bulk resistivity.

For Ti_3AlC_2, the trend between the surface slabs and the bulk resistivity is not as good. The Ti1(C) and C(Ti2) surface slabs show the same resistivity as the bulk up until 200 K, from which they deviate and show a higher resistivity. All the other surface slabs show a higher

TABLE 5.2: The resistivity of each surface slab of the three MAX phases at 300 K with and without an A group vacancy

MAX phase	Surface	Resistivity (μΩ m)	Resistivity with vacancy (μΩ m)
Ti_2AlC	Bulk	0.460	0.620
	Al(Ti)	0.557	0.390
	Ti(Al)	0.329	0.854
	C(Ti)	0.338	1.012
	Ti(C)	0.489	0.710
Ti_3AlC_2	Bulk	0.370	0.586
	Al(Ti2)	0.740	0.629
	Ti2(Al)	1.369	1.187
	C(Ti2)	0.412	0.630
	Ti1(C)	0.427	0.604
	C(Ti1)	1.373	0.768
	Ti2(C)	0.740	0.825
Ti_3SiC_2	Bulk	0.268	0.392
	Si(Ti2)	0.981	1.177
	Ti2(Si)	1.008	1.104
	C(Ti2)	1.130	1.829
	Ti1(C)	1.123	2.120
	C(Ti1)	0.624	1.594
	Ti2(C)	0.987	0.700

resistivity than the bulk, with the resistivities of Ti2(C) and Al(Ti2) being nearly identical, while that of C(Ti1) and Ti2(Al) is three times that of the bulk. Half of the surface slabs with a vacancy present show the same trend as the bulk, with the resistivity being higher with a vacancy. These surface slabs are C(Ti2), Ti1(C), and Ti2(C). The other three slabs, Al(Ti2), Ti2(Al), and C(Ti1), have a lower resistivity with an Al vacancy.

The agreement between the surface slabs and the bulk of Ti_3SiC_2 is the worst of the three MAX phases. The bulk resistivity is much lower than any of the surface slabs. The resistivity of C(Ti1) is the closest to that of the bulk, however, it is still more than double that of the bulk. The resistivities of Si(Ti2), Ti2(Si), and Ti2(C) are very close to each other, while that of C(Ti2) and Ti1(C) are the highest of the surface slabs. The resistivity of Ti2(C) with a Si vacancy is lower than the resistivity without a vacancy, which is opposite to the trend observed from the bulk. The other surface slabs all show an increase in resistivity with a Si vacancy compared to without one. The resistivities of C(Ti1), C(Ti2), and Ti1(C) with a vacancy are between four and five and a half times larger than the bulk resistivity.

Combining the observations of Figure 5.9 and Figure 5.12, a trend emerges between the Ti d-band centre and the resistivity of the MAX phases when an A group vacancy is formed. It was seen in Figure 4.1 that the Ti d orbital contributes towards the DOS at the Fermi level more than any other orbitals from the MAX phase elements. This suggests that the Ti d orbital is primarily responsible for the electrical conductivity. When an Al/Si vacancy is formed, the Ti d-band centre tends to shift to lower energy, for both the bulk unit cells and

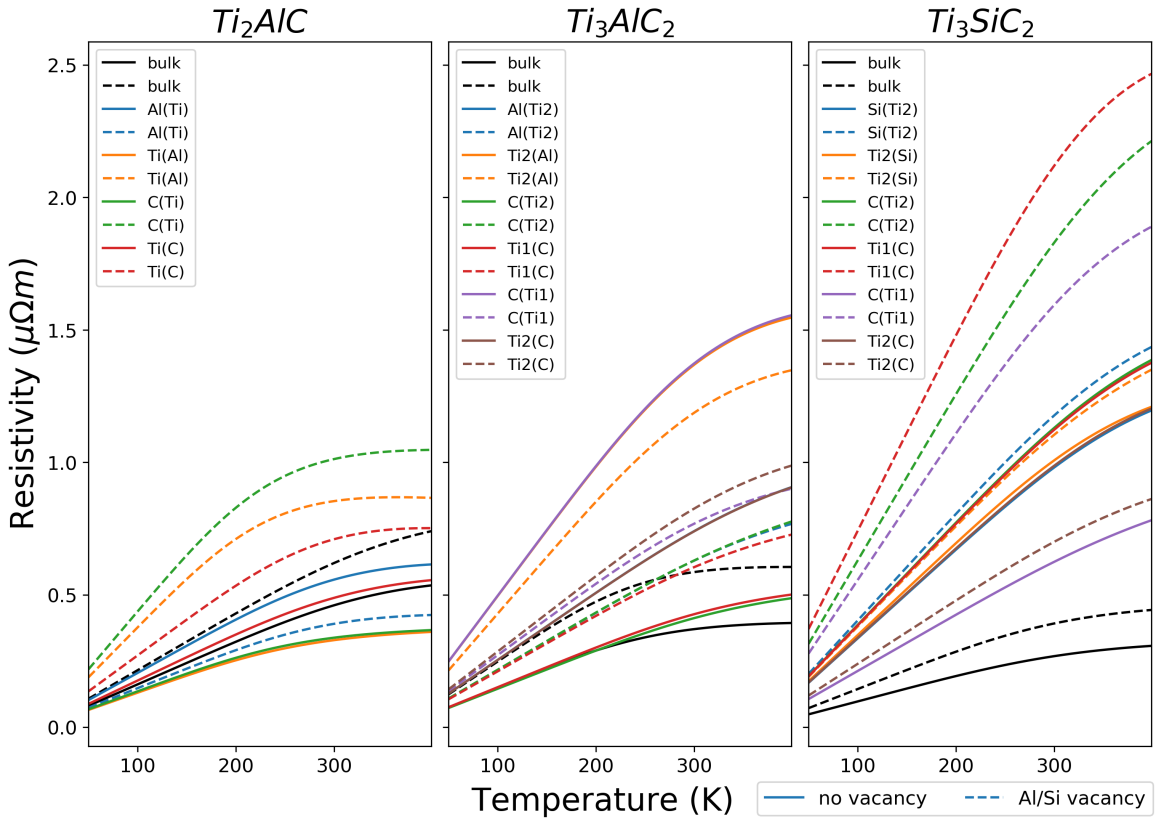

FIGURE 5.12: Resistivity of MAX phase surfaces against temperature with and without an Al/Si vacancy. Resistivities are taken at the chemical potential closest to zero.

the surface unit cells. A shift to lower energy implies that the electrons are more strongly bound by the nucleus of the atom. This would increase the energy required for electrons to move from the valence band to the conduction band. Electrons are required to be in the conduction band for a material to be electrically conductive. Therefore, a reduction in DOS at the Fermi level, signified by a shift of the d-band centre to lower energy, would reduce the electrical conductivity, thereby increasing the resistivity of a material. This would explain why the resistivity increases when an Al/Si vacancy is formed.

6. Discussion

6.1. Surface Stability

Since different (0 0 0 1) surfaces can be cleaved from the MAX phases, the surface that would preferentially be found on a MAX phase particle is of great interest. However, without being able to directly determine the surface energy of each surface, other metrics need to be used to determine the most stable surface of each MAX phase.

For Ti_2AlC, it was seen that the cleavage energy of Al(Ti) and Ti(C) surfaces was lower than that of C(Ti) and Ti(Al), indicating that Al(Ti) and Ti(C) are the more stable of the four surfaces. From the analysis of the DOS of Al(Ti) and C(Ti), it was seen that the change in DOS affects deeper layers for C(Ti) than it does for Al(Ti), suggesting that Al(Ti) is more stable than C(Ti). It was described through the change in Bader charge compared to the bulk atoms that in Al(Ti) the Al layer changes but the subsurface Ti layer does not change much. However, with Ti(C), both the surface Ti layer and the subsurface C layer show a change in Bader charge (Figure 5.7). To better analyse this, the cumulative change in the Bader charge over the first three layers of each surface slab was calculated and is shown in Table 6.1. Although the Bader charge in the first layer is higher for Al(Ti) than for Ti(C), it can be seen that over the first three layers, the absolute value of the cumulative change in Bader charge is less for Al(Ti) than for Ti(C), suggesting that the first three layers of Al(Ti) are not as affected by the cleaving of a surface as those in Ti(C). It was described in Section 5.3.3 how the positive change for surface with Al, Si, and C in the surface layer signify the atom becoming more positive, and for surfaces with Ti in the surface, the negative change means that Ti becomes more negative. In both cases, the atoms are returning closer to their elemental number of valence electrons, therefore the absolute value of the change in Bader charge is compared.

It can also be seen from Figure 5.7 that both the C(Ti) and Ti(Al) surfaces are affected by the surface much more than the Al(Ti) and Ti(C) surfaces. This is because the Ti-C cage is broken, causing the Ti and C atoms to experience completely different environments. The breaking of the Ti-C structure would therefore make C(Ti) and Ti(Al) less stable than Al(Ti) and Ti(C). It is unsurprising that Ti(Al) and C(Ti) both show instability, since they only differ by the C surface layer. In other words, removing the C surface layer in C(Ti) produces Ti(Al). The breaking of the Ti cage with C in the middle seems to destabilise those surface layers.

Should Ti(C) prove to be more stable than Al(Ti) under fuel cell conditions, there will not be excessive reconstruction should Al(Ti) be at the surface since removing the surface Al layer creates a Ti(C) surface. Both of these layers maintain the Ti-C cage intact at or near the surface, which seems to provide better stability. Additionally, the Ti(C) surface is closer

to the electrical resistivity of the bulk than Al(Ti) (Figure 5.12), therefore forming Ti(C) will not negatively impact the electrical conductivity.

TABLE 6.1: The cumulative Bader charge change over the first three surface layers

MAX phase	Surface	Cumulative Bader charge change		
		1 layer	2 layers	3 layers
Ti_2AlC	Al(Ti)	0.370	0.367	0.329
	Ti(C)	-0.186	-0.358	-0.363
	C(Ti)	0.639	0.728	0.926
	Ti(Al)	-0.969	-0.915	-0.908
Ti_3AlC_2	Al(Ti2)	0.381	0.389	0.352
	Ti2(C)	-0.164	-0.325	-0.349
	C(Ti1)	0.801	0.769	0.855
	Ti2(Al)	-0.941	-0.920	-0.895
	C(Ti2)	0.538	0.598	0.815
	Ti1(C)	-0.504	-0.770	-0.799
Ti_3SiC_2	Si(Ti2)	0.457	0.436	0.435
	Ti2(C)	-0.301	-0.423	-0.400
	C(Ti1)	0.869	0.874	0.977
	Ti2(Si)	-0.887	-0.985	-0.997
	C(Ti2)	0.654	0.668	0.766
	Ti1(C)	-0.483	-0.706	-0.762

For Ti_3AlC_2, the cleavage energy of Al(Ti2) and Ti2(C) were the lowest of the three surface pairs investigated. This is the same bond that is broken that produces the Al(Ti) and Ti(C) surfaces in Ti_2AlC, therefore the similarity is not unexpected. The breaking of the Ti2-C bond to produce C(Ti1) and Ti2(Al) requires the most energy, yielding the highest cleavage energy. This is not unexpected as was seen in Ti_2AlC, where breaking the Ti-C cage was energetically unfavourable. However, breaking the Ti1-C bond in Ti_3AlC_2, creating C(Ti2) and Ti1(C) resulted in a lower cleavage energy than C(Ti1) and Ti1(C). This also breaks the Ti-C cage, but leaves one complete Ti-C cage intact in the Ti1(C) surface, which seems to provide increased stability.

From the DOS of Ti_3AlC_2 it was seen that C(Ti1) showed a change in spin polarisation, which coupled with the high cleavage energy could be a sign of instability. Additionally, the flattening of the charge density sphere around the surface C atoms shows how much the environment changes. In keeping with the low cleavage energy of Al(Ti2), the change in DOS did not extend beyond the second layer in the slab, while for C(Ti2) there was a change in the shape of the DOS of the third layer consisting of Al atoms.

Then, looking at Table 6.1, it can be seen that the low cleavage energy of Al(Ti2) and Ti2(C) corresponds with a low change in Bader charge. Over three layers the absolute cumulative change in Bader charge is almost identical for Al(Ti2) as for Ti2(C), showing that these surfaces are very similar in how the change in environment affects the surface atoms. This

follows what was seen in Ti_2AlC with Al(Ti) and Ti(C) as well. Both Al(Ti2) and Ti2(C) keep the whole Ti cage intact near the surface, which explains the low cleavage energy.

The surface with the largest cumulative change in Bader charge is the Ti2(Al) surface. This is similar to the Ti(Al) surface of Ti_2AlC, which also showed a large change. Closely behind this surface in terms of Bader charge change is the C(Ti1) surface. These surfaces break the Ti cage, resulting in a high cleavage energy and a large change in Bader charge of the surface atoms. Breaking the Ti cage seems to cause the biggest change in Bader charge at the surface along with higher cleavage energies.

The surfaces of Ti_3SiC_2 show similar trends as those of Ti_3AlC_2. The surface pair with the lowest cleavage energy was Si(Ti2) and Ti2(C), again showing that the Ti2-Si bond (Ti2-A group atom) is the bond that is most easily broken. The cleavage energy generated through the breaking of this bond is higher than for Ti_3AlC_2, confirming that the Ti2-Si bond is stronger than the Ti2-Al bond. In agreement with Ti_3AlC_2, the surfaces with the highest cleavage energy are C(Ti1) and Ti2(Si), with the same cleavage energy for both 312 MAX phases. In-between these two broken bonds, the cleavage energy of C(Ti2) and Ti1(C) enters, showing the same trend as in Ti_3AlC_2. However, the cleavage energy from breaking the Ti1-C bond in Ti_3SiC_2 is higher than in Ti_3AlC_2, suggesting that this bond is stronger in Ti_3SiC_2, despite the fact that the bond length is the same in the bulk systems. This is discussed more below.

The DOS of Ti_3SiC_2 has the same trend as in Ti_3AlC_2. The DOS changes mostly in the first two layers and only slightly in the third layer in the Si(Ti2) surface. Unlike in Ti_3AlC_2, a spin polarisation change is not observed in the C(Ti1) surface. A large peak in the C surface layer is observed at the Fermi level that is not present in the C layers further away from the surface. The change in DOS extends far down the slab to the fifth layer, showing that breaking the Ti cage the C(Ti1) surface causes changes deep into the surface, no matter which A group atom is part of the MAX phase. Similarly to Ti_3AlC_2, there is a change in the DOS shape down to the third layer of the C(Ti2) surface, down to the Si layer closest to the surface.

Coming back to Table 6.1, the absolute cumulative change in Bader charge trend follows that of Ti_3AlC_2 well, with the surface with the smallest change being Ti2(C), closely followed by Si(Ti2). The Bader charge changes for the Ti_3SiC_2 surfaces are generally higher than the equivalent surfaces in Ti_3AlC_2, which is unsurprising given that Si in the bulk has a lower Bader charge than Al in the bulk, therefore any change in its environment is going to affect it all the more. Again, the surfaces with the highest cleavage energy, coupled with the breaking of the Ti cage, show the largest change in Bader charge, the same surfaces as in Ti_3AlC_2: C(Ti1) and Ti2(Si). These two surfaces have a similar cumulative change in Bader charge, however both are larger than the same surfaces in Ti_3AlC_2.

Returning to the cleavage energy of C(Ti2) of Ti_3SiC_2 being higher than for Ti_3AlC_2, it can be seen that the change in Bader charge is higher for the surface C layer in Ti_3SiC_2 than in Ti_3AlC_2. This could be because of the difference between the change in Bader charge of Al

and Si in the third layer from the surface. The change in Al is 0.216 e^-, while the change in Si is 0.098 e^-, indicating that Al experiences a greater Bader charge change than Si. This larger change in Al could help cause the Bader charge change of the C atom at the surface to be smaller. This smaller change could aid in reducing the cleavage energy of C(Ti2) in Ti_3AlC_2. This can be seen in Figure 5.7 with the C(Ti2) surface line. The change in C Bader charge at the surface in Ti_3AlC_2 is smaller than the change in Ti_3SiC_2, while the change in Al in the third layer is larger than the change of Si in the same layer. It is known that Si is more electronegative than Al, therefore Si would be less "willing" to give up extra electrons that it has gained from the surrounding Ti atoms. Therefore, the smaller change at the surface when Al is present in the slab may be the reason that C(Ti2) of Ti_3AlC_2 has a lower cleavage energy than C(Ti2) of Ti_3SiC_2.

Looking at the effect of introducing an A group vacancy into the MAX phase surfaces, it was seen in Figure 5.11 that the Bader charge decreases for the Al/Si layer with the vacancy present compared to the same surface without the vacancy. For the case where the Al/Si vacancy is at the surface, the change in Bader charge is roughly half the change when the Al/Si layer is not at the surface. This would be because the remaining Al/Si atoms at the surface can only draw electrons from one Ti layer instead of from two Ti layers. However, the negative change in Bader charge of the Al/Si atoms indicates that the remaining Al/Si atoms are able to draw more electrons and so their Bader charge is closer to the bulk Al/Si Bader charge. This could change the stability of Al(Ti), Al(Ti2), and Si(Ti2) surfaces, but the change in Bader charge cannot be used to predict the change in stability directly. The other low cleavage energy surfaces – Ti(C), Ti2(C), and Ti2(C) – where the Al/Si vacancy layer is at the bottom of the first slab also show the same negative change in Bader charge. However, the Bader charge of the top three layers in the 312 MAX phases is not affected by the vacancy, indicating that the effect of the vacancy does not propagate through the whole Ti cage.

The top layers of Ti(C) in Ti_2AlC show some change in Bader charge, since they are closer to the vacancy layer. The surface Ti atoms show an increase in Bader charge, while the subsurface C atoms and third layer Ti atoms show a decrease in Bader charge. This brings the Ti surface atoms closer to their bulk Bader charge, while the subsurface C draws even more electrons than in its bulk state in becoming more negative, and the Ti in the third layer loses electrons to the Al layer beneath it. However, the d-band centre of all three top layer shifts to lower energy (Figure 5.9), indicating that the surface might retain its stability.

While the Bader charge of the Al atoms at the surface of Al(Ti2) in Ti_3AlC_2 becomes more negative when an Al vacancy is formed, the d-band centre shifts to higher energy, indicating that the Al layer might be slightly less strongly bonded to the subsurface Ti2 atoms with an Al surface vacancy. This would make sense, given the propensity of Al to migrate out and form Al_2O_3 in experimental results (Barsoum, 2013: ch. 7). The other low cleavage energy surface of Ti_3AlC_2, Ti2(C), shows a decrease in Bader charge in the Al vacancy layer and the surrounding two layers, but not in the surface three layers (Ti2-C-Ti1), i.e. the atoms on the other side of the Ti cage. Additionally, the d-band centre of these three surface layers shifts

to a slightly lower energy, indicating a possible increase in bond strength of the surface Ti-C cage. The d-band centre shift of the Al vacancy layer seems to be mitigated by the C layers on the other side of the adjacent Ti2 layers, both above and below.

The same trends observed for Al(Ti2) and Ti2(C) in Ti_3AlC_2 are observed in Si(Ti2) and Ti2(C) of Ti_3SiC_2. The Bader charge of Si in the surface layer decreases when a Si vacancy is formed, while the d-band centre increases slightly. The fact that the d-band centre of Si in Si(Ti2) does not change as much as that of Al in Al(Ti2) could indicate that the Si(Ti2) surface is not as affected as Al(Ti2) when vacancies are present. For the Ti2(C) surface, the Bader charge change with a Si vacancy is the same as the effect observed with a Al vacancy. However, the d-band centres of the Ti2(C) Ti_3SiC_2 slab shift to lower energy compared to the same layers in Ti2(C) of Ti_3AlC_2.

6.2. Electrical Conductivity

One of the primary objectives of this study was to determine whether the MAX phases investigated were electrically conductive. By using Boltzmann transport theory the electrical conductivity of each MAX phase was able to be calculated. At 300 K the bulk resistivity of the MAX phases was calculated to be 0.460 µΩ m for Ti_2AlC, 0.370 µΩ m for Ti_3AlC_2, and 0.268 µΩ m for Ti_3SiC_2. This equates to electrical conductivity values of $2.17 \times 10^4\,S\,cm^{-1}$ for Ti_2AlC, $2.70 \times 10^4\,S\,cm^{-1}$ for Ti_3AlC_2, and $3.73 \times 10^4\,S\,cm^{-1}$ for Ti_3SiC_2. This shows that MAX phases are definitely electrically conductive.

Comparing the MAX phases against other catalyst support materials used in PEMFCs, we see that MAX phases show good potential in terms of electrical conductivity. Pantea et al. (2001) report a measurement for carbon, traditionally used as the catalyst support material, as $4.0\,S\,cm^{-1}$. Carbon has low oxidation resistance, hence the need for materials that are more oxidation resistant. In the ceramics class, Pawbake et al. (2016) investigated tungsten carbide, WC, and report an electrical conductivity of $1.26 \times 10^3\,S\,cm^{-1}$, three orders of magnitude higher than that of carbon black. WC shows good oxidation resistance. However, Sharma & Pollet (2012) claim that WC is unstable above 0.8 V, and therefore is not a viable alternative.

The constituent elements of the MAX phases are not electrically conductive in some other compounds and it seems that the mixture of the Ti-C cages interleaved with either Al or Si alters the electronic structure enough that the MAX phases become electrically conductive. Kim et al. (2015a) synthesised SiC and report an electrical conductivity of $2.0 \times 10^{-10}\,S\,cm^{-1}$. Hollander (1961) reports an electrical conductivity of $5000\,S\,cm^{-1}$ (200 µΩ cm) for single crystal TiC in the [100] direction, while Fan et al. (2010) show that pure Al_2O_3 is an insulator, with an electrical conductivity of $1 \times 10^{-15}\,S\,cm^{-1}$. In terms of SiO_2, Srivastava (1985) reports that it is an insulator. Therefore, the unique structure of the MAX phases creates the electrical conductivity, not necessarily the elements involved.

Looking above at the current and alternative catalyst support materials, it can be seen that all three MAX phases should be able to outperform all the mentioned materials in terms of electrical conductivity. This satisfies the electrical conductivity requirement of Sharma & Pollet (2012: 97).

A crucial factor to consider for the MAX phases is how the electrical conductivity changes when oxidation occurs. It is known that the Al/Si atoms will preferentially migrate out of the lattice to form Al_2O_3 or SiO_2 layers on the surface of particles (Barsoum, 2013). Hence, Al/Si vacancies were investigated. It was shown in Figure 4.5 that the electrical resistivity of all three MAX phases increased when vacancies were introduced. This has the effect of decreasing the electrical conductivity. However, the resistivity did not decrease by any orders of magnitude, and should therefore they will still be good electrical conductors should vacancies form. Given that the inclusion of Al_2O_3 or SiO_2 layers on top of the MAX phase surfaces was not modelled, it is not possible to quantify a realistic change in electrical conductivity. However, the formation of Al_2O_3 or SiO_2 scale is sure to reduce the electrical conductivity.

It is possible that the formation of Al_2O_3 or SiO_2 on the surface of a MAX phase catalyst particle might not affect the performance of the catalyst overall, if the electrical conductivity of the Pt catalyst nanoparticles and the catalyst-support interaction are not affected. The electron flow in the catalyst would be through the Pt particle into the MAX phase, therefore the formation of Al_2O_3 or SiO_2 might not affect this, but this is only speculation.

The resistivities of the different surfaces vary from the bulk resistivity. Some surfaces follow the trend of increased resistivity with vacancy formation, while some show a decreased resistivity when vacancies are introduced. Among these surfaces that show a decreased resistivity with an A group vacancy are Al(Ti) of Ti_2AlC and Al(Ti2) of Ti_3AlC_2; however, Si(Ti2) increases in resistivity when a Si vacancy is introduced at the surface. This could be because the d-band centre of the half of the Ti atoms in Al(Ti) and all the Ti atoms in Al(Ti2) shifts to higher energy, while the Ti atoms in Si(Ti2) shift to lower energy.

6.3. Oxidation Resistance

One of the other primary objectives of this study was to determine the oxidation resistance of the MAX phases. They can be very electrically conductive, but if they do not withstand the low pH conditions within a PEMFC, they will not be better than the currently used carbon black catalyst support material. There is not a straightforward method to measure the oxidation resistance of a material using DFT. To gain an understanding of the oxidation resistance therefore, the vacancy formation energy of an A group element was investigated. It is known that the A group atom is the most easily removed from the unit cell structure of the MAX phase of the three elements (Barsoum, 2013), therefore during oxidation this will be the element that will preferentially migrate out of the structure.

A single vacancy was formed in a 2 x 2 x 2 supercell of the bulk unit cell. The vacancy formation energies were reported in Table 4.3 and were compared against literature values in Table 4.4. It was seen that the vacancy formation energy of Si in Ti_3SiC_2 was the lowest of the three MAX phases, while that of Ti_2AlC and Ti_3AlC_2 are very close. This is interesting because the Bader charge of Si in the bulk structure is more negative than Al in both Al-containing MAX phases. One would therefore expect that the vacancy formation of Si be higher than for Al. Looking at the energy values per atom of bulk Al and bulk Si, -3.745 eV and -5.423 eV respectively, it can be seen that bulk Si has a lower energy than bulk Al. It could be that Si in its diamond cubic structure is more stable than Al in its fcc structure, hence forms a vacancy more easily in the bulk structure.

Oxidation of a material occurs at the surface of the material. It was already established which (0 0 0 1) surfaces of the MAX phase are likely to be the most stable. The vacancy formation energy of the bulk MAX phases showed that a Si vacancy is the most energetically favourable out of the A group vacancies. However, this does not give an indication as to the effect of a vacancy in the surface layers. The vacancy formation energy of an A group atom was then determined for the different surfaces for each MAX phase. These are shown in Figure 5.8. The vacancy formation energy is plotted against the number of layers beneath the surface where the A group atom layer occurs, starting with the A group at the surface. The bulk vacancy formation energy is plotted as a vertical line for reference.

It can be seen that the vacancy formation energy of an A group atom at the surface is lower than in the bulk systems. It therefore requires less energy to form a vacancy near the surface, aided by the fact that atoms near the surface are able to undergo relaxation and so re-minimise the energy of the system. However, as the vacancy layer moves further away from the surface, more and more surrounding atoms are affected by the reconstruction, therefore the vacancy formation energy increases. For each MAX phase, the surfaces with Ti on the surface show a much higher vacancy formation energy than the surfaces with Al, Si, or C on the surface. This could again be because of surface reconstruction through relaxation. The C surfaces are able to compress down into the layers below, creating a lower energy system. The same occurrence was also observed in the charge density of the surfaces where the C atoms at the surface flattened and moved closer to the underlying Ti atoms (Figures 5.4, 5.5, and 5.6). Surfaces with Ti on the surface are able to keep their Ti-C cages intact, therefore could be more stable because of the higher vacancy formation energy.

Comparing the vacancy formation energy of Al(Ti) and Al(Ti2) (Figure 5.8), it can be seen that an Al vacancy in Al(Ti2) is slightly lower than for Al(Ti). These two MAX phases show the same trend in vacancy formation energy down the slab, showing that similar characteristics that they share. However, comparing Al(Ti2) and Si(Ti2), it can be seen that forming an Si vacancy in Si(Ti2) is beneficial to the surface as the energy is negative, compared to Al(Ti2) which is positive. This could indicate that the most stable (0 0 0 1) surface in Ti_3SiC_2 is Ti2(C).

Ultimately, the true oxidation resistance cannot be fully determined without modelling

other surfaces, such as the (1 0 0) and (1 1 0) surfaces. These surfaces could prove to be more stable than the (0 0 0 1) surfaces, or they could be very unstable. Additionally, without being able to calculate a Pourbaix diagram, the true electrochemical oxidation resistance cannot be determined. However, these vacancy formation energy calculations can at least tell us that up to 2.882 eV, or 278 kJ mol^{-1}, is required to form a vacancy. This energy requirement is not trivial, therefore the MAX phases should be able to provide some level of electrochemical oxidation resistance. This hope is aided by the fact that they are oxidation resistant in air, forming protective Al_2O_3 or SiO_2 layers (Barsoum et al., 1997; Tallman et al., 2013).

7. Conclusions

7.1. General Conclusions

The focus of this study was to determine using density functional theory the electrical conductivity and oxidation resistance of three MAX phases: Ti_2AlC, Ti_3AlC_2, and Ti_3SiC_2. To do this, the unit cells of the three MAX phases were modelled and optimised using four different functionals. The functional that optimised the lattice parameters and bulk modulus was chosen by comparison to experimental values. The optimised parameters were then used to calculate the density of states, charge density, Bader charge, and electrical resistivity of the bulk unit cells.

The density of states show a continuous band at the Fermi level, indicating that all three MAX phases are electrically conductive. Element and orbital resolved DOS revealed that the primary contributor to the DOS at the Fermi level is the Ti d orbital. It also highlighted the strong bonds formed between Ti and C atoms, while bonds between Ti and Al or Si were weaker. This was confirmed through the Ti-C and Ti-Al/Si bond lengths. Additionally, this showed that the Ti2-Si bond is stronger than the Ti2-Al bond. However, the presence of Al or Si does not make a difference in the Ti-C bond lengths in the 312 MAX phases. The change in stoichiometric ratio from 211 to 312 did have an effect on the Ti-C bond, with the inner Ti1-C bond being longer than the outer Ti2-C bond in Ti_3AlC_2, with the Ti-C bond in Ti_2AlC falling between these two lengths, but closer to the Ti2-C bond length. The charge density revealed that Ti_3SiC_2 has a higher electron density in amongst the atoms compared to both Al containing MAX phases. It was displayed that the Bader charge of Al does not change between Ti_2AlC and Ti_3AlC_2, however the Bader charge of Si in Ti_3SiC_2 is more negative than that of Al in Ti_3AlC_2. The change of stoichiometric ratio affected the Bader charge of Ti and C, with the Bader charge of C increasing from the 211 to the 312 MAX phases. The two inequivalent Ti atoms in the 312 MAX phases possessed different Bader charges, with the inner Ti1 having a more positive charge than the outer Ti2 atom. The difference between Ti1 and Ti2 reduced going from Ti_3AlC_2 to Ti_3SiC_2.

Results derived from the Boltzmann transport properties show that Ti_3SiC_2 has the lowest electrical resistivity, and therefore the highest electrical conductivity of the three MAX phases. At 300 K this was estimated to be 0.268 μΩ m using the constant relaxation time approximation. At the same temperature, the resistivities of Ti_2AlC and Ti_3AlC_2 were calculated to be 0.460 μΩ m and 0.370 μΩ m respectively. These values are in good agreement with experimental literature.

An A group element vacancy was then formed in a 2 x 2 x 2 supercell of each MAX phase to investigate the vacancy formation energy. The calculated vacancy formation energy of

Ti_3SiC_2 was the lowest of the three at 2.167 eV, while the values for Ti_2AlC and Ti_3AlC_2 were much more similar, at 2.882 eV and 2.812 eV respectively. The formation of a vacancy caused the d-band and p-band centres of most atomic layers around the vacancy layer to shift to lower energy. By looking at the Bader charge of the atomic layers around the vacancy, it was seen that a vacancy affects the immediate two layers above and below the vacancy predominantly. The electrical resistivity of all three MAX phases were calculated to increase with the formation of an A group vacancy, signifying that the electrical conductivity of the MAX phases will decrease during oxidation of the A group element. This increase in resistivity correlates with the shift in Ti d-band centre to lower energy, binding electrons more strongly at lower energies, increasing the difficulty for them to move from the valence band to the conduction band.

As an electrocatalyst support material, MAX phase particles will have surfaces present. It is therefore desirable to know which surfaces would be present on a particle. Due to the layered nature of MAX phases, multiple (0 0 0 1) surfaces are possible, therefore these were investigated to see which would be more stable. Supercells of 2 x 2 were created from the optimised bulk unit cells from which to cleave surfaces and the number of slabs and the vacuum gap were optimised for each cleaved surface. Cleavage energies were calculated for each surface, revealing that the Al(Ti) and Ti(C) pair of Ti_2AlC, the Al(Ti2) and Ti2(C) pair of Ti_3AlC_2, and the Si(Ti2) and Ti2(C) pair of Ti_3SiC_2 surfaces had the lowest cleavage energies for each MAX phase. This suggests that these surfaces are more stable than the other surfaces. This was confirmed through the DOS of each layer, seeing how far down the creation of the surface affected the DOS compared to the bulk DOS. As expected, the DOS near the surface was altered, but the number of atomic layers beneath the surface where the DOS was different to the bulk DOS varied for different surfaces. The change in Bader charge through the surface slab confirmed the stability of the Al(Ti), Ti(C); Al(Ti2), Ti2(C); and Si(Ti2), Ti2(C) surfaces for Ti_2AlC, Ti_3AlC_2, and Ti_3SiC_2 respectively. Surfaces where the Ti-C octahedral structure was broken showed more instability than surfaces with the Ti-C layers intact, or even partially intact in the case of the 312 MAX phases.

Vacancies of an A group atom were also formed for each surface, showing how the vacancy formation energy changed as the vacancy layer moved further away from the surface. The vacancy formation energy was lowest when the vacancy was at the surface, i.e. in Al(Ti), Al(Ti2), and Si(Ti2). For Si(Ti2) it is favourable for there to be a vacancy at the surface, indicating that the Ti2(C) surface could be more stable than the Si(Ti2) surface for Ti_3SiC_2.

The electrical resistivity of each surface slab was calculated, with most surfaces showing a higher resistivity than the bulk systems. This was also determined for surface slabs with vacancies present, with most surfaces with a vacancy increasing in resistivity. However, some surface slabs showed a decrease in electrical resistivity with an A group vacancy present.

The oxidation resistance of a material is not something quantifiable, therefore no conclusive statements are able to be made about the likelihood of oxidation resistance within a fuel cell environment. However, the strong bonding of the Ti-C layers, coupled with the influence

of the Al/Si layers on the Ti d-band creating electrical conductivity, is positive as a potential electrocatalyst support material.

7.2. Recommendations

There are a few additional calculations that would greatly benefit this research as further work in this study. One of these is the cleaving of different surface planes for the calculation of a Wulff diagram. This would give an idea of the shape of a MAX phase particle.

Another interesting aspect where this research could go is in the determination of a Pourbaix diagram. This would be able to give the stability of the MAX phases and competing compounds across a range of pH values. Other work that could be built on this study is the stability of different surfaces in the presence of surface oxygen or hydroxyl species. This would aid in determining the stability of each surface under more realistic conditions.

8. References

Ali, M. S., Islam, A. K. M. A., Hossain, M. M. & Parvin, F. (2012). Phase stability, elastic, electronic, thermal and optical properties of $Ti_3Al_{1-x}Si_xC_2$ ($0 \leq x \leq 1$): First principle study. *Physica B: Condensed Matter* 407(21), 4221–4228.

Bader, R. F. W. (1985). Atoms in molecules. *Accounts of Chemical Research* 18(1), 9–15.

Bai, Y., He, X., Sun, Y., Zhu, C., Li, M. & Shi, L. (2010). Chemical bonding and elastic properties of Ti_3AC_2 phases (A = Si, Ge, and Sn): A first-principle study. *Solid State Sciences* 12(7), 1220–1225.

Bai, Y., Srikanth, N., Chua, C. K. & Zhou, K. (2017). Density Functional Theory Study of $M_{n+1}AX_n$ Phases: A Review. *Critical Reviews in Solid State and Materials Sciences*, 1–52.

Barsoum, M. W., El-Raghy, T., Rawn, C. J., Porter, W. D., Wang, H., Payzant, E. A. & Hubbard, C. R. (1999). Thermal properties of Ti_3SiC_2. *Journal of Physics and Chemistry of Solids* 60(4), 429–439.

Barsoum, M. W. (2000). The $M_{N+1}AX_N$ phases: A new class of solids. *Progress in Solid State Chemistry* 28(1-4), 201–281.

Barsoum, M. W. (2006). Physical Properties of the MAX Phases. *Encyclopedia of Materials: Science and Technology* 1, 1–11.

Barsoum, M. W. (2013). *MAX Phases*. First Edit. Weinheim, Germany: Wiley-VCH Verlag GmbH & Co. KGaA.

Barsoum, M. W. & El-Raghy, T. (1996). Synthesis and Characterization of a Remarkable Ceramic: Ti_3SiC_2. *Journal of the American Ceramic Society* 79(7), 1953–1956.

Barsoum, M. W. & Radovic, M. (2011). Elastic and Mechanical Properties of the MAX Phases. *Annual Review of Materials Research* 41(1), 195–227.

Barsoum, M. W., El-Raghy, T. & Ogbuji, L. U. J. T. (1997). Oxidation Of Ti_3SiC_2 in Air. *Journal of The Electrochemical Society* 144(7), 2508.

Barsoum, M. W., Tzenov, N., Procopio, A., El-Raghy, T. & Ali, M. (2001). Oxidation of $Ti_{n+1}AlX_n$ (n=1-3 and X=C, N): II. Experimental Results. *Journal of The Electrochemical Society* 148(8), C551.

Bengtsson, L. (1999). Dipole correction for surface supercell calculations. *Physical Review B* 59(19), 12301–12304.

Birch, F. (1947). Finite Elastic Strain of Cubic Crystals. *Physical Review* 71(11), 809–824.

Blöchl, P. E. (1994). Projector augmented-wave method. *Physical Review B* 50(24), 17953–17979.

Boltzmann, L. (1964). *Lectures on Gas Theory.* Translated by Stephen G. Brush. University of California Press.

Born, M. & Oppenheimer, R. (1927). Zur Quantentheorie der Molekeln. *Annalen der Physik* 389(20), 457–484.

Borup, R. et al. (2007). Scientific aspects of polymer electrolyte fuel cell durability and degradation. *Chemical Reviews* 107(10), 3904–3951.

Cabioch, T., Eklund, P., Mauchamp, V., Jaouen, M. & Barsoum, M. W. (2013). Tailoring of the thermal expansion of $Cr_2(Al_x, Ge_{1-x})C$ phases. *Journal of the European Ceramic Society* 33(4), 897–904.

Chadi, D. J. & Cohen, M. L. (1973). Special Points in the Brillouin Zone. *Physical Review B* 8(12), 5747–5753.

Cohen, E. R. et al. (2007). *Quantities, Units and Symbols in Physical Chemistry*. 3rd Editio. Cambridge: IUPAC & RSC Publishing.

Cort, J. W. & Kenji, M. (2005). Advantages of the mean absolute error (MAE) over the root mean square error (RMSE) in assessing average model performance. *Climate Research* 30(1), 79–82.

Dirac, P. A. M. (1929). Quantum Mechanics of Many-Electron Systems. *Proceedings of the Royal Society A: Mathematical, Physical and Engineering Sciences* 123(792), 714–733.

Eichler, A. (2003). *Sampling the Brillouin-zone*. `https://www.vasp.at/vasp-workshop/slides/k-points.pdf`.

Eklund, P., Beckers, M., Jansson, U., Högberg, H. & Hultman, L. (2010). The $M_{n+1}AX_n$ phases: Materials science and thin-film processing. *Thin Solid Films* 518(8), 1851–1878.

Etzkorn, J., Ade, M., Kotzott, D., Kleczek, M. & Hillebrecht, H. (2009). Ti_2GaC, Ti_4GaC_3 and Cr_2GaC —Synthesis, crystal growth and structure analysis of Ga-containing MAX-phases $M_{n+1}GaC_n$ with M=Ti, Cr and n=1, 3. *Journal of Solid State Chemistry* 182(5), 995–1002.

Fan, Y., Wang, L., Li, J., Li, J., Sun, S., Chen, F., Chen, L. & Jiang, W. (2010). Preparation and electrical properties of graphene nanosheet/Al_2O_3 composites. *Carbon* 48(6), 1743–1749.

Gao, H., Benitez, R., Son, W., Arroyave, R. & Radovic, M. (2016). Structural, physical and mechanical properties of $Ti_3(Al_{1-x}Si_x)C_2$ solid solution with x=0–1. *Materials Science and Engineering: A* 676, 197–208.

Greeley, J., Nørskov, J. K. & Mavrikakis, M. (2002). Electronic Structure and Catalysis on Metal Surfaces. *Annual Review of Physical Chemistry* 53(1), 319–348.

Gressman, P. T. & Strain, R. M. (2010). Global classical solutions of the Boltzmann equation with long-range interactions. *Proceedings of the National Academy of Sciences* 107(13), 5744–5749.

Hammer, B. & Nørskov, J. K. (2000). Theoretical surface science and catalysis—calculations and concepts. *Impact of Surface Science on Catalysis*. Vol. 45. Academic Press, 71–129.

Hammer, B., Hansen, L. B. & Nørskov, J. K. (1999). Improved adsorption energetics within density-functional theory using revised Perdew-Burke-Ernzerhof functionals. *Physical Review B - Condensed Matter and Materials Physics* 59(11), 7413–7421.

Henkelman, G., Arnaldsson, A. & Jónsson, H. (2006). A fast and robust algorithm for Bader decomposition of charge density. *Computational Materials Science* 36(3), 354–360.

Hettinger, J. D. et al. (2005). Electrical transport, thermal transport, and elastic properties of M_2AlC (M=Ti, Cr, Nb, and V). *Physical Review B* 72(11), 115120.

Hohenberg, P. & Kohn, W. (1964). Inhomogeneous electron gas. *Physical Review B* 136(3B), B864–B871.

Hollander, L. E. (1961). Electrical Conductivity and Thermoelectric Effect in Single-Crystal TiC. *Journal of Applied Physics* 32(6), 996–997.

Horlait, D., Grasso, S., Chroneos, A. & Lee, W. E. (2016). Attempts to synthesise quaternary MAX phases (Zr, M)$_2$AlC and Zr$_2$(Al, A)C as a way to approach Zr$_2$AlC. *Materials Research Letters* 4(3), 137–144.

Hu, C., Zhang, H., Li, F., Huang, Q. & Bao, Y. (2013). New phases' discovery in MAX family. *International Journal of Refractory Metals and Hard Materials* 36, 300–312.

Hug, G. (2006). Electronic structures of and composition gaps among the ternary carbides Ti$_2$MC. *Physical Review B - Condensed Matter and Materials Physics* 74(18), 1–7.

Ito, M., Setoyama, D., Matsunaga, J., Muta, H., Kurosaki, K., Uno, M. & Yamanaka, S. (2006). Electrical and thermal properties of titanium hydrides. *Journal of Alloys and Compounds* 420(1-2), 25–28.

Ivanovsky, A. L., Novikov, D. L. & Shveikin, G. P. (1995). Electronic Structure of Ti$_3$SiC$_2$. *Mendeleev Communications* 3, 90–91.

Jeitschko, W. & Nowotny, H. (1967). Die Kristallstruktur von Ti$_3$SiC$_2$—ein neuer Komplexcarbid-Typ. *Monatshefte für Chemie-Chemical Monthly* 98(2), 329–337.

Jeitschko, W., Nowotny, H. & Benesovsky, F. (1964). Carbides of formula T$_2$MC. *Journal of the Less Common Metals* 7(2), 133–138.

Jovic, V. D. & Barsoum, M. W. (2004). Corrosion Behavior and Passive Film Characteristics Formed on Ti, Ti$_3$SiC$_2$, and Ti$_4$AlN$_3$ in H$_2$SO$_4$ and HCl. *Journal of The Electrochemical Society* 151(2), B71.

Jovic, V. D., Jovic, B. M., Gupta, S., El-Raghy, T. & Barsoum, M. W. (2006). Corrosion behavior of select MAX phases in NaOH, HCl and H$_2$SO$_4$. *Corrosion Science* 48(12), 4274–4282.

Kim, K. J., Cho, T.-y., Kim, Y.-w., Nishimura, T. & Narimatsu, E. (2015a). Electrical and thermal properties of silicon carbide–boron nitride composites prepared without sintering additives. *Journal of the European Ceramic Society* 35(16), 4423–4429.

Kim, S., Aykol, M. & Wolverton, C. (2015b). Surface phase diagram and stability of (001) and (111) LiM$_2$O$_4$ spinel oxides. *Physical Review B* 92(11), 115411.

Kohn, W. & Sham, L. J. (1965). Self-consistent equations including exchange and correlation effects. *Physical Review* 140(4A).

Krems, M. (2007). *The Boltzmann Transport Equation: Theory and Applications*. `http://www.mattkrems.com/projects/completedprojects/boltzmann.pdf`.

Kresse, G. & Furthmüller, J. (1996). Efficient iterative schemes for ab initio total-energy calculations using a plane-wave basis set. *Physical Review B* 54(16), 11169–11186.

Kresse, G. & Marsman, M. (2012). *VASP the GUIDE*. `http://cms.mpi.univie.ac.at/VASP/` `https://cms.mpi.univie.ac.at/wiki/index.php/The_VASP_Manual`. University of Vienna, 1–188.

Lane, N. J., Naguib, M., Lu, J., Hultman, L. & Barsoum, M. W. (2012). Structure of a new bulk Ti$_5$Al$_2$C$_3$ MAX phase produced by the topotactic transformation of Ti$_2$AlC. *Journal of the European Ceramic Society* 32(12), 3485–3491.

Lapauw, T. et al. (2016a). Synthesis of the new MAX phase Zr$_2$AlC. *Journal of the European Ceramic Society* 36(8), 1847–1853.

Lapauw, T., Halim, J., Lu, J., Cabioc'h, T., Hultman, L., Barsoum, M., Lambrinou, K. & Vleugels, J. (2016b). Synthesis of the novel Zr_3AlC_2 MAX phase. *Journal of the European Ceramic Society* 36(3), 943–947.

Lewars, E. G. (2011). *Computational Chemistry*. 2nd Edition. Dordrecht: Springer Netherlands, 318.

Li, C., Wang, Z. & Wang, C. (2013). Phase stability, mechanical properties and electronic structure of hexagonal and trigonal $Ti_5Al_2C_3$: An ab initio study. *Intermetallics* 33, 105–112.

Li, D., Liang, Y., Liu, X. & Zhou, Y. (2010). Corrosion behavior of Ti_3AlC_2 in NaOH and H_2SO_4. *Journal of the European Ceramic Society* 30(15), 3227–3234.

Liao, T., Wang, J. Y. & Zhou, Y. C. (2008a). Ab initio modeling of the formation and migration of monovacancies in Ti_2AlC. *Scripta Materialia* 59(8), 854–857.

Liao, T., Wang, J. Y. & Zhou, Y. C. (2008b). First-principles investigation of intrinsic defects and (N, O) impurity atom stimulated Al vacancy in Ti_2AlC. *Applied Physics Letters* 93(26), 261911.

Liu, Y., Ji, C., Gu, W., Jorne, J. & Gasteiger, H. A. (2011). Effects of Catalyst Carbon Support on Proton Conduction and Cathode Performance in PEM Fuel Cells. *Journal of The Electrochemical Society* 158(6), B614.

Lu, G. H., Huang, M., Cuma, M. & Liu, F. (2005). Relative stability of Si surfaces: A first-principles study. *Surface Science* 588(1-3), 61–70.

Lv, H., Mu, S., Cheng, N. & Pan, M. (2010). Nano-silicon carbide supported catalysts for PEM fuel cells with high electrochemical stability and improved performance by addition of carbon. *Applied Catalysis B: Environmental* 100(1-2), 190–196.

Madsen, G. K. & Singh, D. J. (2006). BoltzTraP. A code for calculating band-structure dependent quantities. *Computer Physics Communications* 175(1), 67–71.

Madsen, G. K., Carrete, J. & Verstraete, M. J. (2018). BoltzTraP2, a program for interpolating band structures and calculating semi-classical transport coefficients. *Computer Physics Communications* 231, 140–145.

Magnuson, M. & Mattesini, M. (2017). Chemical bonding and electronic-structure in MAX phases as viewed by X-ray spectroscopy and density functional theory. *Thin Solid Films* 621, 108–130.

Makov, G. & Payne, M. C. (1995). Periodic boundary conditions in ab initio calculations. *Physical Review B* 51(7), 4014–4022.

Manoun, B., Zhang, F. X., Saxena, S. K., El-Raghy, T. & Barsoum, M. W. (2006). X-ray high-pressure study of Ti_2AlN and Ti_2AlC. *Journal of Physics and Chemistry of Solids* 67(9-10), 2091–2094.

Manoun, B., Saxena, S. K., Hug, G., Ganguly, A., Hoffman, E. N. & Barsoum, M. W. (2007). Synthesis and compressibility of $Ti_3(Al, Sn_{0.2})C_2$ and $Ti_3Al(C_{0.5}, N_{0.5})_2$. *Journal of Applied Physics* 101(11).

Mattsson, A. E., Schultz, P. A., Desjarlais, M. P., Mattsson, T. R. & Leung, K. (2005). Designing meaningful density functional theory calculations in materials science - A primer. *Modelling and Simulation in Materials Science and Engineering* 13(1).

Mauchamp, V., Yu, W., Gence, L., Piraux, L., Cabioc'H, T., Gauthier, V., Eklund, P. & Dubois, S. (2013). Anisotropy of the resistivity and charge-carrier sign in nanolaminated Ti_2AlC: Experiment and ab initio calculations. *Physical Review B - Condensed Matter and Materials Physics* 87(23), 1–7.

Medvedeva, N. I., Novikov, D. L., Ivanovsky, A. L., Kuznetsov, M. V. & Freeman, A. J. (1998). Electronic properties of Ti_3SiC_2-based solid solutions. *Physical Review B* 58(24), 16042–16050.

Methfessel, M. & Paxton, A. T. (1989). High-precision sampling for Brillouin-zone integration in metals. *Physical Review B* 40(6), 3616–3621.

Middleburgh, S. C., Lumpkin, G. R. & Riley, D. (2013). Accommodation, Accumulation, and Migration of Defects in Ti_3SiC_2 and Ti_3AlC_2 MAX Phases. *Journal of the American Ceramic Society* 96(10). Ed. by Y. Zhon, 3196–3201.

Momma, K. & Izumi, F. (2008). VESTA : a three-dimensional visualization system for electronic and structural analysis. *Journal of Applied Crystallography* 41(3), 653–658.

Momma, K. & Izumi, F. (2011). VESTA 3 for three-dimensional visualization of crystal, volumetric and morphology data. *Journal of Applied Crystallography* 44(6), 1272–1276.

Montaña, J. C. (2018). *Basic BoltzTraP2 tutorial*. `https://gitlab.com/sousaw/BoltzTraP2/wikis/tutorial`.

Music, D., Sun, Z., Ahuja, R. & Schneider, J. M. (2006). Electronic structure of $M_2AlC(0001)$ surfaces (M = Ti,V,Cr). *Journal of Physics: Condensed Matter* 18(39), 8877–8881.

Music, D., Sun, Z., Ahuja, R. & Schneider, J. M. (2007). Surface energy of M_2AC (0001) determined by density functional theory (M=Ti,V,Cr; A=Al,Ga,Ge). *Surface Science* 601(4), 896–899.

Naguib, M. et al. (2011). Two-dimensional nanocrystals produced by exfoliation of Ti_3AlC_2. *Advanced Materials* 23(37), 4248–4253.

Naguib, M., Mochalin, V. N., Barsoum, M. W. & Gogotsi, Y. (2014). 25th anniversary article: MXenes: A new family of two-dimensional materials. *Advanced Materials* 26(7), 992–1005.

Neugebauer, J. & Scheffler, M. (1992). Adsorbate-substrate and adsorbate-adsorbate interactions of Na and K adlayers on Al(111). *Physical Review B* 46(24), 16067–16080.

Nørskov, J. K., Rossmeisl, J., Logadottir, A., Lindqvist, L., Kitchin, J. R., Bligaard, T. & Jónsson, H. (2004). Origin of the overpotential for oxygen reduction at a fuel-cell cathode. *Journal of Physical Chemistry B* 108(46), 17886–17892.

Nowotny, V. H. (1971). Strukturchemie einiger Verbindungen der Übergangsmetalle mit den elementen C, Si, Ge, Sn. *Progress in Solid State Chemistry* 5, 27–70.

Ong, K. P., Singh, D. J. & Wu, P. (2011). Analysis of the thermoelectric properties of n-type ZnO. *Physical Review B* 83(11), 115110.

Ong, S. P. et al. (2013). Python Materials Genomics (pymatgen): A robust, open-source python library for materials analysis. *Computational Materials Science* 68, 314–319.

Orellana, W. & Gutiérrez, G. (2011). First-principles calculations of the thermal stability of Ti_3SiC_2 (0001) surfaces. *Surface Science* 605(23-24), 2087–2091.

Pack, J. D. & Monkhorst, H. J. (1977). "Special points for Brillouin-zone integrations"—a reply. *Physical Review B* 16(4), 1748–1749.

Pantea, D., Darmstadt, H., Kaliaguine, S., Sümmchen, L. & Roy, C. (2001). Electrical conductivity of thermal carbon blacks: Influence of surface chemistry. *Carbon* 39(8), 1147–1158.

Parr, R. G. & Yang, W. (1989). *Density-Functional Theory of Atoms and Molecules*. Vol. 16. International series of monographs on chemistry. New York: Oxford University Press.

Pawbake, A. et al. (2016). Wide band gap and conducting tungsten carbide (WC) thin films prepared by hot wire chemical vapor deposition (HW-CVD) method. *Materials Letters* 183, 315–317.

Payne, M. C., Teter, M. P., Allan, D. C., Arias, T. A. & Joannopoulos, J. D. (1992). Iterative minimization techniques for ab initio total-energy calculations: molecular dynamics and conjugate gradients. *Reviews of Modern Physics* 64(4), 1045–1097.

Perdew, J. P. & Wang, Y. (1992). Accurate and simple analytic representation of the electron-gas correlation energy. *Physical Review B* 45(23), 13244–13249.

Perdew, J. P. & Zunger, A. (1981). Self-interaction correction to density-functional approximations for many-electron systems. *Physical Review B* 23(10), 5048–5079.

Perdew, J. P., Chevary, J., Vosko, S., Jackson, K., Pederson, M., Singh, D. & Fiolhais, C. (1992). Atoms, molecules, solids, and surfaces: Applications of the generalized gradient approximation for exchange and correlation. *Physical Review B* 46(11), 6671–6687.

Perdew, J. P., Burke, K. & Wang, Y. (1996a). Generalized gradient approximation for the exchange-correlation hole of a many-electron system. *Physical Review B* 54(23), 533–539.

Perdew, J. P., Burke, K. & Ernzerhof, M. (1996b). Generalized gradient approximation made simple. *Physical Review Letters* 77(18), 3865–3868.

Perdew, J. P., Ruzsinszky, A., Tao, J., Staroverov, V. N., Scuseria, G. E. & Csonka, G. I. (2005). Prescription for the design and selection of density functional approximations: More constraint satisfaction with fewer fits. *The Journal of Chemical Physics* 123(6), 062201.

Pietzka, M. A. & Schuster, J. C. (1994). Summary of constitutional data on the aluminum-carbon-titanium system. *Journal of Phase Equilibria* 15(4), 392–400.

Pietzka, M. A. & Schuster, J. C. (1996). Phase Equilibria in the Quaternary System Ti-Al-C-N. *Journal of the American Ceramic Society* 79(9), 2321–2330.

Sanville, E., Kenny, S. D., Smith, R. & Henkelman, G. (2007). Improved grid-based algorithm for Bader charge allocation. *Journal of Computational Chemistry* 28(5), 899–908.

Scabarozi, T., Ganguly, A., Hettinger, J. D., Lofland, S. E., Amini, S., Finkel, P., El-Raghy, T. & Barsoum, M. W. (2008). Electronic and thermal properties of $Ti_3Al(C_{0.5}, N_{0.5})_2$, $Ti_2Al(C_{0.5}, N_{0.5})$ and Ti_2AlN. *Journal of Applied Physics* 104(7), 073713.

Schrödinger, E. (1926). An Undulatory Theory of the Mechanics of Atoms and Molecules. *Physical Review* 28(6), 1049–1070.

Schuster, J. C., Nowotny, H. & Vaccaro, C. (1980). The ternary systems: CrAlC, VAlC, and TiAlC and the behavior of H-phases (M_2AlC). *Journal of Solid State Chemistry* 32(2), 213–219.

Serway, R. A. (1998). *Principles of Physics*. 2nd. Fort Worth, Texas: London: Saunders College Publishers.

Shao, Y., Yin, G. & Gao, Y. (2007). Understanding and approaches for the durability issues of Pt-based catalysts for PEM fuel cell. *Journal of Power Sources* 171(2), 558–566.

Sharma, S. & Pollet, B. G. (2012). Support materials for PEMFC and DMFC electrocatalysts - A review. *Journal of Power Sources* 208, 96–119.

Son, W., Duong, T., Talapatra, A., Gao, H., Arróyave, R. & Radovic, M. (2016). Ab-initio investigation of the finite-temperatures structural, elastic, and thermodynamic properties of Ti_3AlC_2 and Ti_3SiC_2. *Computational Materials Science* 124, 420–427.

Springborg, M. (1997). *Density-Functional Methods in Chemistry and Materials Science*. Ed. by M. Springborg. John Wiley & Sons.

Srivastava, J. K. (1985). Electrical Conductivity of Silicon Dioxide Thermally Grown on Silicon. *Journal of The Electrochemical Society* 132(4), 955.

Sui, S., Wang, X., Zhou, X., Su, Y., Riffat, S. & Liu, C.-j. (2017). A comprehensive review of Pt electrocatalysts for the oxygen reduction reaction: Nanostructure, activity, mechanism and carbon support in PEM fuel cells. *J. Mater. Chem. A* 5(5), 1808–1825.

Sun, Z., Zhou, Y. & Li, M. (2001). High temperature oxidation behavior of Ti_3SiC_2-based material in air. *Acta Materialia* 49(20), 4347–4353.

Sun, Z. M. (2011). Progress in research and development on MAX phases: a family of layered ternary compounds. *International Materials Reviews* 56(3), 143–166.

Sun, Z. M., Zhou, J., Music, D., Ahuja, R. & Schneider, J. M. (2006). Phase stability of Ti_3SiC_2 at elevated temperatures. *Scripta Materialia* 54(1), 105–107.

Sun, Z. & Ahuja, R. (2006). Ab initio study of the Cr2AlC (0001) surface. *Applied Physics Letters* 88(16), 161913.

Sun, Z. & Zhou, Y. C. (1999). Ab initio calculation of titanium silicon carbide. *Physical Review B* 60(3), 1441–1443.

Tallman, D. J., Anasori, B. & Barsoum, M. W. (2013). A Critical Review of the Oxidation of Ti_2AlC, Ti_3AlC_2 and Cr_2AlC in Air. *Materials Research Letters* 1(3), 115–125.

Tan, J., Han, H., Wickramaratne, D., Liu, W., Zhao, M. & Huai, P. (2014). A comparative first-principles study of the electronic, mechanical, defect and acoustic properties of Ti_2AlC and Ti_3AlC. *Journal of Physics D: Applied Physics* 47(21), 215301.

Tang, W., Sanville, E. & Henkelman, G. (2009). A grid-based Bader analysis algorithm without lattice bias. *Journal of Physics: Condensed Matter* 21(8), 084204.

Thore, A., Dahlqvist, M., Alling, B. & Rosén, J. (2014). Temperature dependent phase stability of nanolaminated ternaries from first-principles calculations. *Computational Materials Science* 91, 251–257.

Tzenov, N. V. & Barsoum, M. W. (2004). Synthesis and Characterization of Ti_3AlC_2. *Journal of the American Ceramic Society* 83(4), 825–832.

Wang, H. et al. (2017). First-Principles Study of Vacancies in Ti_3SiC_2 and Ti_3AlC_2. *Materials* 10(2), 103.

Wang, J., Wang, J. Y. & Zhou, Y. C. (2008a). Stable M_2AlC (0001) surfaces (M = Ti, V and Cr) by first-principles investigation. *Journal of Physics Condensed Matter* 20(22).

Wang, J., Liu, B., Wang, J. Y. & Zhou, Y. C. (2015). Theoretical investigation of thermodynamic stability and mobility of the intrinsic point defects in Ti_3AC_2 (A = Si, Al). *Physical Chemistry Chemical Physics* 17(14), 8927–8934.

Wang, J. Y. & Zhou, Y. C. (2003a). Ab initio investigation of the electronic structure and bonding properties of the layered ternary compound Ti_3SiC_2 at high pressure. *Journal of Physics: Condensed Matter* 15(12), 1983–1991.

Wang, J. Y. & Zhou, Y. C. (2004). Dependence of elastic stiffness on electronic band structure of nanolaminate M_2AlC (M=Ti,V,Nb, and Cr) ceramics. *Physical Review B - Condensed Matter and Materials Physics* 69(21), 1–9.

Wang, J. Y., Zhou, Y. C., Liao, T., Zhang, J. & Lin, Z. (2008b). A first-principles investigation of the phase stability of Ti_2AlC with Al vacancies. *Scripta Materialia* 58(3), 227–230.

Wang, X. H. & Zhou, Y. C. (2002a). Microstructure and properties of Ti_3AlC_2 prepared by the solid–liquid reaction synthesis and simultaneous in-situ hot pressing process. *Acta Materialia* 50(12), 3143–3151.

Wang, X. H. & Zhou, Y. C. (2002b). Oxidation behavior of Ti_3AlC_2 powders in flowing air. *Journal of Materials Chemistry* 12(9), 2781–2785.

Wang, X. H. & Zhou, Y. C. (2003b). Oxidation behavior of Ti_3AlC_2 at 1000–1400 °C in air. *Corrosion Science* 45(5), 891–907.

Wang, X. H. & Zhou, Y. C. (2010). Layered Machinable and Electrically Conductive Ti_2AlC and Ti_3AlC_2 Ceramics: a Review. *Journal of Materials Science & Technology* 26(5), 385–416.

Wolfsgruber, H., Nowotny, H. & Benesovsky, F. (1967). Die Kristallstruktur von Ti_3GeC_2. *Monatshefte für Chemie und verwandte Teile anderer Wissenschaften* 98(6), 2403–2405.

Xiao, J., Yang, T., Wang, C., Xue, J. & Wang, Y. (2015). Investigations on Radiation Tolerance of $M_{n+1}AX_n$ Phases: Study of Ti_3SiC_2, Ti_3AlC_2, Cr_2AlC, Cr_2GeC, Ti_2AlC, and Ti_2AlN. *Journal of the American Ceramic Society* 98(4). Ed. by S. Sinnott, 1323–1331.

Xie, J., Wang, X., Li, A., Li, F. & Zhou, Y. C. (2012). Corrosion behavior of selected $M_{n+1}AX_n$ phases in hot concentrated HCl solution: Effect of A element and MX layer. *Corrosion Science* 60, 129–135.

Xu, X., Wu, E., Du, X., Tian, Y. & He, J. (2008). First-principle study of electronic properties of $Ti_3Si_{1-x}Al_xC_2$ solid solutions. *Journal of Physics and Chemistry of Solids* 69(5-6), 1356–1361.

Yu, M. & Trinkle, D. R. (2011). Accurate and efficient algorithm for Bader charge integration. *The Journal of Chemical Physics* 134(6), 064111.

Yu, W., Li, S. & Sloof, W. G. (2010). Microstructure and mechanical properties of a $Cr_2Al(Si)C$ solid solution. *Materials Science and Engineering: A* 527(21-22), 5997–6001.

Zhang, H. Z. & Wang, S. Q. (2007). First-principles study of Ti_3AC_2 (A = Si, Al) (0 0 1) surfaces. *Acta Materialia* 55(14), 4645–4655.

Zhang, H., Wang, J., Wang, J. Y., Zhou, Y. C., Peng, S. & Long, X. (2013). Role of Nanolaminated Crystal Structure on the Radiation Damage Tolerance of Ti_3SiC_2: Theoretical Investigation of Native Point Defects. *Journal of Nanomaterials* 2013(0001), 1–5.

Zhang, L. & Singh, D. J. (2009). Electronic structure and thermoelectric properties of layered $PbSe-WSe_2$ materials. *Physical Review B* 80(7), 075117.

Zhang, S., Yuan, X. Z., Hin, J. N. C., Wang, H., Friedrich, K. A. & Schulze, M. (2009). A review of platinum-based catalyst layer degradation in proton exchange membrane fuel cells. *Journal of Power Sources* 194(2), 588–600.

Zhao, S., Xue, J., Wang, Y. & Huang, Q. (2014). Ab initio study of irradiation tolerance for different $M_{n+1}AX_n$ phases: Ti_3SiC_2 and Ti_3AlC_2. *Journal of Applied Physics* 115(2), 023503.

Zhou, Y. C., Wang, X. H., Sun, Z. M. & Chen, S. Q. (2001). Electronic and structural properties of the layered ternary carbide Ti_3AlC_2. *Journal of Materials Chemistry* 11(9), 2335–2339.

A. Methodology and Model Validation Supplementary Data

A.1. Bulk k-point Grid Optimisation

Figure A.1 shows the full data from the k-point grid optimisation.

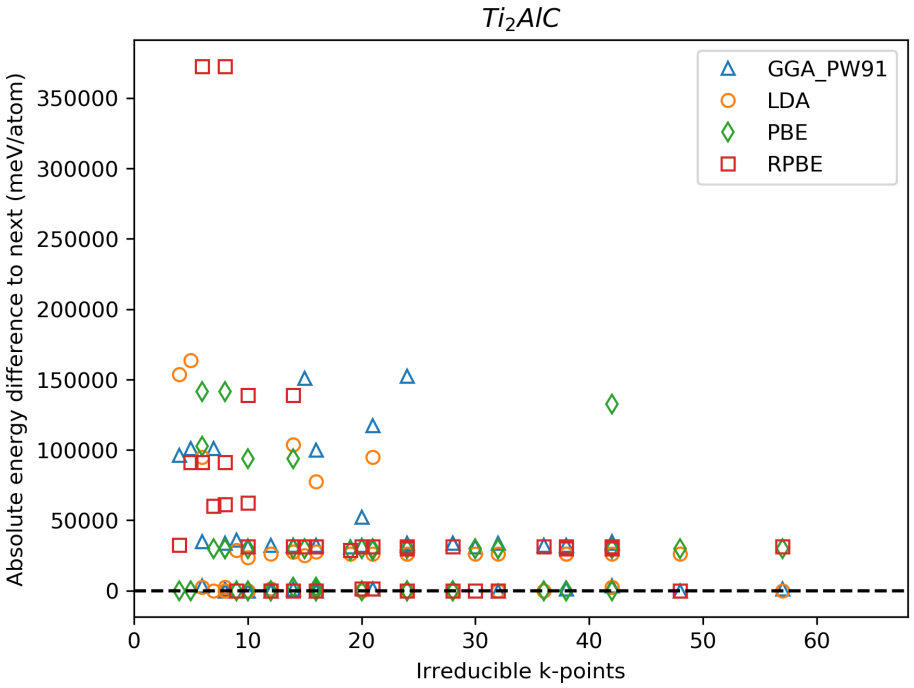

(a)

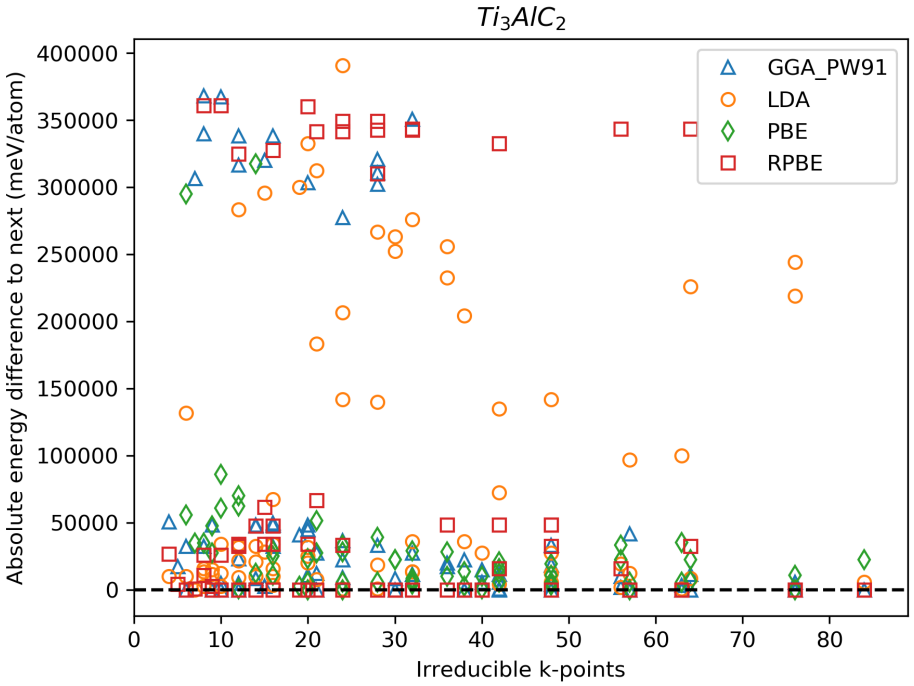

(b)

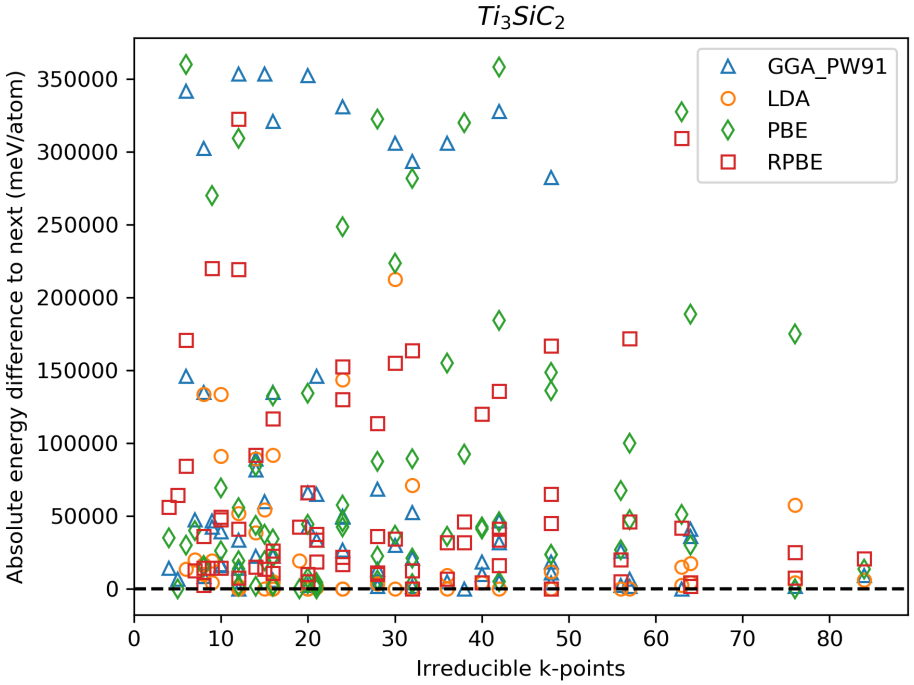

(c)

FIGURE A.1: Complete data for energy difference at different irreducible k-points for Ti_2AlC, Ti_3AlC_2, and Ti_3SiC_2

A.2. Lattice Parameter Optimisation

The Table A.1 shows the results of the different calculations of the a and c lattice parameters. The procedure for calculating the fitted results and automatic relaxation results can be found in Section 3.3. The results for the lattice parameters from the bulk modulus were calculated from the minimum volume from the Birch-Murnaghan EOS. Using this minimum volume, and assuming an equal c/a ratio to that from the literature the a and c values were calculated.

TABLE A.1: Lattice parameters from manual fitting, automatic relaxation and Birch-Murnaghan EOS fitting

MAX Phase	Functional	Manual fitting		Automatic relaxation		Birch-Murnaghan	
		a (Å)	c (Å)	a (Å)	c (Å)	a (Å)	c (Å)
Ti_2AlC	GGA-PW91	3.0800	13.7538	3.0763	13.7429	3.0761	13.7615
	LDA	3.0200	13.5343	3.0085	13.5101	3.0189	13.5056
	PBE	3.0700	13.7623	3.0522	13.7071	3.0701	13.7348
	RPBE	3.0900	13.8220	3.0746	13.7492	3.0893	13.8204
Ti_3AlC_2	GGA-PW91	3.0950	18.4596	3.0908	18.5098	3.0817	18.6207
	LDA	3.0350	18.3278	3.0253	18.3225	3.0345	18.3351
	PBE	3.0750	18.6782	3.0663	18.5725	3.0848	18.6389
	RPBE	3.1050	18.5802	3.0923	18.5653	3.0938	18.6938
Ti_3SiC_2	GGA-PW91	3.0665	17.9334	3.0864	17.7761	3.0830	17.7662
	LDA	3.0165	17.5755	3.0048	17.5728	3.0221	17.4149
	PBE	3.0665	17.8651	3.0479	17.8396	3.0743	17.7162
	RPBE	3.0865	17.8076	3.0821	17.7235	3.0895	17.8034

Literature values:
Ti_2AlC: a = 3.040 Å, c = 13.600 Å (Wang & Zhou, 2010)
Ti_3AlC_2: a = 3.075 Å, c = 18.580 Å (Wang & Zhou, 2010)
Ti_3SiC_2: a = 3.0665 Å, c = 17.671 Å (Barsoum, 2000)

A.3. Bulk Modulus Fitted Curves

Figures A.2, A.3, and A.4 show the fitting of the bulk modulus using the Birch-Murnaghan equation-of-state (Birch, 1947). From the series of a lattice parameter and unit cell volume changes, the systems that had the closest c/a ratio to the experimental c/a ratio were used to fit the to the equation-of-state, to find the bulk modulus. The open source software pymatgen was used to fit the data and generate the graphs (Ong et al., 2013).

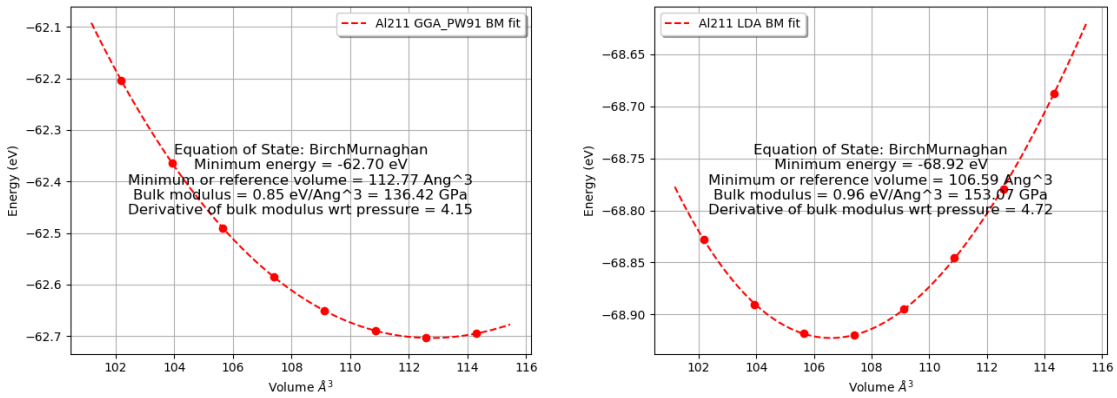

(d) (e)

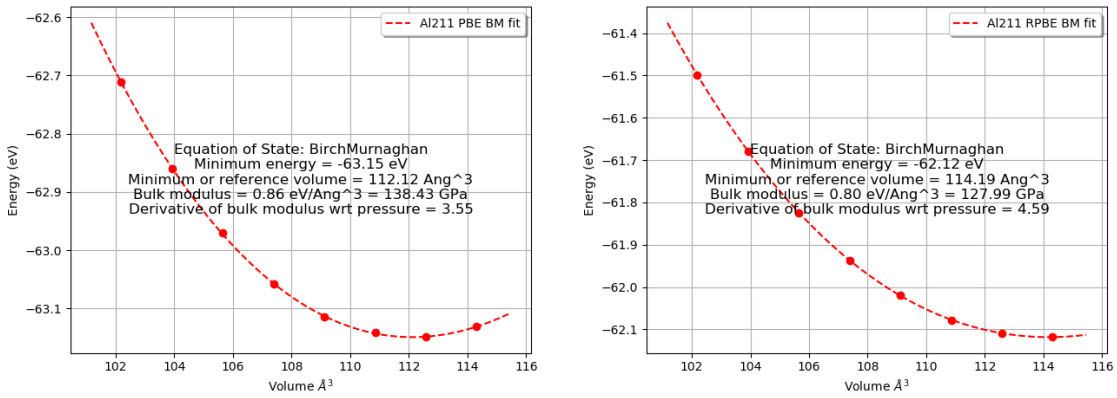

(f) (g)

FIGURE A.2: Bulk modulus graphs using the Birch-Murnaghan equation-of-state for Ti_2AlC. (d) is GGA-PW91, (e) is LDA, (f) is PBE, and (g) is RPBE

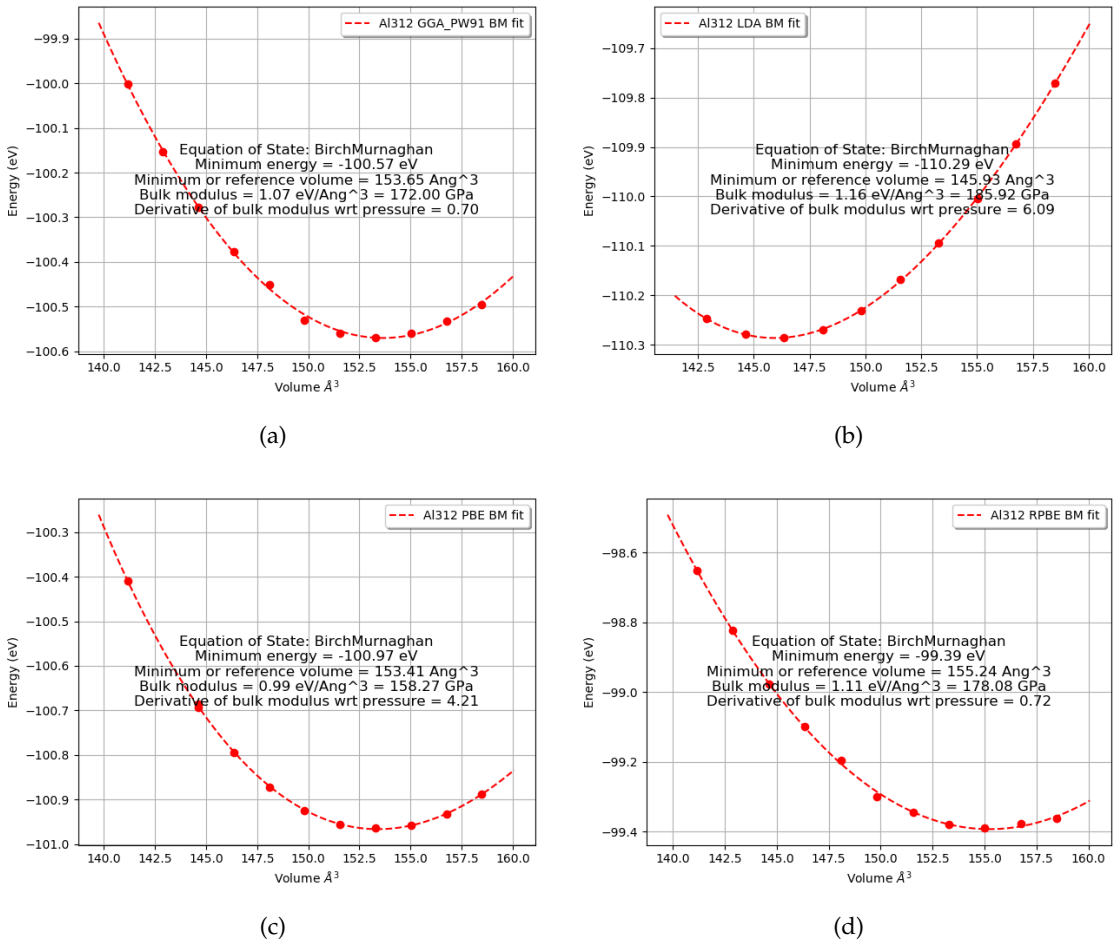

FIGURE A.3: Bulk modulus graphs using the Birch-Murnaghan equation-of-state for Ti_3AlC_2. (a) is GGA-PW91, (b) is LDA, (c) is PBE, and (d) is RPBE

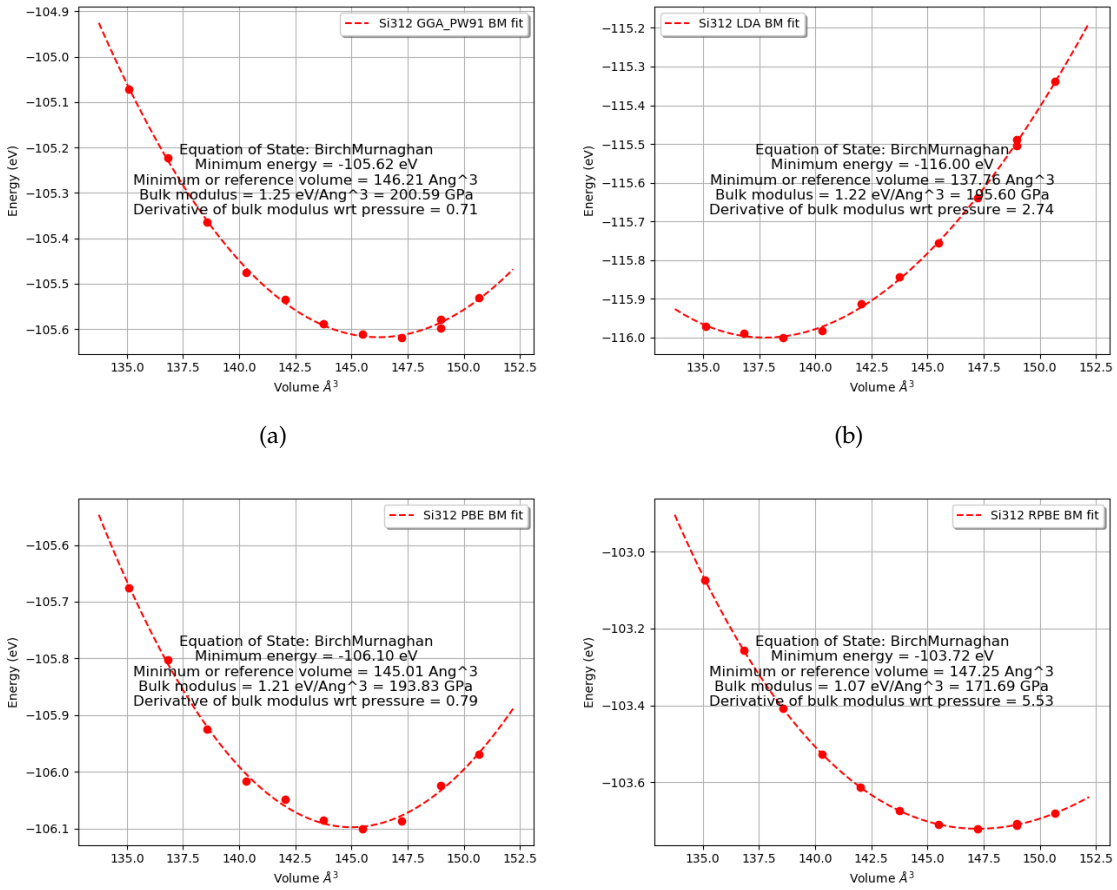

FIGURE A.4: Bulk modulus graphs using the Birch-Murnaghan equation-of-state for Ti_3SiC_2. (a) is GGA-PW91, (b) is LDA, (c) is PBE, and (d) is RPBE

A.4. Surface Distances Between Layers

Figures A.5, A.6, and A.7 show the distances between each atomic layer during relaxation of the unit cell slabs. Different surfaces have been placed next to each other so that the centre of each slab remains in the middle of the slab. The middle of each slab is highlighted in blue. For the 312 MAX phases, the layers were split 4:2, alternating between top and bottom, so that the centre of the slab remained in adjacent layers.

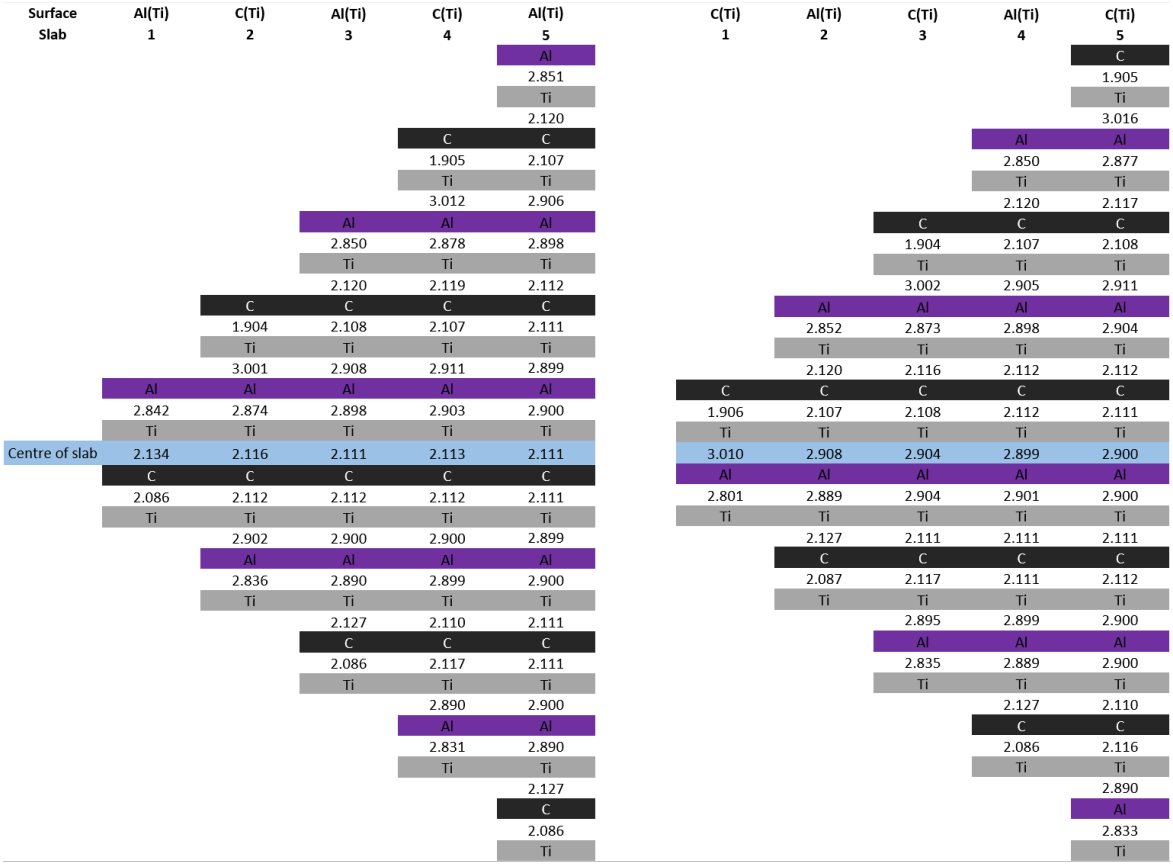

Surface	Al(Ti)	C(Ti)	Al(Ti)	C(Ti)	Al(Ti)	C(Ti)	Al(Ti)	C(Ti)	Al(Ti)	C(Ti)
Slab	1	2	3	4	5	1	2	3	4	5
					Al					C
					2.851					1.905
					Ti					Ti
					2.120					3.016
				C	C				Al	Al
				1.905	2.107				2.850	2.877
				Ti	Ti				Ti	Ti
				3.012	2.906				2.120	2.117
			Al	Al	Al			C	C	C
			2.850	2.878	2.898			1.904	2.107	2.108
			Ti	Ti	Ti			Ti	Ti	Ti
			2.120	2.119	2.112			3.002	2.905	2.911
		C	C	C	C		Al	Al	Al	Al
		1.904	2.108	2.107	2.111		2.852	2.873	2.898	2.904
		Ti	Ti	Ti	Ti		Ti	Ti	Ti	Ti
		3.001	2.908	2.911	2.899		2.120	2.116	2.112	2.112
	Al	Al	Al	Al	Al	C	C	C	C	C
	2.842	2.874	2.898	2.903	2.900	1.906	2.107	2.108	2.112	2.111
	Ti	Ti	Ti	Ti	Ti	Ti	Ti	Ti	Ti	Ti
Centre of slab	2.134	2.116	2.111	2.113	2.111	3.010	2.908	2.904	2.899	2.900
	C	C	C	C	C	Al	Al	Al	Al	Al
	2.086	2.112	2.112	2.112	2.111	2.801	2.889	2.904	2.901	2.900
	Ti	Ti	Ti	Ti	Ti	Ti	Ti	Ti	Ti	Ti
		2.902	2.900	2.900	2.899		2.127	2.111	2.111	2.111
		Al	Al	Al	Al		C	C	C	C
		2.836	2.890	2.899	2.900		2.087	2.117	2.111	2.112
		Ti	Ti	Ti	Ti		Ti	Ti	Ti	Ti
			2.127	2.110	2.111			2.895	2.899	2.900
			C	C	C			Al	Al	Al
			2.086	2.117	2.111			2.835	2.889	2.900
			Ti	Ti	Ti			Ti	Ti	Ti
				2.890	2.900				2.127	2.110
				Al	Al				C	C
				2.831	2.890				2.086	2.116
				Ti	Ti				Ti	Ti
					2.127					2.890
					C					Al
					2.086					2.833
					Ti					Ti

FIGURE A.5: Distances between atomic layers for different slab thicknesses for Ti_2AlC. The centers have been aligned, with the surface changing to facilitate the alignment

FIGURE A.6: Distances between atomic layers for different slab thicknesses for Ti_3AlC_2. The centers have been aligned, with the surface changing to facilitate the alignment

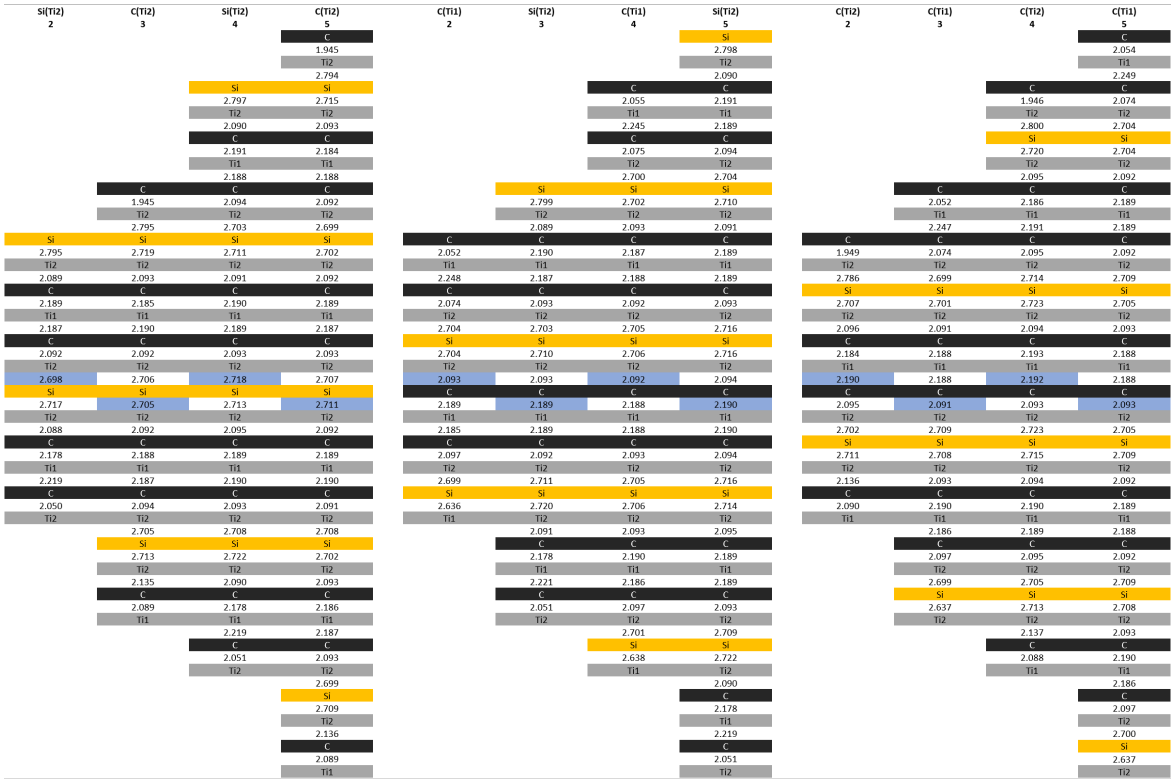

FIGURE A.7: Distances between atomic layers for different slab thicknesses for Ti_3SiC_2. The centers have been aligned, with the surface changing to facilitate the alignment

A.5. Electrostatic Potentials of Surfaces

The electrostatic potential of each surface slab is show in Figure A.8, Figure A.8, and Figure A.8. These show the local electrostatic potential averaged over the x and y coordinates of each unit cell. The electrostatic potential in the vacuum can be clearly seen.

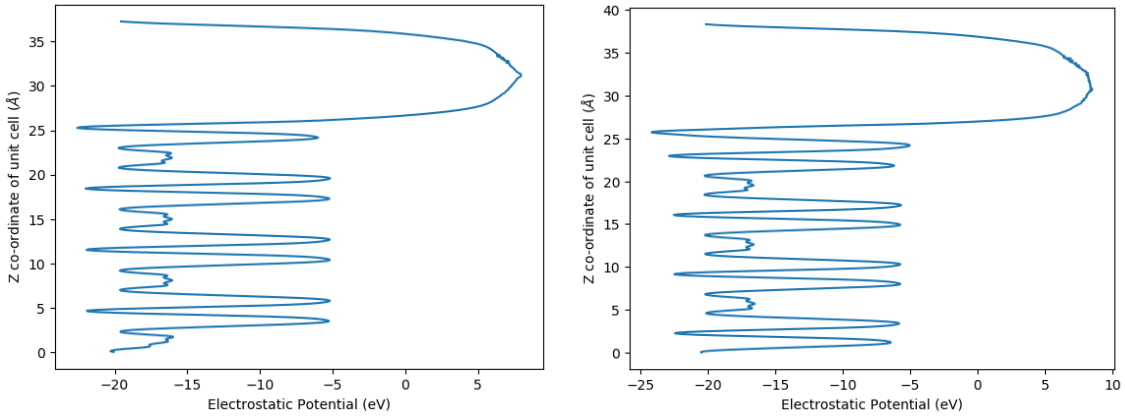

(a) (b)

FIGURE A.8: Electrostatic potential in z direction of unit cell for (a) Ti_2AlC–Al(Ti) and (b) Ti_2AlC–C(Ti)

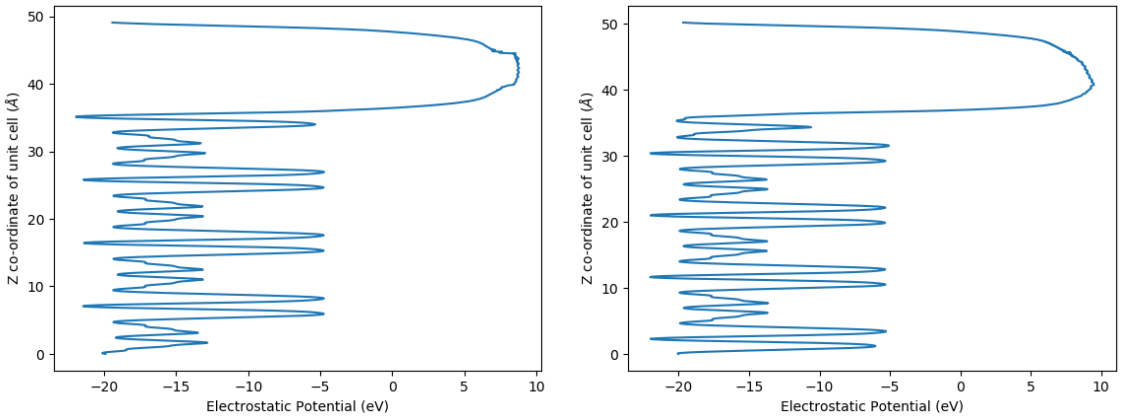

(c) (d)

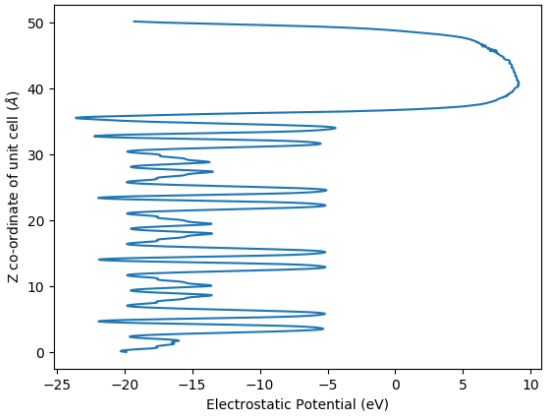

(e)

FIGURE A.8: Electrostatic potential in z direction of unit cell for (c) Ti_3AlC_2–Al(Ti2), (d) Ti_3AlC_2–C(Ti1), and (e) Ti_3AlC_2–C(Ti2)

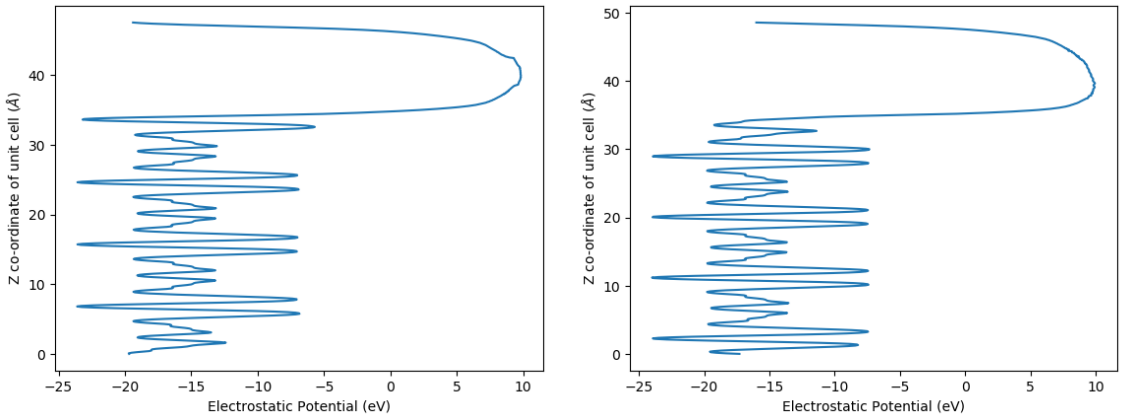

(f) (g)

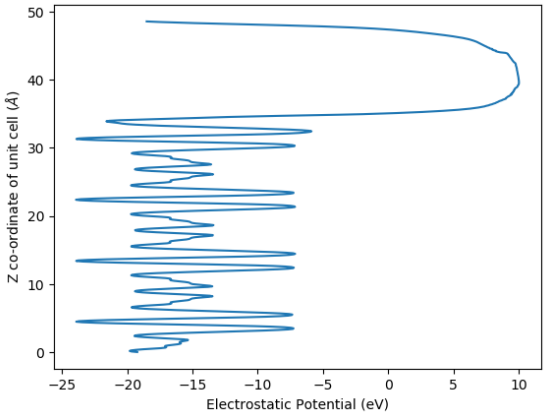

(h)

FIGURE A.8: Electrostatic potential in z direction of unit cell for (f) Ti_3SiC_2–Si(Ti2), (g) Ti_3SiC_2–C(Ti1), and (h) Ti_3SiC_2–C(Ti2)

A.6. Aluminium and Silicon Bulk Optimisation

To determine the vacancy formation energy of the MAX phases, the energy of an Al and a Si atom is needed as reference. Therefore, the energy of bulk aluminium and bulk silicon were calculated and are shown in Figure A.9 and Figure A.10, respectively. Each figure shows the k-point grid optimisation as the absolute energy difference to next against the irreducible number of k-points, the cut-off energy optimisation and the lattice parameter optimisation with the optimised lattice parameter and bulk modulus.

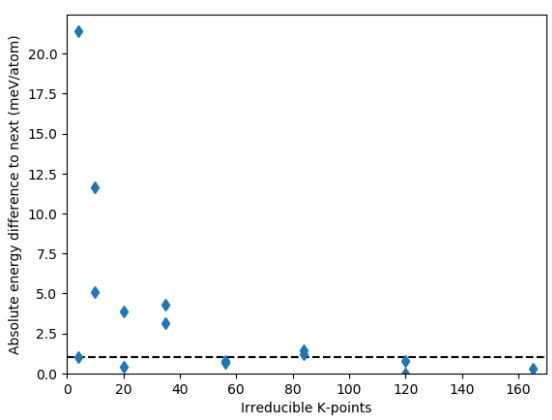

(i)

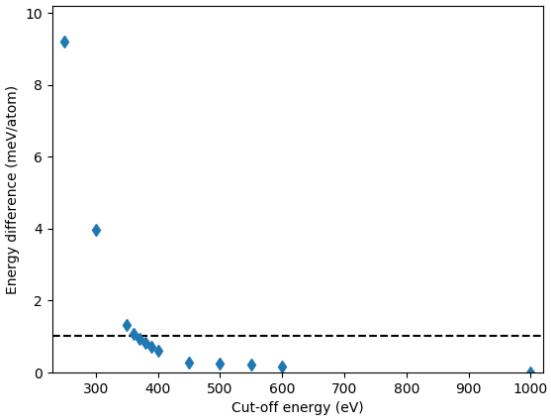

(j)

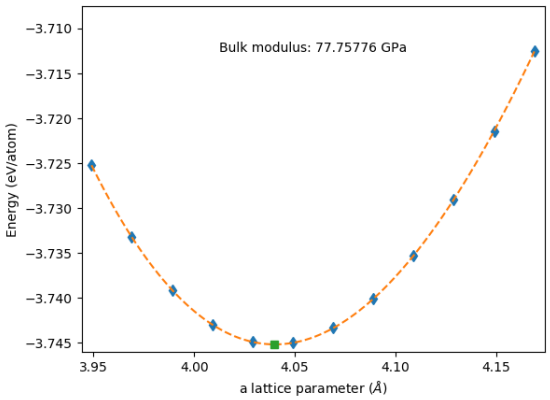

(k)

FIGURE A.9: Optimisation of k-points, cut-off energy and lattice parameter for bulk aluminium

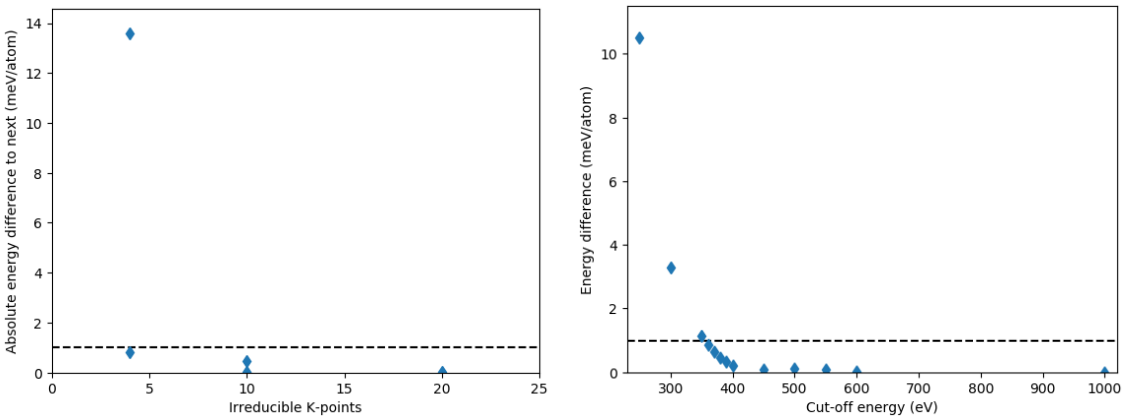

(a) (b)

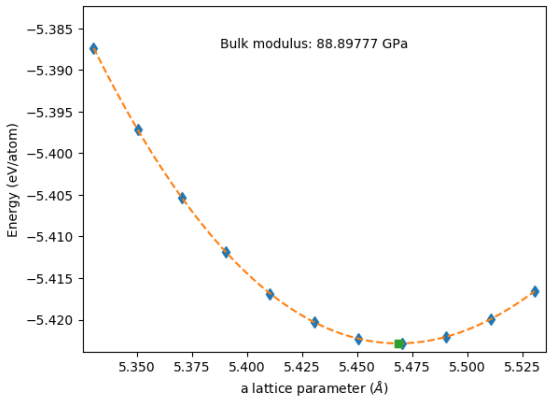

(c)

FIGURE A.10: Optimisation of k-points, cut-off energy and lattice parameter for bulk silicon

B. Bulk Systems Additional Information

B.1. Bulk Vacancies Density of States

The density of states for the average of each atomic layer with and without an A group vacancy are shown in Figure B.1. The DOS of the same layer above and below the vacancy layer are averaged for each element. The layer with the vacancy is at the top of the figure, and the subsequent layers are shown in each successive frame. This is repeated until the next A group layer is reached.

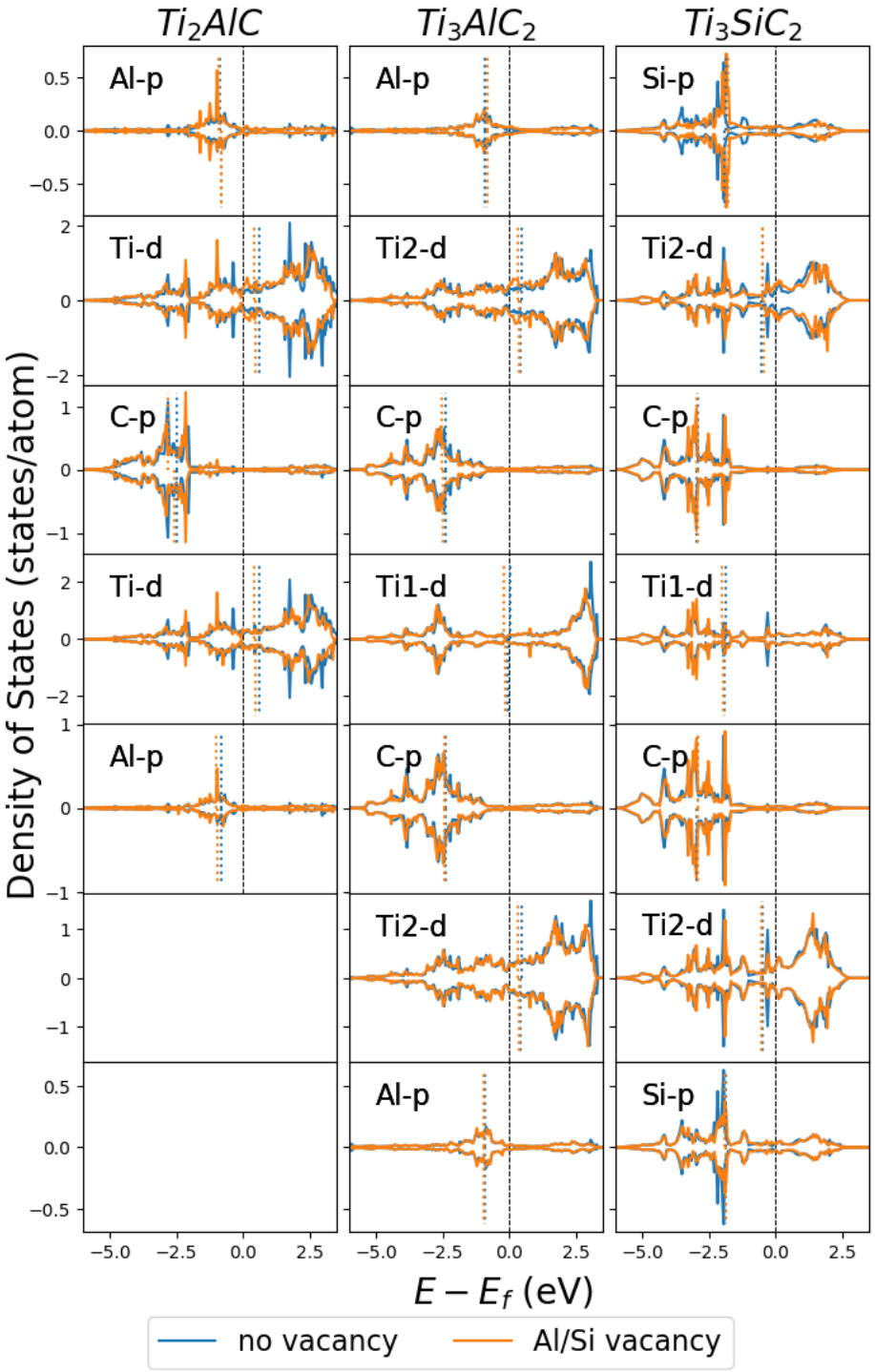

FIGURE B.1: DOS for each layer in bulk systems with and without an A group vacancy